Università degli Studi di Firenze
Facoltà di Scienze Matematiche Fisiche e Naturali

Tesi di Dottorato in
Astronomia

Optimization and astrophysical applications of ultra-high precision spectroscopic measurements

Dottoranda: **Giulia Schettino**

Tutore: **Dr. Marco Romoli**

Co-tutore: **Dr. Ernesto Oliva**

Co-tutore: **Prof. Massimo Inguscio**

Coordinatore: **Prof. Alberto Righini**

Ciclo XXIV
Settore FIS05

You have asked me what I would do and what I would not do.
I will tell you what I will do and what I will not do.
I will not serve that in which I no longer believe,
whether it call itself my home, my fatherland or my church:
and I will try to express myself in some mode of life or art
as freely as I can, and as wholly as I can,
using for my defence the only arms I allow myself to use...
...silence, exile, and cunning.

James Joyce
A portrait of the artist as a young man

Contents

Chapter 1

The search for extrasolar planets and the Giano spectrograph

According to the widely accepted picture of stellar formation, a planetary system is a simple by-product of the stellar formation process. During the contraction of a cloud of gas and dust to form a star, the conservation of angular momentum implies the formation of a flat "accretion disk" around the protostar; this disk is believed to be, in some way, the first stage for planetary formation (see, e.g., [1]). The accepted idea is that dust particles and ice grains in disks combine to form protoplanets: in the outer regions of the disk, where ice can condensate, "planetesimals" achieve in a few million years enough mass (about 10 times the Earth mass) to gravitationally accrete gas forming giant gaseous planets. Instead, in the inner part of the disk, where the volatiles cannot condensate due to the higher temperature, silicate particles merge to form terrestrial planets, like Earth (e.g., [2]). Images taken by the NASA/ESA Hubble Space Telescope during the '90s (e.g., [3]), together with the number of near-IR detections of disks around T Tauri stars (e.g., [4]), has shown that disks around young stars are very common; this fact supports the idea that extrasolar planets should be common [5]. The interest in the search of extrasolar planets is highly bound with the wondering whether some forms of life exist elsewhere the Earth. Expecially, looking for planets similar to our can give answers on how common is life as we know it and how likely is its birth elsewhere in the universe.

The main limitation, as will be analyzed in details in the following, in the detection of extrasolar planets consists in the fact that these bodies are cold objects, so that their visible/near-IR spectrum consists of light reflected from the parent star. In this case, the planet-to-stellar luminosity ratio at optical wavelengths results of the order of 10^{-9} [5], so that, seen from a distance of a few parsecs, the planet is an undetectable signal hidden by the diffraction of the stellar image. This is why extrasolar planets can be detected only via indirect methods.

The first discovery of a planet far from Solar System was in the early '90s, and it was the case of a planet in orbit around the pulsar PSR 1257+12 [6]. The first planet around a Sun-like star was detected in 1995 around the star 51 Pegasi [7]. Up to now, 573 exoplanets has been discovered using a variety of techniques (continuous updated tables can be found on *http://exoplanet.eu*). These discoveries showed the existence of planets with a huge variety of characteristics [8], opening unexpected questions about the origin and evolution of planetary systems. In fact, in general the observed planetary companions are very different from their Solar System counterparts and most of them were not supposed to exist according to the theories accepted till 1995. For example, giant planets were thought to form only far from their stars [9], while about 10% of them have orbital periods of less than five days (like the one discovered in 1995). The growing number of discovered exoplanets allows a statistical analysis of their properties and those of their host stars, providing constraints on physical and chemical processes involved in the formation of these systems and, ultimately, in systems suitable for the birth of life.

1.1 Methods of detection

All these discoveries and studies were made possible due to the development of different planet-search techniques. An overview of all the methods that can be used to infer the presence of extrasolar planets around a star and the number of discovered planets for each method up to the end of 2010 are shown in Figure 1.1.

The most important methods are astrometry, radial velocity and transit techniques. The second one is responsible for most of the discoveries. The basic idea is that a planet induces

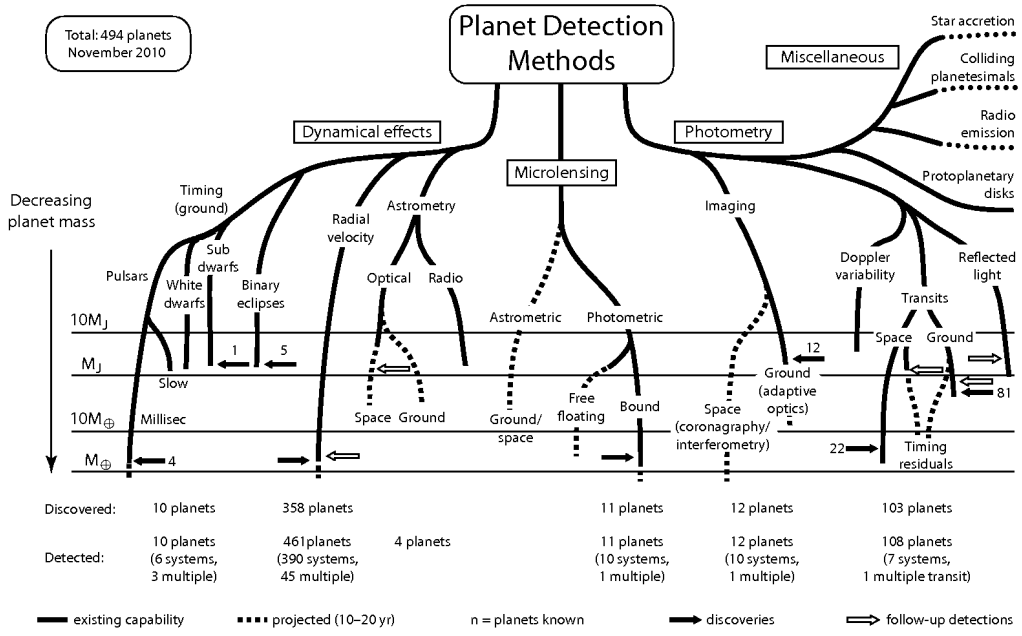

Figure 1.1: Overview of the indirect methods which can be used to detect extrasolar planets and the number of discovered planets for each method up to the end of 2010 (courtesy of: *http://exoplanet.eu*).

dynamical motions on its parent star, giving the possibility to detect its presence by indirect means. Indeed, any star in a binary or multiple system presents a periodic motion around the center of mass of the system, and it is just this effect that gives the possibility to indirectly detect a planet orbiting around a star, i.e. by measuring the dynamical effect induced on the star by the presence of the planet. It is possible to profit of this effect using two different techniques: astrometry and radial velocity. The third method, transit technique, consists of photometric measurements and can be used when the planet orbit is quasi perpendicular to the plane of the sky.

1.1.1 Astrometry

The first astrometric planetary detection was made in 2002 using the Hubble Space Telescope [10]. The idea is to use the dynamical effect that the planet has on the stellar motion to measure the small astrometric periodic shift of the star as it moves around the center of mass of the

star-planet system.

For a system of two bodies of mass M_1 and M_2, the center of mass equation states that $M_1 a_1 = M_2 a_2$, where a_1 and a_2 are the semi-major axis of their orbits, respectively. Defining $a = a_1 + a_2$ as the semi-major axis of the relative orbits (i.e. the two body separation), the center of mass equation can be rewritten as:

$$a_1 = \frac{M_2}{M_1 + M_2}\, a\,. \tag{1.1}$$

Equation 1.1 relates the expected astrometric displacement a_1 of a star of mass M_1 induced by the presence of a planet of mass M_2 to the distance a of the planet from the star. The distance a can also be related to the orbital period P via Kepler's third law:

$$P^2 = \frac{a^3}{M_1 + M_2}\,. \tag{1.2}$$

Measuring a_1, a_2 and P the system can be in principle solved for the masses of the two bodies. In practice, the situation is more complex. We can only hope to measure a_1 and P since we are not able to directly detect the planet. Moreover, the mass M_1 is usually estimated using stellar evolution models and also the fact that observed astrometric orbits are a 2-dimensional projection of a true 3-dimensional orbit needs to be taken into account. The main limitation lies in the too small expected astrometric motions: for example, a Jupiter-like planet ($M_2 = 318\, M_\oplus$, where $M_\oplus$ is the Earth mass) in a 10 years orbit around a solar-mass star located at 10 pc from us induces an astrometric motion of only 440 μarcsec. Nevertheless, as can be seen from Equations 1.1−1.2, the semi-major axis a is proportional both to the mass of the planet and its orbital period, so that the astrometric technique is more sensitive to long period companions, as well as more massive ones. For all these reasons, this method is difficult to use by itself, but, instead, is very useful in combination with radial velocity method to constrain the different orbital parameters of the system (e.g., [11]).

1.1.2 Radial velocity

The radial velocity (RV) method consists in the detection of the velocity wobble K_1 (RV semi-amplitude), along the line of sight, expected for a star of mass M_1 orbited by a planet of mass M_2, which is given by [12]:

$$K_1 = 212.9 \left(\frac{M_1}{P}\right)^{1/3} \frac{q}{(1+q)^{2/3}} \frac{\sin i}{\sqrt{1-e^2}} \text{ [km/s]}\,, \tag{1.3}$$

where $q = M_2/M_1$ and i is the inclination of the orbital axis with respect to the line of sight. The masses are expressed in solar masses and the orbital period P in days. From Equation 1.3 it immediately appears that the RV technique is only able to measure the projected radial velocity, i.e. the radial velocity along the line of sight, so that we can only infer the "projected mass" of a planet ($M_2 \sin i$), which means its minimum mass. This implies that to obtain an unambiguous determination of the true mass the orbital inclination needs to be independently estimated (e.g. through an astrometric detection or a transit measurement).

The radial velocity of the star can be measured from the Doppler shift of the stellar spectral lines using high resolution spectroscopic measurements. In this case, the main challenge is that the radial velocity needs to be measured with a very high precision. For example, a Jupiter-like planet with a 12 years period produces a semi-amplitude K_1 in a Sun-like star of only 13 m/s, while, in the case of an Earth-like planet, $K_1 = 8$ cm/s.

The non-relativistic Doppler equation states that:

$$\frac{\Delta\lambda}{\lambda} = \frac{v}{c}\,, \tag{1.4}$$

where λ is the reference wavelength[1], $\Delta\lambda$ is the observed wavelength shift and v is the radial velocity. At optical wavelengths, a Jupiter-like planet induces a Doppler shift of $\Delta\lambda \sim 10^{-4}$ Å, while, in the case of an Earth-like planet, $\Delta\lambda \sim 10^{-6}$ Å. The situation results a bit better when considering planets orbiting around stars with lower masses than the Sun (i.e. better observable at near-IR wavelengths), but the main constraint still remains: a typical high resolution

[1] At zero velocity, typically the reference wavelength of an absorption spectral line.

spectrograph, with a resolving power $R = \lambda/\Delta\lambda \sim 10^5$, is able only to resolve $\Delta\lambda \sim 0.05$ Å.

This problem can be overcome, first of all, by taking into account that we are dealing with stars which show thousands of well defined absorption lines, so that this information can be used in a statistical way to achieve the necessary precision, usually using a cross-correlation technique (see, e.g., [13, 14]). This is still not enough if the spectrograph itself is not sufficiently stable, or if the instrument drifts cannot be controlled over time. An accurate wavelength-to-pixel calibration is, hence, needed. Up to now this has been usually achieved with the spectrum of a calibration lamp recorded simultaneously with the target spectrum (e.g., [15]), or in some cases using a gas cell spectrum (e.g., [16]).

Currently, the most accurate RV instrument for planet search is the HARPS spectrograph[2] [17]. Figure 1.2 shows a typical radial velocity curve of a star induced by the presence of a planetary companion; this data has been obtained with HARPS observing the star μ Ara (HD 160691) [14]. The orbital parameters of the system (like the semi-amplitude K_1, the orbital period P and the eccentricity e) can be obtained from a fit of the observed points [18]: the showed case refers to a planet with a 9.5 days orbit which induces a sinusoidal radial velocity

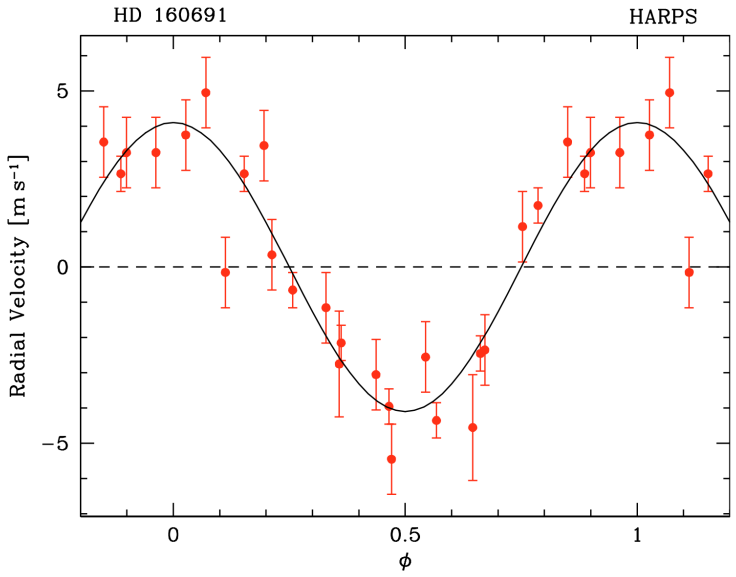

Figure 1.2: Phase radial velocity measured for the star μ Ara (HD 160691) with HARPS [14].

[2] http://www.eso.org/sci/facilities/lasilla/instruments/harps/.

signal with semi-amplitude of 4.1 m/s. Once the orbital parameters are known, $M_2 \sin i$ can be obtained directly from the so called "mass function" [19]:

$$f(m) = \frac{(M_2 \sin i)^3}{(M_1 + M_2)^2} = 1 - 0.36 \times 10^{-7} \, K_1^2 \, (1-e)^{3/2} \, P \, [M_\odot] \, , \tag{1.5}$$

where K_1 in given in km/s and P in days. In the showed case it results $M_2 \sin i = 14 \, M_\oplus$, i.e. of the order of Uranus mass.

A significant limitation to the RV method lies in the fact that intrinsic stellar features, like non-radial pulsation, inhomogeneous convection, spots, unknown stellar blends or acoustic modes may be responsible of variations in radial velocities of the same order of the ones we need to detect (see, e.g., [20, 21]). Given all these effects, diagnostics, like photometry, have to be applied to confirm that the RV signal is really observed due to the presence of a planet. Moreover, these limitations imply that RV technique is applicable mostly for main sequence late-type stars (F, G, K and M), while young active objects as well as early-type fast rotating stars are usually not good target for planet search with this technique, since the presence of dark spots, unknown stellar blends, atmospheric granulation or turbulence motions can "simulate" the presence of a planetary companion [12].

1.1.3 Photometric transit

When a planet crosses the stellar disk as seen from our direction, it blocks part of the star light. This phenomenon is called transit. The geometrical probability (p) that a full transit occurs is given by the ratio between the stellar radius and the orbital radius, $p = R_{star}/a$, for a circular orbit. This means that this technique is more sensitive to short period planets, when the p value is higher. The expected luminosity variation results of the order of [19]:

$$\frac{\Delta L}{L} = \left(\frac{R_{planet}}{R_{star}} \right)^2 \, . \tag{1.6}$$

For a Jupiter-like planet, $R_{planet} \sim 0.1 \, R_{star}$, inducing a photometric variation of the order of 1%, while for an Earth-like planet much lower values are expected, making the use of this method

less suitable.

The main limitation of this technique lies in the fact that, as can be seen from Equation 1.6, the measurement and modeling of a transit light curve gives just the ratio of the stellar-to-planetary radius (see, e.g., [22]): unfortunately, for planets with masses below ~ 100 times the mass of Jupiter, the mass-radius relation becomes extremely flat, so that the photometric signal due to the transit of a Jovian planet or a brown dwarf are undistinguishable [23]. Nevertheless, once the photometric transit and the RV observations are available at the same time, it is possible to almost completely characterize the system, inferring values for radius, mass and density of the planet.

As for the RV method, other phenomena are also able to induce photometric signals similar to those expected from a planetary transit. The most up-to-now prolific photometric transit survey is the Optical Gravitational Lensing Experiment (OGLE)[3] campaign, which announced about 200 possible transit planets [24, 25]. After detecting the RV signatures induced by these orbiting bodies, it turned out that most of systems were rather eclipsing binaries of small stars (late M dwarf) around F - G dwarfs or main sequence stars around giants (e.g., [26, 27]). Eventually, only seven candidates have up to now been confirmed as transit planets.

1.2 Planet-search: state of the art

As previously pointed out, prior to 1995 all our understading of planet formation was based on studies made on the only observable system, the Solar System. The failure of our theories to explain the diversities of the hundreds of discovered exoplanets has shown the necessity of further observations to outline a statistical analysis of the distribution of masses, periods, orbital eccentricity as well as of the chemical properties of the hosting stars.

In the following, I will briefly overview the major observational results. Then, I will focus on the specific topic of the search for Earth-like planets, introducing the general aim at the base of this Thesis: a feasible way to detect this type of planets using a high resolution astronomical spectrograph.

[3] http://ogle.astrouw.edu.pl/.

1.2.1 Planet-search results

For what concerns the masses of exoplanets, the analysis of the mass distribution of short period (below $\sim$ 3000 days) companions to solar-type stars is shown in Figure 1.3 [28]. As can be seen, although the RV technique is more sensitive to massive companions, the frequency of discovered planets increases as a function of decreasing mass. Furthermore, this distribution falls

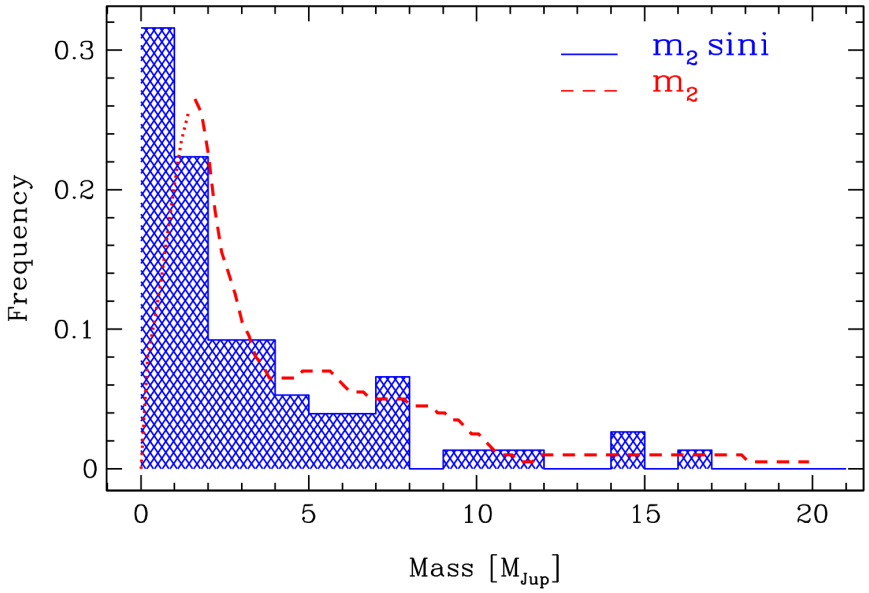

Figure 1.3: Mass function of companions to solar-type stars (blue). The dashed line (red) represents the result of a statistical deconvolution of the observed distribution in order to take into account the effect of orbital inclination [28].

to a value close to zero for masses between about 10 and 20 times the mass of Jupiter; from 20 to 60 Jupiter masses there is, then, a scarcity of companions to solar-type stars. This gap, which separates the lower mass planetary companions from their higher mass stellar counterparts, is called the "brown-dwarf desert" [29]. Together with the shape of the mass distribution, this suggests a different formation mechanism between low-mass and high-mass companions.

The mass-period distribution of planetary companions is shown in Figure 1.4-a [12]: there seems to be a paucity of high-mass planetary companions orbiting on short period trajectories (lower than $\sim$ 40 days). The analysis of the orbital eccentricity distribution, shown in Figure 1.4-b [12], also indicates a possible range of values from about 0 to more than 0.9, similar to the

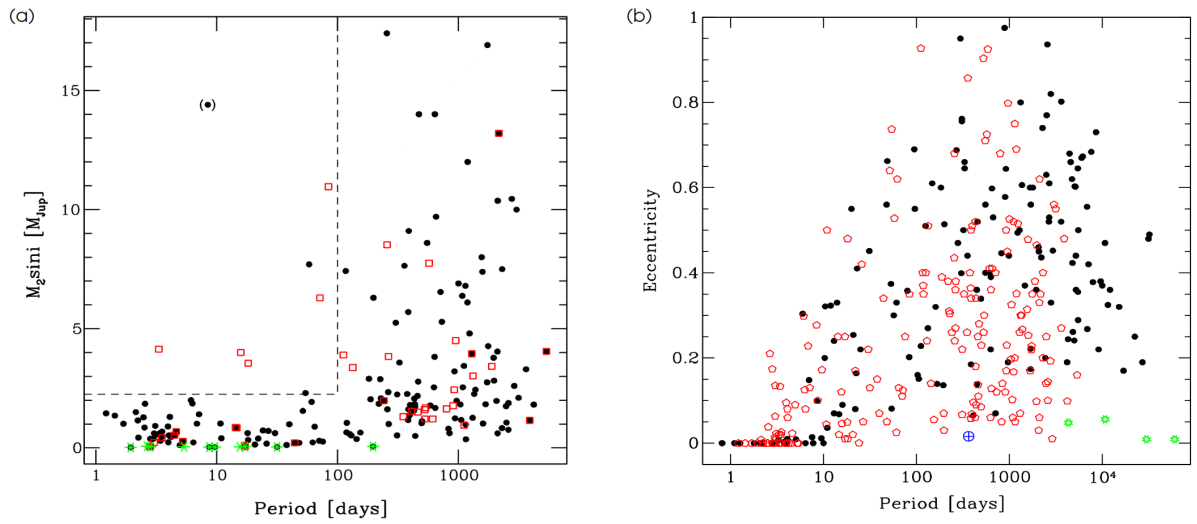

Figure 1.4: (a): period-mass distribution of known extrasolar planets orbiting dwarf stars. Black dots are for planets around single stars, red squares for planets in binaries, green star symbols for the few discovered terrestrial planets. Dashed black lines are limits for 2.25 Jupiter-mass (horizontal) and 100 days (vertical). (b): period-eccentricity diagram for the sample of known exoplanets (red open pentagons) in comparison with stellar binaries (black dots). The Earth (blue cross) and the giant planets of Solar System (green starred symbols) are also indicated [12].

range found in binary systems.

Tha statistical analysis of stars hosting planets has also shown a correlation between the star chemical composition and the presence of a planet. More than 20% of stars with metallicity higher than two times the solar metallicity results to harbor a planet, while only about 3% of stars with solar metallicity has a giant planet (see, e.g., [30]), as shown in Figure 1.5. This suggests that planetary formation is more efficient in a metal-rich environment.

1.2.2 The search for terrestrial planets

Most of the detected planets are gaseous giants similar to Jupiter, with typical masses of a few hundreds of Earth masses. Lower mass planets are difficult to detect because the induced radial velocity variations are smaller. However, in the last years, several planets with masses in the Uranus-Neptune range or lower ($\leq 20 M_{\oplus}$) have been detected (e.g., [31, 32, 33]). The discovery of very low mass planets so close to the detection threshold of RV surveys, and over a

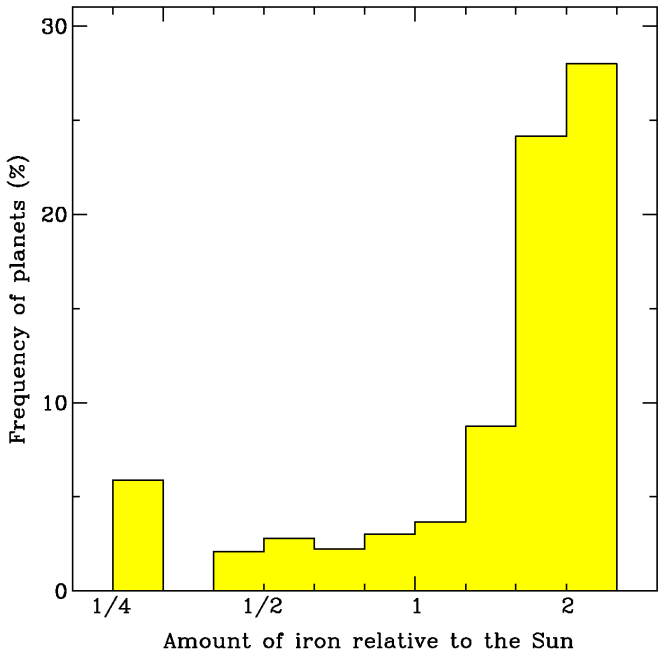

Figure 1.5: Percentage of stars having a planetary companion as a function of stellar metallicity [30].

short period of time, suggests that this kind of objects may be rather common.

The peculiar interest in searching for Earth-like planets instead of giant planets is, of course, related to the appealing question of how exceptional are the conditions which have made possible the birth of life on Earth and, eventually, how high can be the probability that some form of "life" rises elsewhere. In fact, the argument that the Earth cannot be a special place implies that life should be a common phenomenon in planetary systems. It is also difficult to discuss what life might be like on other planets because the only example we have is the life, as we know it, on Earth. If we assume that life elsewhere has some of the features that we see on Earth, i.e. is based on liquid water, oxigen and carbon, it is possible to define a "habitable zone" [34] around a star so that, if a planet remains there for a sufficient amount of time, life as we know it can rise. The habitable zone can be defined as the circumstellar belt where an Earth-like planet can mantain liquid water on its surface. This zone can be defined not only around Sun-like stars: for example, we can expect to find conditions favourable to the birth of life around a M-type star, but, since it is much less luminous than the Sun, the habitable zone will be placed closer to the

star. Only by carrying on a statistical study of the properties of planets and host-stars we can eventually understand how common are the conditions suitable for life elsewhere in the universe.

As pointed out in Section 1.1.2, the RV technique is the most promising method to detect the presence of Earth-like planets. For solar-type stars this implies to reveal signals of the order of several cm/s: while current high resolution spectrographs can, in principle, reach this goal, it is necessary to use a calibration source which guaratees at least this resolution. Standard astronomical calibration sources, such as Th-Ar lamps (see Section 3.1.1), are not suitable for this aim. The situation is much easier for lower mass stars, where the RV signature of an Earth-like planet becomes of the order of 1 m/s (see Section 1.4 for a detailed description). These low mass stars are cool and can only be observed at IR wavelengths, where classical Th-Ar and Th-Ne lamps do not emit enough lines for a proper wavelength calibration [35].

This Thesis describes the design and the realization of a new type of calibration apparatus, based on a laser frequency comb in the near-IR as the main source, capable to produce hundreds of lines with a stability which is orders of magnitude better than 1 m/s. Together with the general purpose of building a suitable calibration system for near-IR ($1 - 2$ μm range) high resolution spectroscopic observations, the specific application of the system to the Giano astronomical spectrograph will be presented.

1.3 The Giano spectrograph

Giano[4] is an optimized IR spectrometer which can yield, in one shot, $0.95 - 2.5$ μm wide spectra at high resolution (resolving power $R \simeq 50000$ with a 0.5" slit or $R \simeq 25000$ with a 1" slit), mantaining a very high throughput throughout the whole spectral range [36]. Giano is now being built at INAF - Arcetri Astrophysical Observatory in Florence. The project is part of the Second Generation Instrumentation Plan of the Telescopio Nazionale Galileo (TNG), located at Roque de Los Muchachos Observatory (ORM), La Palma, Spain[5]. TNG is a 3.58 m alto-azimuthal telescope with a F/11 focal aperture and equipped with an active optics system. Its 2 Nasmyth foci host five instruments which are permanently mounted and operating. They

[4] http://www.bo.astro.it/giano.
[5] http://www.tng.iac.es.

offer a large variety of observing modes, covering the optical and near-IR wavelength ranges and spanning from broadband imaging to high resolution spectroscopy.

Giano will be able to reach magnitude limits similar of those of 2MASS[6] and DENIS[7], i.e. any object detected by these IR surveys can be studied at high spectral resolution with Giano spectrograph. One of the main goal will be the detection of extrasolar rocky planets around cool low mass stars. In fact, the capability to simultaneously measure a huge number of near-IR features at high resolving power make it an optimal tool to this aim.

1.3.1 Instrument overview

A schematic overview of the Giano design is shown in Figure 1.6, which includes the cryostat with the cold optics, array and electronics, the fiber-fed interface and calibration units, the instrument calibration software and electronics. Thermal background will be minimized by a cold pupil image matched by a fixed Lyot stop, foreseen before the spectrometer entrance slit. The slit exchange system is designed to optimize the stability and repeatibility of the slit positioning. The instrument cryostat will be mounted at the TNG Nasmyth-A focus at a fixed position. Light from the telescope will be fed through a fiber (see Section 1.3.3).

The core of Giano is the spectrometer unit, formed by an optical system which sends the radiation to a commercial 23.2 l/mm R2 echelle grating[8], that acts as high resolution disperser. The spectrometer unit and a 2048×2048 pixels HAWAII-2 array[9] are fixed to an optical bench which will operate in vacuum at cryogenic and thermostated temperatures.

1.3.2 The Giano optics

The optical layout of Giano is shown in Figure 1.7 [37]. The spectrometer consists of a canonical three mirrors anastigmatic (TMA) combination, used in double-pass, which acts both

[6] http://www.ipac.caltech.edu/2mass/.

[7] http://cdsweb.u-strasbg.fr/denis.html.

[8] Echelle reflecting gratings are often referred to by their "R number", where R is the tangent of the *blaze* angle q (i.e. the grating angle at which most of the incident light is reflected), $R = \tan q$. In the case of an R2 echelle, the blaze angle is, thus, $\tan^{-1} 2 = 63.4°$.

[9] The detector is the commercial HAWAII-2 2.5 μm 2048×2048 pixels PACE FPA n.H2-83, from Rockwell Scientific. It consists of a HgCdTe sensor grown on a Sapphire substrate and bonded on a multiplexer. Detailed information can be found on http://www.teledyne-si.com/imaging/hawaii2rg.html.

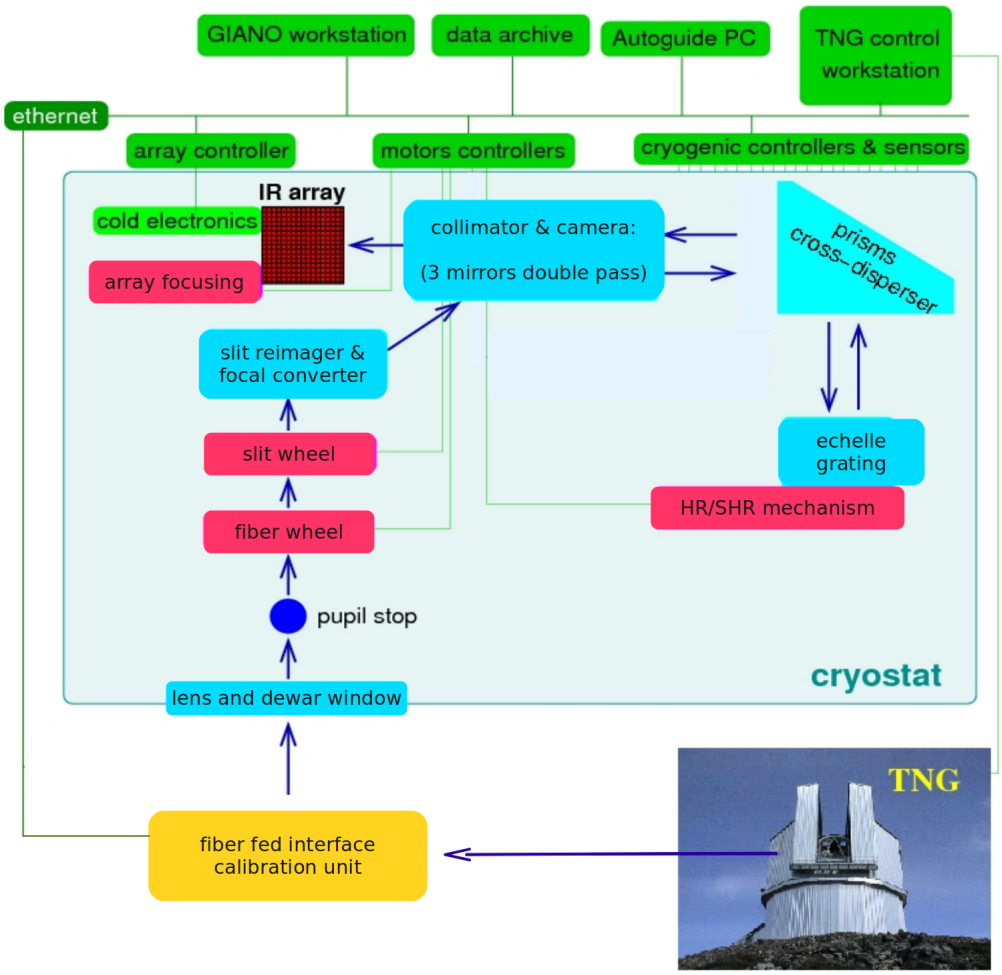

Figure 1.6: Schematic overview of the Giano design (http://www.bo.astro.it/giano). The light path is indicated by the dark blue arrows. The spectrometer optical elements are schematized as cyan boxes, while the moving parts are displayed in magenta. Green boxes represent electronics and software systems.

as collimator and camera. The collimated beam diameter is 100 mm and the system focal length is 420 mm. The echelle grating works at a fixed position in a quasi-Littrow configuration with an off-axis along the slit of 5°. A system of prisms from high dispersing IR optical materials acts as cross-disperser (CRD). As the source image lies close to the detector, a 2-mirrors (FR1-FR2) system is also included, to re-image the slit at a convenient place far from any critical element.

The entrance slit is illuminated by the F/11 beam from the pre-slit optics and feeds the conic FR1-FR2 mirrors, which re-image the focal plane at F/4.2 on a side of the detector. This

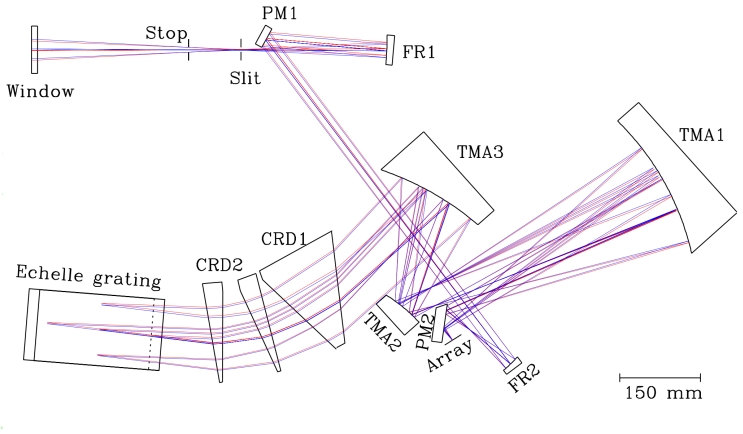

Figure 1.7: Optical layout and ray-tracing of Giano [37]: PM (plane mirror), FR (conic focal reducer mirror), TMA (anastigmatic mirror), CRD (cross-dispersing prism).

distance is large enough to avoid vignetting for slit lengths less than 10". The light, then, enters into the TMA which creates a 100 mm collimated beam feeding the cross-dispersing prisms and the grating. The rays reflected from the grating pass again through the prisms and are focused onto the array by the same three mirrors. Two flat mirrors (PM1, PM2) are added to conveniently position the array, the input slit and the FS1-FR2 mirrors.

1.3.3 Fiber-fed interface

The spectrometer is fed through a bundle of two ZBLAN[10] fibers, manufactured by IRphotonics[11], with a 85 μm core (corresponding to a sky-projected angle of 1") and a cladding of 125 μm, one to collect the radiation from the observed object, the other to, simultaneously, measure the light from the sky. The two fibers are aligned and mounted inside a custom connector, with the fibers centers at a distance of 0.25 mm, corresponding to a sky-projected angle of 3".

As will be more clear in Chapter 3, one of the main advantages of a fiber-fed interface with respect to an optical pre-slit systems is strongly correlated with the calibration system that will be described in this Thesis. A comb-based system as the calibration source has a natural fiber-coupled output (expecially in the case of dielectric coated mirrors, see Chapter 5). A

[10]ZBLAN (ZrF4-BaF2-LaF3-AlF3-NaF) is a heavy metal fluoride glass, with a broad optical transmission window (from 0.3 to 7 μm), low refractive index (1.50) and low dispersion.
[11]www.iguide-irphotonics.com.

configuration such that the calibration spectrum is directly fed into the spectrograph via an optical fiber can be envisaged as the stablest one and potentially the best one for tracking real-time distortions of the spectrogragh wavelength scale. In the case of Giano, this can be reached by feeding the spectrograph with a third fiber, carrying the calibration spectrum light so that it can be recorded simultaneously to the object spectrum.

In general, a significant contribution to the radial velocity uncertainty is given by a non-uniform illumination of the spectrograph slit. In fact, if the slit is not uniformly illuminated, the variation of illumination would reflect itself in a variation of the image profile and position on the detector, thus limiting the measurement accuracy. Since ideally one would deliver the calibration light to the spectrograph via a uniform and isotropic source (such as an integrating sphere), in the case of a fiber-fed spectrograph, where the slit is illuminated by a directional and coherent beam, it is necessary to act in some way on the fiber output to uniformize the light distribution, otherwise a RV offset higher than 1 m/s could be recorded [38]. To this aim a scrambling unit can be introduced, so that the interference among the spatial modes of the fiber due to the coherence of the light source is reduced [39].

1.4 Search for extrasolar planets with Giano

Working in the near-IR range, Giano is more suitable for the search of extrasolar terrestrial planets around M dwarf stars instead of solar-type stars, due to their lower surface temperature (3000−4000 K). M dwarfs, or red dwarfs, are small main sequence stars (masses between 0.08 and 0.5 $M_\odot$, $M_\odot$ being the solar mass) and they make up over 80% of the total number of stars in our galaxy [40]. For a long time, M dwarfs have been considered not potentially suitable for "life" for many reasons. First of all, due to their small size, nuclear reactions proceed really slow so that they emit very little light with respect to the Sun (from 6% of the Sun luminosity $L_\odot$ for the "hottest" ones to less than 0.001 $L_\odot$ for the coldest [41]). To attain Earth-like surface temperatures and receive a sufficient amount of radiation for liquid water, a possible planet needs, hence, to orbit very close to its parent star; under these conditions, it is likely that the planet should have synchronous rotation with the star due to tidal forces [19], i.e. it shows always the

same face to the star, creating a perpetual day on this face and a perpetual night on the other, condition not desirable for the birth of life. Despite these unfavorable conditions, there are many reasons to expect that life, as we know it, could still form on Earth-mass planets around M dwarf stars (see, e.g., [41] and references therein). Although the probability of life to form in this case is low, M dwarf stars are so common with respect to Sun-type stars that we can expect to find some of them which can hold conditions suitable for life. It is hence interesting to search for extrasolar planets around M dwarf stars.

I, now, quantify how the radial velocity (v_*), the orbital period (P) and the orbital radius (R) change in the case of a terrestrial planet orbiting around a M dwarf with respect to a solar-type star, in the simplified hypothesis of circular motion. First of all I assume that, to achieve the same conditions for habitability, the planet receives an amount of radiation equal to the solar constant ($K_\odot = L_\odot/4\pi R^2 = 1353$ W/m^2), so that we can write, in a logarithmic form:

$$\log \frac{L_*}{L_\odot} = 2 \log \frac{R}{1 \text{ a.u.}} , \tag{1.7}$$

where L_* is the M dwarf luminosity, R is the distance between the M dwarf and its planet and 1 a.u. is the Earth−Sun distance. The radial velocity, v_{pl}, of a planet orbiting a M dwarf with respect to that of the Earth, $v_\oplus$, from Kepler's law ($v^2 = GM/R$) is given by:

$$\log \frac{v_{pl}}{v_\oplus} = \frac{1}{2} \left[\log \frac{M_*}{M_\odot} - \log \frac{R}{1 \text{ a.u.}} \right] , \tag{1.8}$$

where M_* is the mass of the M dwarf.

From the center of mass equation, $M_* v_* = M_{pl} v_{pl}$ (where M_{pl} is the mass of the planet), we can derive the radial velocity of the star, v_*, due to the presence of the Earth-like planet, with respect to the Sun radial velocity wobbling induced by the Earth, $v_\odot$:

$$\log \frac{v_*}{v_\odot} = \log \frac{v_{pl}}{v_\oplus} - \log \frac{M_*}{M_\odot} + \log \frac{M_{pl}}{M_\oplus} . \tag{1.9}$$

Substituting Equation 1.8 in Equation 1.9, we find:

$$\begin{aligned} \log \frac{v_*}{v_\odot} &= \frac{1}{2}\left[\log \frac{M_*}{M_\odot} - \log \frac{R}{1 \text{ a.u.}}\right] - \log \frac{M_*}{M_\odot} + \log \frac{M_{pl}}{M_\oplus} \\ &= \log \frac{M_{pl}}{M_\oplus} - \frac{1}{2}\left[\log \frac{M_*}{M_\odot} + \log \frac{R}{1 \text{ a.u.}}\right] . \end{aligned} \tag{1.10}$$

Eliminating R from Equation 1.10 using Equation 1.7, it results:

$$\log \frac{v_*}{v_\odot} = \log \frac{M_{pl}}{M_\oplus} - \frac{1}{2} \log \frac{M_*}{M_\odot} - \frac{1}{4} \log \frac{L_*}{L_\odot} . \tag{1.11}$$

For the orbital period P, in the case of a circular orbit ($P = 2\pi R/v$), we obtain:

$$\begin{aligned} \log \frac{P}{1 \text{ yr}} &= \log \frac{R}{1 \text{ a.u.}} - \log \frac{v_{pl}}{v_\oplus} = -\frac{1}{2} \log \frac{M_*}{M_\odot} + \frac{3}{2} \log \frac{R}{1 \text{ a.u.}} = \\ &= -\frac{1}{2} \log \frac{M_*}{M_\odot} + \frac{3}{4} \log \frac{L_*}{L_\odot} , \end{aligned} \tag{1.12}$$

where 1 yr is the Earth orbital period and the second equality is obtained from Equation 1.8, while the third from Equation 1.7.

To roughly estimate what we can expect for v_*, P and R in the case of a terrestrial planet in orbit around a typical M dwarf star, I use the appropriate relation $L \sim M^4$ [42], which yields:

$$\log \frac{v_*}{v_\odot} \sim \log \frac{M_{pl}}{M_\oplus} - \frac{3}{2} \log \frac{M_*}{M_\odot} , \tag{1.13}$$

$$\log \frac{P}{1 \text{ yr}} \sim \frac{5}{2} \log \frac{M_*}{M_\odot} . \tag{1.14}$$

Considering the typical case $M_* \simeq 0.1 M_\odot$ and that $v_\odot = 0.09$ m/s, we can finally obtain:

$$v_* \sim 3 \times \frac{M_{pl}}{M_\oplus} \text{ m/s} , \tag{1.15}$$

$$P \sim 1 \text{ day} , \tag{1.16}$$

$$R \sim 0.01 \text{ a.u.} . \tag{1.17}$$

These results show the advantages of the search of Earth-like planets around M dwarf stars

instead of Sun-like stars. In fact, the expected radial velocities are more than one order of magnitude higher than the Sun case, making easier to detect the star signal. Moreover, the periods are shorter, so that it is sufficient a shorter observation time to follow an entire planet period.

The aim of this Thesis is to underline the characteristics of the best calibration source to support these observations and to propose a detailed design for the calibration apparatus. As will be explained, the basis for a capable calibration system consists in a laser frequency comb. The properties of this laser will be described in the next Chapter, while in Chapter 3 I will fully analyze the capability of the comb for astronomical applications.

Chapter 2

Optical frequency comb

The birth of optical frequency comb (OFC) is closely connected to the attempt to determine the absolute frequency of spectral lines with ultra-high precision (optical frequency metrology). The idea is that, to infer the unknown frequency of a line, it is necessary to compare it with a nearby line whose frequency is known with the required accuracy. In this sense, an OFC provides, as explained in the following, a set of regularly-spaced sharp lines (a ruler) whose frequencies can be known with an accuracy directly traceable with the frequency primary standard.

2.1 Hystorical background

The advent of highly monochromatic lasers, nearly 40 years ago, has stimulated the development of increasingly accurate experiments aimed at deepening the knowledge of quantum physics laws and determining fundamental constants. In order to obtain highly precise results, it is necessary to measure the frequency of light rather than its wavelength. This is because time can be measured with a higher precision than any other physical quantity: counting the number of cycles in a second can be as accurate as the clock that is used to measure the duration of the second[1].

[1]From 1967 the second is defined as the duration of 9192631770 periods of the radiation corresponding to the transition between two hyperfine levels of the ground state of the ^{133}Cs atom (at rest at a temperature of 0 K). Current commercial Cs clocks provide a precision of several parts in 10^{13}, i.e. a velocity precision of $\sim$0.01 cm s^{-1}. This may even be improved by using a timing signal broadcasted by the Global Positioning System to further stabilize the Cs clock or by setting up a local Cs fountain clock (see, e.g., [43]). As will be explained in the following, for the astronomical case the goal would be to build a calibration source capable to ensure a 1 cm

While it has been quite easy from the beginning to measure radio frequencies with high accuracy, the main problem of frequency metrology was to extend this accuracy to the domain of near-IR and optical oscillations (hundreds of THz). The early approach was to use harmonic frequency chains starting from a Cs atomic clock and generating higher harmonics using non-linear devices (see, e.g., [44]). An alternative approach is the difference-frequency synthesis, which is based on the capability to subdivide a large optical frequency interval into smaller portions with a known relationship to the original frequency gap, and to measure the small frequency difference to yield the original frequency gap (e.g., [45]).

During the '90s, a different approach to the problem has been developed, based on the generation of THz-spanning optical combs, obtained by placing a radio frequency (rf) electro-optic modulator in a low-loss optical cavity, in a way that the cavity enhances modulation efficiency by resonating with the carrier frequency and all generated sidebands producing a comb of frequencies [46]. The main limitation of this approach is that only a few THz bandwidth was achievable due to the cavity dispersion and modulation efficiency. To overcome this restriction, metrologists turned their attention to the technology of passively mode-locked (ML) lasers; in this case, the capability to generate very short pulses was promising to reach a wide spectral coverage in the frequency domain (see Appendix A). The technological problems in realizing such devices were overcome in the late '90s by the advent of Kerr-lens ML Ti:Sa lasers, and from then onwards with the development of increasingly improved fs systems. A new step ahead was, then, made by Prof. Hänsch and coworkers in 1998 identifying the link between ultrafast and ultrastable world [47], i.e. using the modes of a ML fs laser as a precise ruler in frequency space. One year later, the first self-referencing stabilization of the carrier-envelope phase of the pulses emitted by a fs ML laser was demonstrated at JILA [48]. These results led to a big improvement in optical frequency metrology. Moreover, in recent years, the growing interest for frequency comb technology also in other fields has stimulated the proposal of using it for astronomical purposes [49].

s^{-1} precision.

2.2 Operational principles

The basic idea of fs frequency combs from ML lasers is that these lasers can store a single pulse and mantain it on a repetitive path. After each round trip, a copy of this pulse is emitted through the output mirror of the laser, resulting in an indefinite train of laser pulses. Like in any other laser, the energy lost is replenished by stimulated emission in the lasing medium.

2.2.1 Generating the comb spectrum

In a time domain description, each pulse is separated from the following one by the time $\tau = l_c/v_g$, where l_c is the laser cavity length and v_g is the net group velocity. The dispersion in the cavity causes the group and phase velocity (v_ϕ) to be different (see Appendix A.3), so that after each round trip the carrier wave is phase shifted with respect to the peak envelope by a quantity:

$$\Delta\phi = 2\pi l_c \omega_c \left(\frac{1}{v_g} - \frac{1}{v_\phi}\right) , \tag{2.1}$$

where ω_c is the carrier wave angular frequency. The emitted field, $E(t)$, at a fixed spatial location results:

$$E(t) = \sum_n \hat{E}(t - n\tau)\, e^{i[\omega_c t + n(\Delta\phi - \omega_c \tau)]} , \tag{2.2}$$

where $\hat{E}$ represents the envelope of the single pulse electric field and the sum is made over all the pulses.

In the frequency domain, the spectrum is described by the Fourier transform of Equation (2.2):

$$E(\omega) = \sum_n e^{i(n\Delta\phi - n\omega\tau)}\, \tilde{E}(\omega - \omega_c) . \tag{2.3}$$

The only significant components of the spectrum are the ones for which the exponentials in the sum add coherently and this happens when the phase shift between the pulse n and the pulse $n+1$ is an integer multiple of 2π: $\Delta\phi - \omega\tau = 2m\pi$. The corresponding spectrum consists of

a series of discrete, regularly spaced lines with angular frequencies $\omega_m = (\Delta\phi - 2m\pi)/\tau$, or in terms of frequencies:

$$f_m = m f_r + f_0 \,, \tag{2.4}$$

where $f_r = 1/\tau$ is the laser **repetition rate frequency** and $f_0 = \Delta\phi\, f_r/2\pi$ is the **offset frequency** (see Figure 2.1). From Equation (2.4) it can be seen that a frequency comb acts as a bridge between the rf domain, where both f_r and f_0 lie, and the optical frequency domain, in the case of $m = 10^5 - 10^6$, allowing in this way to carry the accuracy in radio frequency measurements to the near-IR and optical domains, or, viceversa, the precision and accuracy of an optical frequency (such as an atomic clock in the UV-visible region) can be moved to radio frequencies using the OFCs.

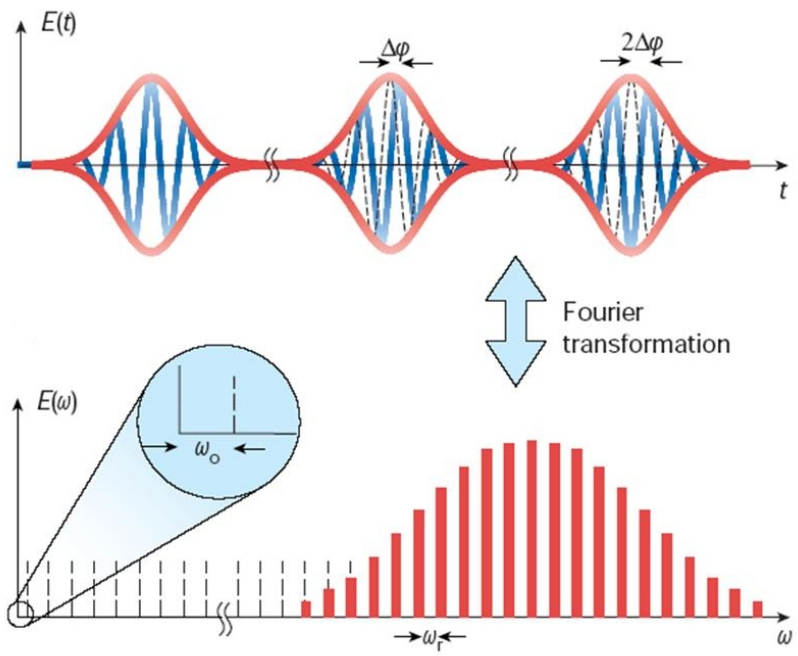

Figure 2.1: Consecutive pulses of the pulse train emitted by a ML laser and the corresponding spectrum. The carrier wave at ω_c (blue line) shifts by a quantity $\Delta\phi$ each round trip with respect to the pulse envelope (red line) [50]. This continuous shift results in a frequency offset ω_0 (or f_0) of the comb from being exact harmonics of the pulse repetition frequency ω_c (or f_c).

2.2.2 Frequency measurements with a comb

In the following I will describe the experimental way to measure an unknown optical laser frequency, f_L, against an OFC. After the frequency comb has been generated, the first step is to determine the offset frequency f_0 and the repetition rate f_r. One of the methods used to measure the offset frequency is the one devised by Prof. Hänsch and coworkers, called self-referencing. To this aim, the comb needs to span an octave, so the output of the fs laser is usually sent along a special highly-dispersive and highly non-linear optical fiber, able to broaden the spectrum. The basic idea of self-referencing is shown in Figure 2.2: the light from the low-frequency wing of the comb is sent through a frequency-doubling crystal; in this non-linear optical medium some radiation is generated at the second harmonic of the input frequency. The light emerging from the crystal has frequency components $2(n'f_r + f_0)$; this radiation is beated on a photodiode with some of the original light of the high-frequency comb wing, whose frequency is $nf_r + f_0$. The signal from this detector contains the frequencies:

$$f = 2(n'f_r + f_0) - (nf_r + f_0) = (2n' - n)f_r + f_0\,. \tag{2.5}$$

For an octave spanning comb there are high-frequency lines which have twice the frequency

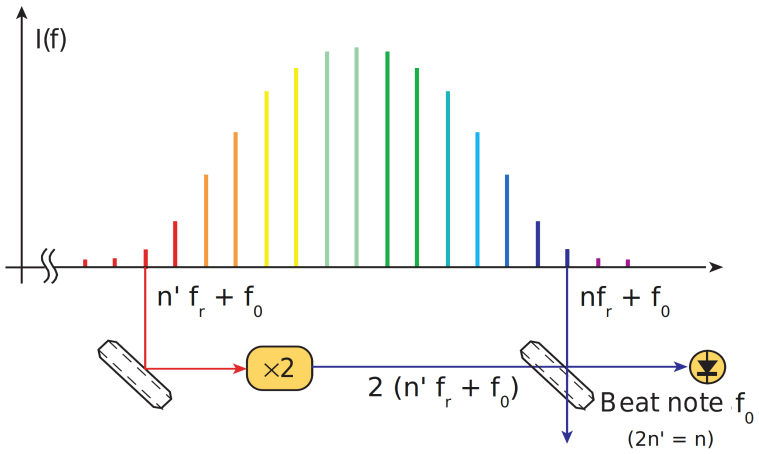

Figure 2.2: Self-referencing method: the comb frequencies span an octave so that modes on the low- and high-frequency wings can be compared, using second harmonic generation, to determine the frequency offset f_0 [50].

of lines on the low-frequency wing, so there are frequency components with $2n' = n$ and these components produce a signal at $f = f_0$ on the photodiode. This frequency is fixed to a given rf value (less than f_r) by controlling the pump power of the ML laser. In fact, passive Kerr-lens mode locking (see Appendix A.2) depends on the pump power by changing the relative phase between phase velocity and group velocity for each generated pulse.

To determine, instead, the repetition rate f_r, which is the inverse of the laser cavity period, it is sufficient to measure on a photodiode the beatnote between adjacent modes. The f_r value is then mantained constant via an electronic feedback which controls the cavity length (i.e. the cavity period) adjusting the position of a cavity mirror with a piezoelectric actuator.

To infer the unknown frequency f_L of a source, the beat frequency between the source and the nearest component of the frequency comb is measured by a photodiode, $f_{beat} = |mf_r + f_0 - f_L|$ (with m integer), so that the unknown frequency results:

$$f_L = mf_r + f_0 \pm f_{beat} \, . \tag{2.6}$$

To determine the sign of f_{beat}, it is sufficient to slightly change the f_r value: increasing f_r, f_{beat} increases in case of negative sign and decreases in case of positive sign. The only remaining information to determine the f_L value with a precision comparable to f_r, f_0 and f_{beat} concerns the integer m. The simplest way to infer m is to measure f_L with other methods (for example with a lambda-meter) with an uncertainty less than f_r [2]: m corresponds to the nearest integer to the quantity $(f_L - f_0 \pm f_{beat})/f_r$.

If f_L is completely unknown, m can however be determined by significantly changing f_r in the following way: assuming f_{beat} to be negative, decreasing f_r will lead first to decreasing f_{beat}, then to increasing f_{beat} because of the changing from the mth mode to the $(m-1)$th mode and so on. Defining m_1, m_2, f_{r1} and f_{r2} as the mode numbers and the repetition rates of two different measurements and the changing in m as $k = m_2 - m_1$, considering that f_L has a fixed

[2] In the case of $f_r = 100$ MHz (a typical value for a near-IR comb) and $f_L \simeq 300$ THz, corresponding to a wavelength of 1 μm, it is necessary to know f_L with a precision greater than 1 part in 10^6, which can be readily achieved.

value in time, the result is: $m_1 f_{r1} + f_0 - f_{beat1} = m_2 f_{r2} + f_0 - f_{beat2}$, from which:

$$m_1 = (k f_{r2} - f_{beat2} + f_{beat1})/(f_{r1} - f_{r2}) \,, \tag{2.7}$$

allowing the determination of the unknown m_1.

2.3 Commercial OFCs

From the late '90s up to now, huge steps further have been made in comb technologies and OFCs in the visible and near-IR domains are by this time commercially available. Two types of laser are common, based on different mode-locking mechanisms: Ti:Sa Kerr-lens mode-locked lasers, which operate around 800 nm, and Er- and Yb-doped fiber lasers, which operate around 1.55 and 1.04 μm, respectively. In the last two years, new technologies have been developed to build new types of OFC in the near-IR, like solid-state frequency combs [51] and Tm-fiber based combs around 2 μm [52]. A general overview of different types of OFC synthesizers and the covered spectral regions are shown in Figure 2.3 [53].

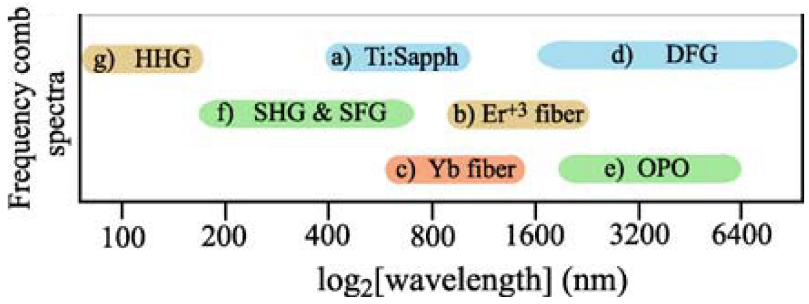

Figure 2.3: General overview of the combs used in different spectral regions: a) Ti:Sa ML lasers in the region 400−1200 nm, b) Er-doped fiber OFCs in the region 1200−2400 nm, c) Yb-doped fiber OFCs in the region 600−1600 nm. Via frequency down coversion of Ti:Sa IR combs can be produced, using d) difference frequency generation (DFG) [54, 55] and e) optical parametric oscillation (OPO) [56] techniques. Finally, f) second harmonic generation (SHG) and g) high harmonic generation (HHG) [57, 58] have been used to cover the UV region.

2.3.1 Ti:Sa optical frequency combs

In order to achieve pulses as short as possible, it is first of all important to use a laser amplifier with a very large gain bandwidth. This is the primary reason for using Ti:Sa, whose bandwidth is between 700 and 1000 nm. In this type of OFCs, the Ti:Sa crystal itself is used as the non-linear material to establish mode-locking operation via the Kerr effect [59] (see Appendix A.2). This effect describes the change in the refractive index n of a material in response to an applied electric field of intensity I [60]:

$$n = n_0 + n_2 I \, . \tag{2.8}$$

As it can be seen from Equation 2.8, the refractive index increases with increasing optical intensity. Since the transverse intensity profile of the intracavity beam is Gaussian, at the center of the beam profile n is increased more strongly than in the wings, hence causing self-focusing, i.e. the Ti:Sa crystal acts as a lens and the beam converges, the focusing increasing with the optical intensity. If an effective aperture[3] is properly positioned along the beam path, high intensities are focused and can be fully transmitted while low intensities experience losses. In this way the non-linear lens acts as a saturable absorber and can favour the ML operation. The Kerr lens ML method itself is not sufficient to generate pulses shorter than about 1 ps, because the group velocity dispersion (GVD) in the laser resonator causes a significant broadening of the pulses [60]. The GVD can be compensated by placing two prisms after the laser cavity: the first prism spatially disperses the pulse so that the longer wavelength components travel through more glass in the second prism than the shorter wavelength ones. Choosing the optimum material, the anomalous dispersion generated in this way counteracts the GVD, minimizing it. Another technique for dispersion control is offered by dielectric mirrors with specially designed coatings ("chirped mirrors") [61], with the advantage of allowing shorter cavities length. As explained in Section 2.2.2, to provide an absolute frequency measurement the comb spectrum needs to span an octave for the offset frequency control. Until recently, the output spectrum generated by a Ti:Sa laser could span only several tens nm, so that the spectrum needed to be broadened via

[3] In real cases the same condition is practically obtained with a cavity configuration at the edge of stability for a given crystal position (where the self-focusing is realized) at which the mode locking operation is favoured with respect to the continuous wave one.

non-linear effects by sending the output of the femtosecond laser along a special highly-dispersive optical fiber, such as an air-silica microstructure fiber [62]: the obtained final spectrum can span the range 520−1130 nm. Recently, the new Octavius series of ultrafast lasers produced by MenloSystems[4], can produce directly from a Ti:Sa laser an octave-spanning output spectrum using special dielectric mirror pairs.

2.3.2 Er- and Yb-doped fiber lasers

In the case of fiber-based fs lasers the mode locking can be obtained in different ways. One of the first approaches was to use additive pulse mode locking (APM) [63]. The fiber is contained in a cavity which has the same round trip time as the laser cavity and is coupled to it by a semitransparent dielectric mirror, so that the pulses in the fiber cavity can interfere with pulses in the main cavity. Properly adjusting the cavity lengths, there is costructive interference near the peak of the pulses but not in the wings, due to different non-linear phase shifts acquired in the fiber. As a result, the peak of a circulating pulse is enhanced while the wings are attenuated. The main problem of this approach is that the cavity length adjustment is very critical and so these systems result not so suitable for commercial products.

Actually, commercial fiber-based combs are based on non-linear polarization effects in the fiber (P-APM). When an intense pulse propagates in a non-polarization mantaining optical fiber, there is a non-linear (i.e. intensity-dependent) change to an elliptical polarization state. The mode locking configuration is, then, obtained by placing some fiber polarization controller or waveplate adjusted in a way that the maximum transmitted power occurs for the highest possible optical intensity in the fiber [64]. A typical scheme for a self-referenced Er-fiber-based OFC with $f_r = 100$ MHz is shown in Figure 2.4 [65]. Into the ring laser, a single polarization is selected by the intracavity polarizing isolator and the waveplates on each side of the isolator are used to optimize the polarization evolution for optimum ML operation. In the case of the P-APM ring laser, two polarization modes, coupled to each other through the intensity-dependent birefringence, are interferometrically combined at a polarizing element, where interference occurs.

[4] http://www.menlosystems.com/home/products/few-cycle-oscillators/octavius-1g-ti-sa-oscillator-overview.html.

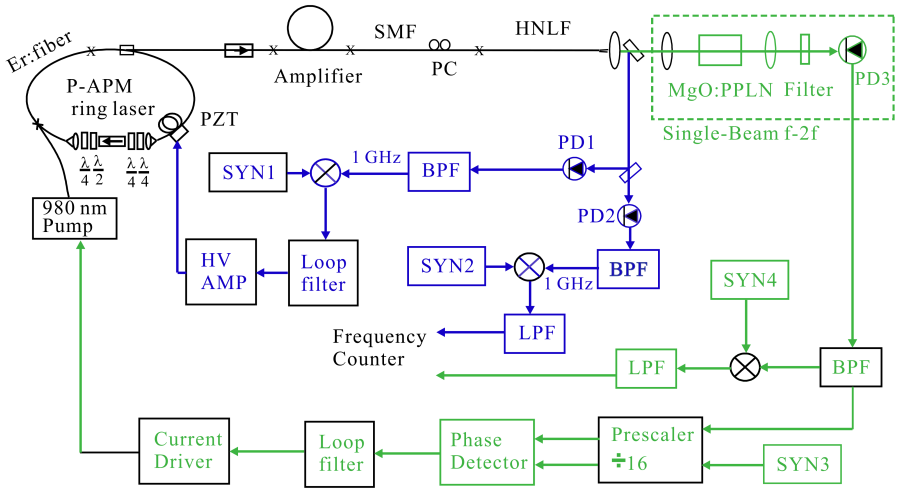

Figure 2.4: Schematic diagram of the Er-fiber-based OFC [65].

A piezoelectric transducer (PZT) is mounted on the fiber (or eventually on an external mirror which is part of the fiber cavity) to precisely control the cavity length. The output of the laser is, then, amplified with an Er-doped fiber amplifier (EDFA) to reach a power level suitable for the spectral broadening to an octave. The pulse trains broadened during the amplification are compressed again in a section of a single mode fiber (SMF) and the output is spectrally broadened in a highly non-linear fiber (HNLF).

This is the technology developed by MenloSystems for the OFC synthesizer used in this Thesis; I will describe it in more details in the following. The offset beat signal is detected right after the HNLF with single beam $f-2f$ heterodyne technique[5]. To stabilize the offset frequency, the beat signal and a reference signal from a synthesizer (SYN3) are first prescaled by a factor 16 and then their phase is detected with a digital phase/frequency detector. The phase signal is fed back to the current driver to stabilize the offset frequency. To characterize the repetition frequency stability, the signal is first detected with an InGaAs photodiode (PD2). The 10^{th} harmonic is filtered out and then mixed down to 1 kHz with a synthesizer (SYN2); the 1 kHz signal is then counted with a universal counter.

[5]The 2100 nm comb lines are frequency-doubled with a 1 cm-long periodically poled magnesium-oxide-doped lithium niobate (MgO:PPLN), while the 1050 nm comb lines are filtered with a 10 nm-wide bandpass filter. The beat signals are detected on an InGaAs photodiode.

Commercial fiber-based OFCs follow the above scheme and cover the octave span from 1050 to 2100 nm with a total power of about 100 mW. A similar scheme has been used to realize, more recently, self-referenced Yb-fiber-based OFCs covering the spectral interval 400−1300 nm [66].

2.4 FC1500 Er-doped fiber OFC

For the measurements of this Thesis, the commercial MenloSystems Er-doped fiber based OFC synthesizer FC1500[6], with repetition rate of 100 MHz, will be used. The FC1500 system consists of an opto-mechanical set-up and special electronics for stabilization and control.

2.4.1 Opto-mechanical setup

The comb system is set up on a 36×38 cm base plate. Figure 2.5 shows a general overview. The femtosecond fiber laser with the internal Er-doped fiber amplifier (EDFA) and the non-linear

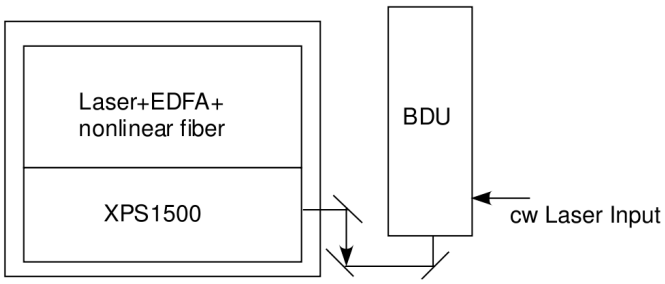

Figure 2.5: A general overview of the opto-mechanical set-up: the laser Er-doped fiber amplifier (EDFA) and non-linear fiber unit, the phase measuring interferometer system (XPS) and the beat detection unit (BDU).

fiber for the octave spanning spectrum generation features a free space output power with up to 350 mW of laser radiation in the range 1−2 μm. In addition, the unit holds two fiber coupled monitor ports (FC/APC) with an output power of approximately 30 mW.

The phase measuring interferometer system (XPS1500) for the offset frequency detection is set up in a one-arm configuration, as shown in Figure 2.6. The main parts are the periodically

[6] http://www.menlosystems.com/home/products/optical-frequency-combs/fc1500-250-wg-optical-frequency-synthesizer-overview.html.

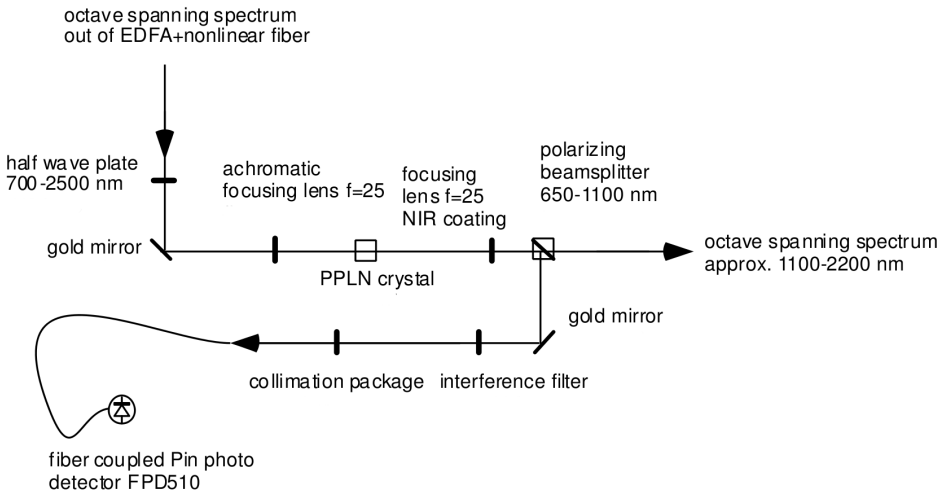

Figure 2.6: Non-linear interferometer (XPS1500).

poled lithium niobate $LiNbO_3$ (PPLN) crystal and the fiber coupled beat detection unit FPD510. The octave spanning spectrum out of the EDFA is guided through the first achromatic focusing lens into the PPLN crystal; using the gold mirror, the light is correctly coupled into one of the periods of the PPLN crystal and the second harmonic light is generated after the crystal. The light is, then, collimated with a near-IR coated lens (focal length 25 mm) and a part of it is reflected in a polarizing beam splitter cube, guided through an interference filter at 1064 nm and coupled into the fiber pigtail of the fiber coupled photodetector (FPD510) using a collimation package. The light not used for the offset frequency detection is transmitted by the polarizing beam splitter cube and is used for the wanted application.

2.4.2 Electronics

The electronics consists of the TC1550 controller for the laser head and the amplifier, the locking electronics for repetition frequency and offset frequency, and the spectrum analyzers to display the beat signals.

To control the whole system and keep it in lock during measurements, not only the main functions of the TC1550 unit can be controlled with the front panel switches, but there is also a "comb control" software, which enables extended access to the TC1550 routines, control of the

locking electronics and monitoring of lockbox output parameters.

The locking electronics used to control the repetition and offset frequencies are sketched in Figure 2.7. Moreover, the reference distribution box RFD10 unit distributes to all the referenced units (counters, synthesizers) a 10 MHz reference signal (from a GPS-disciplined quartz-Rb oscillator, i.e. from a primary frequency standard). In the case of the repetition frequency

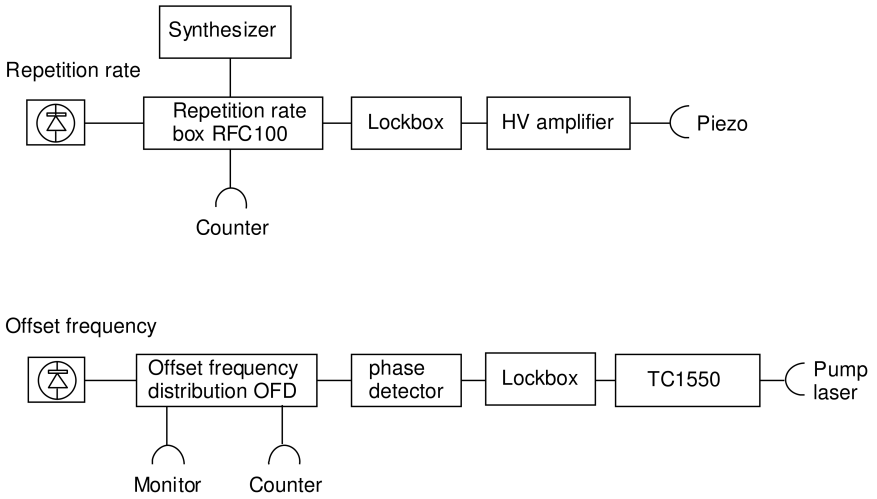

Figure 2.7: General overview of the locking electronics for repetition and offset frequencies.

control, an internal fast photodiode receives the signal, whose main part is amplified and fed to the repetition rate RCF100 unit, where its 10^{th} harmonic is mixed with the input signal at 10 MHz from the RFD10 unit. The resulting DC signal is lowpass filtered and supplied to a lockbox for phase locking. Next, a high voltage (HV) amplifier generates the high voltage for the intracavity piezo in the laser head.

In the case of the offset frequency control, the signal is detected with a fiber coupled photodiode, is lowpass filtered and amplified, and then fed into the monitor port of the offset frequency distribution OFD100 unit: the signal is passband filtered at 20 MHz and then fed to a digital phase detector for phase locking at 20 MHz.

Chapter 3

The astro-comb: characterization and performances

The last generation of high resolution astronomical spectrographs, together with the goal of measuring radial velocities lower than 1 m/s, has clearly shown the necessity of a calibration source capable of reaching the same level of accuracy or even better. Moreover, the need of monitoring for days or months an astronomical source makes the requirement of long-term temporal stability mandatory for a suitable calibration source. In 2007 the OFC has been identified as the near-ideal calibration source for high resolution astronomy [67, 68]. From then on, a great effort has been made to make the use of OFC as calibration source really feasible. Within this context, in this Thesis the apparatus, I projected and built for the calibration of near-IR high resolution spectrographs such as Giano, starting from a mode-locked Er-doped fiber laser frequency comb, is described.

3.1 The ideal calibration source

As pointed out in Section 1.2.2, current high resolution astronomical spectrographs could potentially monitor radial velocity changes down to a few cm/s if a suitable wavelength reference can be obtained. With such high level of precision and stability, some targets would become viable, such as the search for terrestrial mass planets in Earth-like orbits, direct measurement of

the acceleration of the universe and the variation of fine structure constant using quasar spectra. The ideal comparison spectrum would comprise a series of lines which [67]:

(i) have known wavelengths which are determined by frequency metrology;

(ii) are individually unresolved;

(iii) are resolved one from each other;

(iv) have uniform spacing;

(v) cover the entire wavelength range of operation of the spectrograph;

(vi) have nearly uniform intensity;

(vii) are stable over long-time scales;

(viii) do not reduce the signal-to-noise ratio (S/N) of the observed object.

Moreover, the calibration source should (ix) be exchangeable, in the sense that two indipendent sources should produce the same reference spectrum; it should (x) be easy to use, in the sense that the use should be nearly turn-key; and it should (xi) have a reasonably low cost.

3.1.1 Traditional calibration sources

The standard astronomical calibration source in the near-IR is the Th-Ar discharge lamp. The practical problems and limitations of this source can be visualized in Figure 3.1, which displays a part of the echelle spectrum of such a lamp taken with the Giano spectrometer [35]. The spectrum is dominated by prominent Ar lines, some of which are strong enough to produce spurious reflections and light ghosts in the spectrometer. The Ar lines are not accurate calibrators because their wavelengths depend on the current intensity and/or on the gas pressure inside the lamp (see, e.g., [69]). The Th lines are much more stable but are relatively weak and, most important, the number of lines decreases dramatically at wavelengths longer than 1200 nm. For example, no bright lines are detectable in the region between 1690 nm and 1720 nm (grating order 45 in the case of Giano).

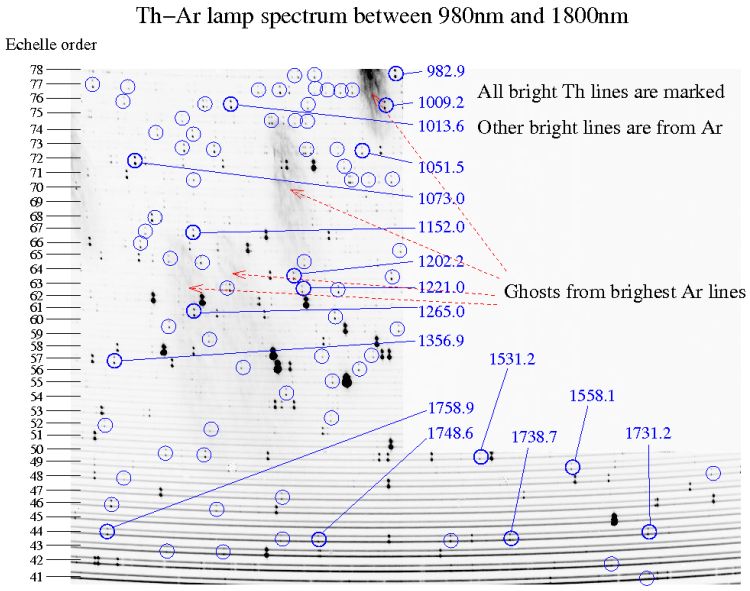

Figure 3.1: Part of the echelle spectrum of a Th-Ar lamp taken with the Giano spectrometer. For each order, two parallel spectra are visible because the instrument is fed by two fibers [35].

From the above list, it results that the Th-Ar lamp spectrum does not meet some crucial requirements for the ideal calibration source, such as to have lines resolved from each other, uniformly spaced and equally intense (iii, iv, vi), to cover the whole spectral range (v) and to guarantee stability over long time periods (vii).

3.1.2 OFC as calibration source

The OFC possibly satisfies all the listed requirements for the ideal calibration source. In the following, I will especially focus on the two most challenging requirements, i.e. lines resolved one from each other (iii) and spectral coverage (v), together with the request of a resonably low cost system (xi).

The simple conceptual scheme for the use of an OFC as the calibration source for an astronomical spectrograph is shown in Figure 3.2: the octave spanning spectrum generated by an OFC is fed into the echelle spectrograph via an optical fiber; a portion of the comb light is split and used for the repetition rate and offset frequency control, i.e. to know and control the comb frequencies. In practice, the spectrograph would be fed by two fibers (or more, as in the case of

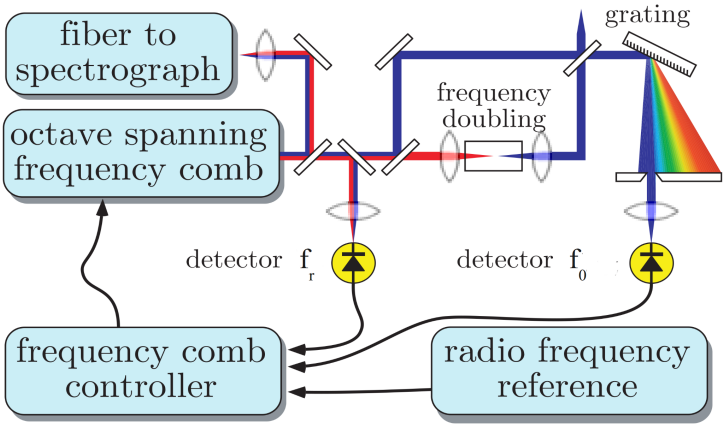

Figure 3.2: Conceptual scheme of the use of OFC for astronomical calibration: the comb is stabilized via the f_r and f_0 control and is then fed to the spectrograph via an optical fiber [67].

Giano), one carrying the science object light and the other carrying the comb light for calibration. The two spectra would be recorded simultaneously on the CCD, varying the intensity of the comb light, with a feedback mechanism, according to the changes in intensity of the observed object light. In this way, changes in weather conditions or small drifts in the spectrograph itself during the exposure, which usually cause distorsions of the wavelength scale, would affect the comb spectrum in the same way.

3.2 Optimal mode spacing

While the wavelength calibration precision available with an OFC clearly improves with increasing line density, on the other hand a too high density of lines would decrease the contrast between neighbouring lines and hence degrade the available precision: an optimal line spacing must exist.

To estimate the photon-limited available precision, we assume to use only one CCD exposure of the comb spectrum to calibrate the spectrograph; therefore, the dynamic range of the CCD pixels limits the comb S/N. A single unresolved comb line imaged on the CCD shows the instrumental profile (IP) of the spectrograph. If this profile is a Gaussian whose full width at half maximum (FWHM) is sampled by $n > 1$ pixels, the error (in terms of velocity) in the line's

position can be approximated as [70]:

$$\delta v \simeq A \frac{\mathrm{FWHM}}{\sqrt{n} \times \mathrm{S/N}} \,, \tag{3.1}$$

where S/N is the peak S/N per pixel across the line and the prefactor A depends on the functional form of the line profile and on the relationship between S/N and pixel intensity. If the noise level is constant across the line, it results that $A = 0.693$ for a Gaussian profile and $A = 0.798$ for a Lorentzian one [70]. Assuming, instead, that the photon noise is Poissonian and that this noise dominates the detector noise, it can be found that $A \simeq 0.41$ [67]. To determine the total velocity precision available from an entire echelle order, we first assume to have a comb line every 2.5 resolution element (intuitively the line density is high but two neighboring lines do not strongly overlap). If we have 2048 pixel per echelle order with a 3-pixel sampling of the FWHM, there are roughly $N = 272$ comb lines per order. For a peak S/N of 500 and a resolving power of 150000 (typical values for a visible high resolution spectrograph), the total calibration precision per echelle order is [67]:

$$\sigma_v \simeq \frac{\delta v}{\sqrt{N}} = \frac{0.41 \times 200 \text{ km/s}}{500 \times \sqrt{3 \times 273}} = 5.7 \text{ cm/s} \,. \tag{3.2}$$

From the above Equation we can see that a calibration precision of some cm/s can be obtained with comb lines spaced ~ 2.5 resolution elements. In the case of Giano, requiring a precision of some tens cm/s and considering that, with 2-pixel sampling (high resolution mode operation) and one comb line every, for example, 4 resolution elements, we have $N = 259$, $A \times \mathrm{FWHM} = 5$ km/s and S/N = 200, we find:

$$\sigma_v \simeq \frac{5 \text{ km/s}}{200 \times \sqrt{4 \times 259}} = 79 \text{ cm/s} \,. \tag{3.3}$$

From this intuitive calculation, we can infer that the optimal comb spacing lies around a line every $2-4$ resolution elements. In the following, I will give a more general mathematical derivation, which leads to a similar conclusion and allows us to determine the optimal spacing in the case of the Giano spectrograph.

3.2.1 Mathematical derivation

The limiting velocity precision to measure, at pixel i, a velocity change in a spectrum $F(i)$ with 1σ error array $\sigma_F(i)$ is given by [71]:

$$\frac{\sigma_v(i)}{c} = \frac{\sigma_F(i)}{\lambda(i)[\partial F(i)/\partial\lambda(i)]} \,. \tag{3.4}$$

This Equation states that a more precise velocity measurement is available from those pixels where the flux has a large gradient and/or the uncertainty in the flux is small. If we define $W(i) = [\sigma_V(i)/c]^{-2}$, the total velocity precision available from all pixels in a spectrum is:

$$\frac{\sigma_V}{c} = \frac{1}{\sqrt{\sum_i W(i)}} \,. \tag{3.5}$$

Considering that the spectrum is divided in echelle orders, the total velocity precision is obtained as a weighted average of that available for each order k:

$$\sigma_V = \frac{1}{\sqrt{\sum_k \sigma_V^{-2}(k)}} \,. \tag{3.6}$$

If we model the comb spectrum as recorded by the spectrograph writing the flux in each pixel, $F(i)$, as the product of an envelope function, $F_e(i)$, and a quickly varying "comb function", $f(i)$, which stays between 0 and 1, then the expected 1σ error array results:

$$\sigma_f(i) = \sqrt{f(i)F_e(i) + \sigma_d^2(i)} \,, \tag{3.7}$$

where $\sigma_d(i)$ is the detector noise at each pixel. Defining $\beta_d(i) = \sigma_d(i)/\sqrt{F_e(i)}$ as the ratio of the detector noise and photon noise at pixel i, the S/N ratio for each pixel can be written as:

$$\left(\frac{S}{N}\right)(i) = f(i)\sqrt{\frac{F_e(i)}{f(i) + \beta_d^2(i)}} \,. \tag{3.8}$$

If we assume that the envelope function, $F_e(i)$, is constant, so that all the comb modes have the same intensity, the comb function, $F_e(i)f(i)$, simply consists of a series of identical delta functions

spaced by the comb repetition rate. This spectrum is, then, convolved with the spectrograph's IP, which can be assumed to be Gaussian with a width specified by the resolving power R. If we also assume that the detector noise is the same at each pixel ($\sigma_d = \text{const}$), the array $\sigma_F(i)$ can easily be determined from Equation 3.7. To derive $\sigma_V(i)$ from Equation 3.4, we can express the derivative as the finite-difference derivative between successive pixels:

$$\frac{\partial F(i)}{\partial \lambda(i)} \simeq \frac{F(i) - F(i-1)}{\lambda(i) - \lambda(i-1)} \,. \tag{3.9}$$

Knowing the velocity precision available per pixel, we can calculate the total precision available using Equation 3.6 and summing over the spectral range of interest. As can be expected, the total precision strongly depends on the comb mode spacing. The simulation I computed for the variation of the total precision available, σ_V, as a function of mode spacing[1], expressed in GHz, is shown in Figure 3.3: the minimum of this function gives the optimum spacing, which lies between 15 and 20 GHz in the case of Giano. Considering also the cases of different high

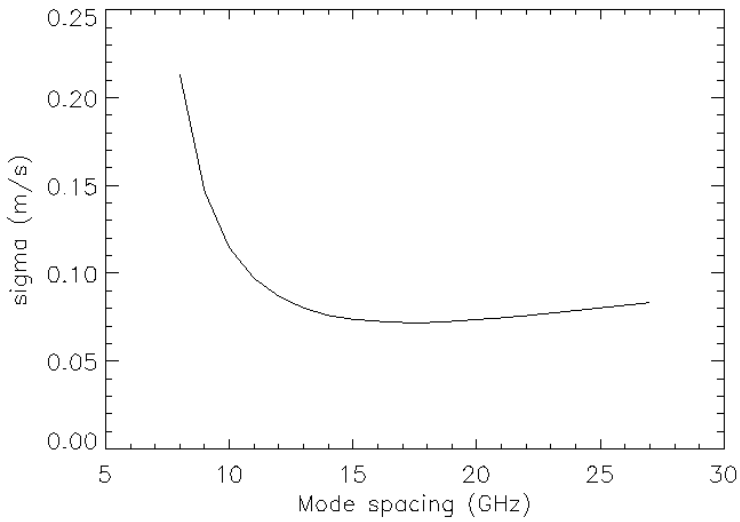

Figure 3.3: Behaviour of the total precision σ_V available with a comb as a function of the mode spacing, expressed in GHz. The value at each mode spacing has been obtained by summing over the wavelength range 1500−1650 nm.

[1] In the case of Giano, a single resolution element (in the case of 2-pixel sampling, i.e. $\Delta\lambda/\lambda = \Delta f/f = 2\times10^{-5}$) corresponds to a resolution of about $\Delta f = 4.5$ GHz at 1500 nm. The mode spacing in terms of frequency can thus be obtained by multiplying the spacing by Δf.

resolution spectrographs, as a "general" condition we can say for the optimum spacing f_r^{opt} [67]:

$$f_r^{opt} \simeq 3\Delta f \,, \tag{3.10}$$

where Δf is the spectrograph resolution in frequency at the midpoint of its wavelength range. The worsening in precision is rapid below f_r^{opt}, because the comb lines overlap, while it varies slowly above the optimum value. Nevertheless, a precision within a factor 2 of the optimum can still be achieved over the range $(0.5{-}5)f_r^{opt}$.

A simple general expression to infer the total velocity precision available at the optimum mode spacing over a spectral range of 200 nm results [67]:

$$\sigma_V^{opt} = 0.63 \left[\frac{500}{(\mathrm{S/N})_{\max}}\right] \left(\frac{1.5 \times 10^5}{R}\right)^{3/2} \mathrm{cm/s}\,. \tag{3.11}$$

In the case of Giano ($(\mathrm{S/N})_{\max} = 200$, $R = 50000$), we can compute $\sigma_V^{opt} \simeq 8$ cm/s, which is consistent with the simulation in Figure 3.3.

3.2.2 Additional sources of error

While the target of reaching a photon-limited precision of 10 cm/s or better can easily be obtained, in principle, with a frequency comb, the fact that this value results 4–5 orders of magnitude smaller than the pixel size for present high resolution spectrographs means that systematic effects due to the specrograph and the detector system need to be taken into account and mitigated. The main effects are [67]: (a) inhomogeneities in the intensity profiles created by the fibers which carry the astronomical object and comb signals, (b) variations of the spectrograph IP across the CCD, (c) inaccuracies in the echelle grating's line markings, (d) variation in pixel size and separation across an individual CCD array, (e) intra-pixel sensitivity variations, (f) CCD temperature variations. Most of the listed effects ((b) - (e)) are ascribable to spectrograph/detector response: due to the comb property to have equidistant lines whose frequencies are known a priori with an accuracy better than the required resolution, the spectrograph/detector response can be accurately characterized with the comb itself. In such a way,

the comb becomes not only a calibration source capable to guarantee in principle a resolution better than 100 cm/s, but also a mean to characterize and correct many systematic errors so that it can be used in practice to reach this resolution. Error sources like (a) (pre-slit effects) need, instead, to be estimated and mitigated with dedicated systems, such as light-scrambling in the fiber [39].

A limitation to the use of the comb spectrum as the reference to mitigate systematic errors can be the possible asymmetry and/or variation of the comb modes themselves (called "repetition rate noise"). Nevertheless, due to the low spectral width of individual comb modes (less than 1 MHz), this source of uncertainty can become relevant just for the goal of getting below a 10 cm/s precision (which is not necessary in our case for the terrestrial planet detection), when the comb mode linewidth is larger than the required resolution. In this case, additional techniques for reducing the mode linewidth can be employed [72].

3.3 Filtering the comb

In Section 3.1 I listed the characteristics of the ideal calibration source. As I stated in Section 3.1.2, one of the most challenging requirements is to have comb modes resolved one from each other. In Section 3.2.1 I computed an optimum mode spacing between 15 and 20 GHz; typical values for commercial near-IR Er-doped frequency combs are, instead, of the order of 100−250 MHz[2]. While a technology capable to generate a near-IR octave spanning comb with directly a repetition rate higher than some GHz is presently not available, a possible solution is to spectrally filter out the unwanted modes with an external Fabry-Perot (F-P) cavity with a convenient free spectral range (FSR) [73, 74, 49].

The ideal situation is depicted in Figure 3.4-top: the red dotted lines represent the comb modes, one every f_r, while the black curve is the F-P transmission profile for a mirror reflectivity $R = 95\%$ in the case of a free spectral range $\mathrm{FSR} = mf_r$ with a filtering ratio $m = 4$, i.e. when one comb mode every four is transmitted by the filtering cavity. As can be easily foreseen, a good suppression of attenuated modes is essential for calibration purposes, because, for the ultimate

[2]For the apparatus discussed in this Thesis we have a repetion rate $f_r = 100$ MHz.

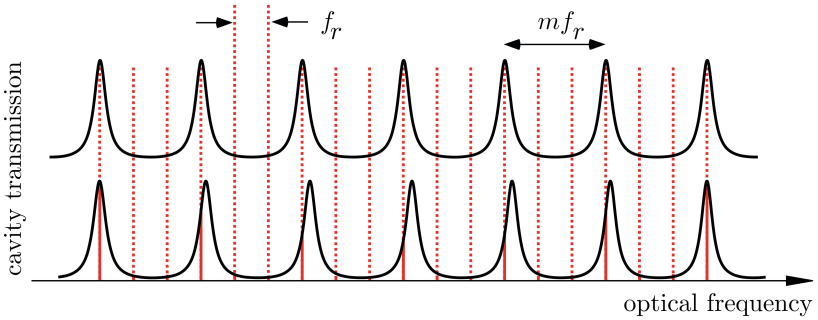

Figure 3.4: Filtering of the comb modes (red lines), spaced by a frequency f_r, with a F-P cavity (black curve) in the ideal case (i.e. perfect matching) on the top, and in the real case (i.e. considering cavity dispersion) on the bottom [75].

resolution, individual comb lines are deconvoluted with the known point spread function[3] of the spectrograph. Insufficient suppression of side modes that lie within the resolution of the spectrograph would result in systematic shifts of the calibration source. This problem can be overcome using a high finesse F-P cavity: sharper cavity transmission peaks ensure a higher suppression of side modes.

On the other hand, statistical calibration uncertainties are reduced when a large optical bandwidth is available. In this case, as depicted in Figure 3.4-bottom, imperfectly compensated group velocity dispersion (GVD, see Appendix A.3) of the cavity mirror coatings generates small mismatches of the filter mode spacing so that while the transmission peaks and the wanted comb modes are well overlapped at some wavelengths, they walk off one another at other wavelengths. This effect is more detrimental in the case of high finesse cavities, which use mirrors with dispersive coatings, as dielectric ones. Instead, other coatings, such as metallic ones, do not present strong dispersion in a wide spectral range but reflectivities higher than 98% with some degree of transmission cannot be achieved with such coatings, contrary to what is technologically possible with dielectric ones. The requirements are, hence, conflicting: high finesse cavity for good side mode suppression, low finesse cavity to reduce the group velocity mismatch. The approach that has been proposed [75] to overcome this restriction has been to combine more than one low finesse F-P cavities in series in a way that the total finesse amounts to that required for a single

[3]The point spread function (PSF) of an instrument represents the response of the optical system to an impulse function. From the spectrograph point of view, comb modes are seen as delta functions.

high finesse cavity. Moreover, dispersive media inside the cavity (such as air) can cause the FSR of the cavity to vary across the spectrum, when the filtered spectrum is hundreds of nanometers wide.

3.3.1 F-P cavities in series

The transmission function of a single F-P cavity made of two mirrors of reflectivity R at a distance L without dispersion is:

$$T(f, R, L) = \frac{(1-R)^2}{(1-R)^2 + 4R\sin^2(2\pi f L/c)} \,. \tag{3.12}$$

To take dispersion into account, the length L needs to be replaced by the optical path length. The transmission profile is made of a regular grid of peaks, each $\delta f = \mathrm{FSR}(1-R)/\pi$ wide, with free spectral range $\mathrm{FSR} = c/2L$. If the FSR is fixed to be exactly m times the comb repetition frequency, $\mathrm{FSR} = m f_r$, then the cavity transmits a mode every m modes.

A basic parameter used to characterize the filtering performance is the level of side mode suppression. We can define it as the residual transmitted power of the closest mode to the transmitted one: $\rho = T(f_r, R, L)$ [75], i.e. the residual transmission at a frequency distance f_r from the transmitted comb mode. The spectral shift due to the presence of the remaining side modes can, hence, be computed as the intensity-weighted average between the wanted mode (weight 1) and the adjacent unwanted mode (weight ρ):

$$\Delta f = \frac{0 + \rho f_r}{1 + \rho} \simeq \rho f_r \,. \tag{3.13}$$

The required 10 cm/s precision in radial velocity measurements corresponds to a frequency precision $\Delta f/f = v/c = 3 \times 10^{-10}$. From Equation 3.13, the value of the needed suppression for the first adjacent unwanted mode can be computed as:

$$\rho \simeq \frac{\Delta f}{f}\,\frac{f}{f_r} \,. \tag{3.14}$$

If we start with a $f_r = 100$ MHz repetition rate comb at $f = 200$ THz (1500 nm), to fulfill the

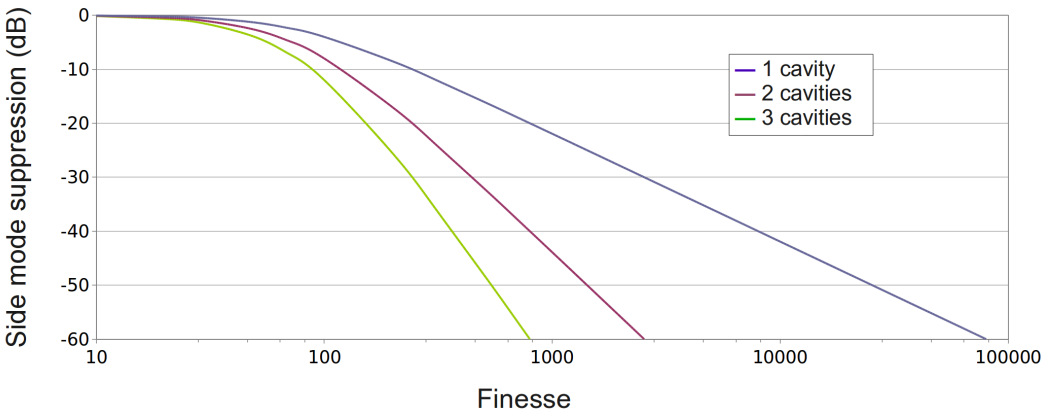

Figure 3.5: Side mode suppression (espressed in dB) vs. cavity finesse in the case of one single cavity (blue), two cavities in series (purple) and three cavities in series (green) with FSR = 16 GHz and $f_r = 100$ MHz. The value of ρ in dB at each finesse (i.e. reflectivity) has been obtained from the ρ definition ($\rho = T(f_r, R, L)$) as $\rho[\text{dB}] = -10 \log \rho$.

required precision we would need, at least, a suppression $\rho = -32$ dB.

We can, now, compute from Equation 3.12 the cavity finesse, defined as $F = \pi/(1-R)$, requiring a side mode suppression of -32 dB: in the case of a single filtering cavity from $f_r = 100$ MHz to FSR = 16 GHz (filtering ratio $m = 160$) a finesse of $F = 3000$ ($R = 99.9\%$) would be required. Such a high finesse is achievable for single mode lasers, but is impossible to obtain for broadband operation, due to mirror coating dispersion [76]. If we suppose to use more than one F-P cavity in series, the total transmission is given by the product of each single cavity transmission function. Thus, we can obtain the same level of side-mode suppression with two F-P cavities of FSR = 16 GHz in series with $F = 500$ ($R = 99.4\%$) each one or with three F-P cavities in series of FSR = 16 GHz with $F = 250$ ($R = 98.7\%$) each one. In Figure 3.5 I computed the variation of the side mode suppression (espressed in dB) varying the cavity finesse in the cases of one single cavity (blue curve), two cavities in series (purple curve) and three cavities in series (green curve) with FSR = 16 GHz and $f_r = 100$ MHz ($m = 160$).

3.3.2 Optimum mirror radius of curvature

The side mode suppression ρ has been estimated from Equation 3.13 with the assumption of perfect spatial mode coupling between the comb modes and the fundamental mode of the

filtering cavities. In a more realistic situation, due to non-perfect mode matching, high order transversal modes of the filtering cavities are present. On one hand, they may get close to or even coincide with comb modes that have to be suppressed, causing a general worsening of the achievable suppression. An accurate optical control of the input Gaussian mode from the comb to match the cavity fundamental mode (see Section 4.2.2) minimizes such problem. On the other hand, transversal modes can coincide with the wanted transmitted modes, causing a frequency calibration mismatch of the spectrograph. A suitable choice of the radius of curvature of the cavity mirrors can overcome such coincidences.

Transverse modes are the set of solutions of the wave equation inside a cavity; in the paraxial approximation (which is applied when the wave propagates in a small cone around the propagation direction), they are described by the Gaussian-Hermite polynomials and the mn-th order mode (with m and n integers) is usually indicated as TEM_{mn} (transverse electromagnetic mode of order mn). Defining the quantity $g_i = 1 - L/r_i$, where r_i is the radius of curvature of the i-th mirror and $L = c/2mf_r$ is the cavity length, the resonance frequencies of the axial-plus-transversal modes in the cavity are given by [77]:

$$f_{qmn} = \frac{c}{2L}\left[q + (n+m+1)\frac{\arccos(\sqrt{g_1 g_2})}{\pi}\right], \tag{3.15}$$

where q is an integer (axial mode number) obtained imposing the resonance condition, i.e. for a standing-wave cavity the total round trip phase shift is an integer multiple (q) of 2π. The cavity fundamental mode (axial mode) is obtained by setting $q = 1$ and $m = n = 0$.

Varying the factors g_1 and g_2 in Equation 3.15, i.e. the radius of curvature of the two cavity mirrors, it is possible to find the configurations which guarantee that transversal modes (m, $n > 0$) do not occur at integer multiples of f_r.

In Figure 3.6-left, I show a simulation of a good arrangement for cavity mirrors (four consecutive FSRs are shown): I considered the case of a hemifocal cavity of FSR = 16 GHz with one plane mirror ($g_1 = 1$) and one concave mirror with radius of curvature $r_2 = 100$ mm ($g_2 = 0.906$) and I took into account the first four transversal modes ($q = 1$, $m + n = 1, 2, 3, 4$). In the simulation, I assumed that the transversal modes $m + n = 1, 2, 3, 4$ are intensity depressed relatively

to the fundamental mode by a factor -10, -20, -30, -40 dB, respectively, which corresponds to an exponential intensity decrease with growing of the mode order. It can be seen that, in the case of a hemifocal cavity with one mirror of radius of curvature of 100 mm, none of the transversal mode frequencies is coincident with that of a comb mode. To better observe this fact, in Figure 3.6-right I show an enlargement of the first transverse mode ($m + n = 1$) as well: as can be seen, the mode lies between two comb modes, so that its contribution to the transmission profile becomes negligible.

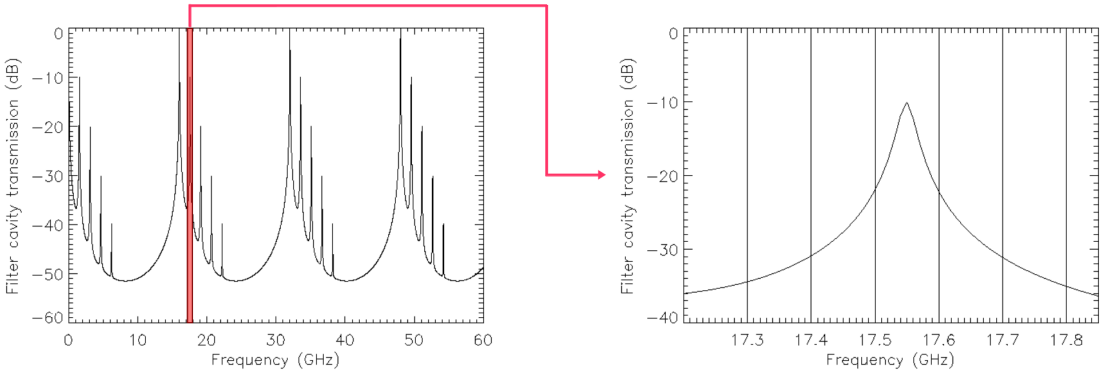

Figure 3.6: Left: simulation of the behaviour of the first four transversal modes ($m+n = 1, 2, 3, 4$) with respect to the fundamental mode for a hemifocal cavity with a radius of curvature $r = 100$ mm for the second mirror and FSR = 16 GHz. Right: enlargement of the first transversal mode.

3.4 Dispersion

As already pointed out, dispersion in a cavity is an important source of error that needs to be taken into account, because it determines the spectral bandwidth over which cavity modes and comb components can be overlapped simultaneously. The generalities on dispersion and the definitions of group and phase velocities are described in Appendix A.3.

The filtering cavities required for the astro-comb realization are affected by dispersion problem in two different ways: first of all because of the imperfectly compensated group velocity dispersion of the mirror coatings[4], secondly for the dependence of the refraction index n of the intracavity

[4]This condition arises only in the case of dielectric coated mirrors; metallic coated ones are virtually free from this kind of dispersion.

medium (air) on wavelength. Both problems become significant just in the case of broadband operation of the filtering cavities, which is the case of the astronomical application I discuss in this Thesis.

3.4.1 Dispersion due to mirror coating

While comb modes are evenly spaced in the frequency domain by a fixed quantity, f_r, the cavity mode spacing is frequency dependent [78]:

$$\mathrm{FSR} = \frac{c}{2L + (c/\pi)\partial\phi/\partial f} \,, \tag{3.16}$$

which is reduced to the known expression $\mathrm{FSR} = c/2L$ for negligible dispersion. The degree to which the cavity FSR is frequency-dependent is determined by the dispersion term $(c/\pi)\partial\phi/\partial f$, where $\phi(f)$ is the round trip phase shift introduced by reflections of the cavity mirrors.

If cavity modes and comb modes are exactly overlapped at a given frequency f_l, the frequency shift, induced by dispersion, between the m-th cavity mode from f_l and the m-th comb component from f_l is given by [53]:

$$\Delta f_m = \int_{f_l}^{f_m} \left(\frac{\mathrm{FSR}(f)}{f_r(f_m)} - 1 \right) df \,, \tag{3.17}$$

where f_m is the frequency of the m-th comb mode. When $\Delta f_m = k f_r$ ($k = ..., -2, -1, 0, 1, 2, ...$), the m-th comb mode overlaps with the $(m+k)$-th cavity mode. From Equation 3.17 the behaviour of FSR with frequency can be virtually inferred by scanning the f_r value[5]. Differentiating Equation 3.17 with respect to the comb mode number, it results:

$$\mathrm{FSR}(f_t) = f_r(f_t) + (f_t - f_l)\frac{d}{df_t} f_r(f_t) \,, \tag{3.18}$$

where the values of f_r that give rise to cavity transmission peaks at frequencies f_t are used to determine the frequency dependence of cavity FSR. The quantity used to take into account the degree of dispersion is the group delay dispersion (GDD), computed as the derivative of the

[5] In fact, comb lasers are ideal sources for broadband characterization of dispersion in optical instrumentation (see, e.g., [79]).

inverse of the frequency-dependent FSR:

$$\mathrm{GDD}(f) = \frac{d}{df}\,\frac{1}{\mathrm{FSR}(f)}\,. \tag{3.19}$$

3.4.2 Dispersion due to intracavity medium

When the filtering cavity is placed in a dispersive media like air, the frequency dependence of refraction index causes the FSR to sligthly vary at different wavelenghts due to the different experienced optical path. Due to the difficulty of measuring accurately the dependence of the air refraction index on wavelength, a large number of semi-empirical formulae have been developed during the last century [80, 81, 82, 83].

Defining the air refractivity as the departure of the refractive index from unity, the refractivity of standard air ($T_{as} = 15°$, $P_{as} = 101.325$ Pa, 0% humidity, 450 ppm CO_2 content) is given by [83]:

$$(n_{as} - 1) = \frac{k_1}{k_0 - \sigma^2} + \frac{k_3}{k_2 - \sigma^2}\,, \tag{3.20}$$

where $k_0 = 238.0185\ \mu\mathrm{m}^{-2}$, $k_1 = 5792105\ \mu\mathrm{m}^{-2}$, $k_2 = 57.362\ \mu\mathrm{m}^{-2}$, $k_3 = 167917\ \mu\mathrm{m}^{-2}$ and $\sigma = 1/\lambda$ is the inverse of vacuum wavelength expressed in μm. In the opposite case of pure water vapor at standard condition ($T_{ws} = 20°$, $P_{ws} = 13.33$ hPa, 100% humidity), it results [83]:

$$(n_{ws} - 1) = \mathrm{cf}\,(w_0 + w_1\sigma^2 + w_2\sigma^4 + w_3\sigma^6)\,, \tag{3.21}$$

where $w_0 = 295.235\ \mu\mathrm{m}^{-2}$, $w_1 = 2.6422\ \mu\mathrm{m}^{-2}$, $w_2 = -0.032380\ \mu\mathrm{m}^{-4}$, $w_3 = 0.004028\ \mu\mathrm{m}^{-6}$ and $\mathrm{cf} = 1.022$ is the correction factor one finds by fitting the calculations to the measurements [83]. A more realistic situation is the case of moist air, where there is some contribution from dry air and some from water vapor. We first introduce the saturation pressure of water: $P_S = -10474 + 116.43 - 0.43284\,T^2 + 0.00053840\,T^3$, where T (in °K) is the ambient temperature; the partial pressure of dry air, thus, results: $P_P = P - P_S$, where P is the ambient pressure. In the case of 20° and 100% humidity, we have: $P_S = 24.1$ Pa. An approximate expression for the

total refractivity in case of moist air, thus, results:

$$(n-1) = \frac{P_P}{P_{as}}\,(n_{as}-1) + \frac{P_s}{P_{ws}}\,(1-n_{ws})\,. \tag{3.22}$$

In Figure 3.7 I compute the behaviour with wavelength of $(n-1)/(n(1\mu\text{m})-1)$ between 0.8 and 2.5 μm ($P = P_{as}$) for the case of dry air (n_{as}), water vapor (n_{ws}) and moist air (n).

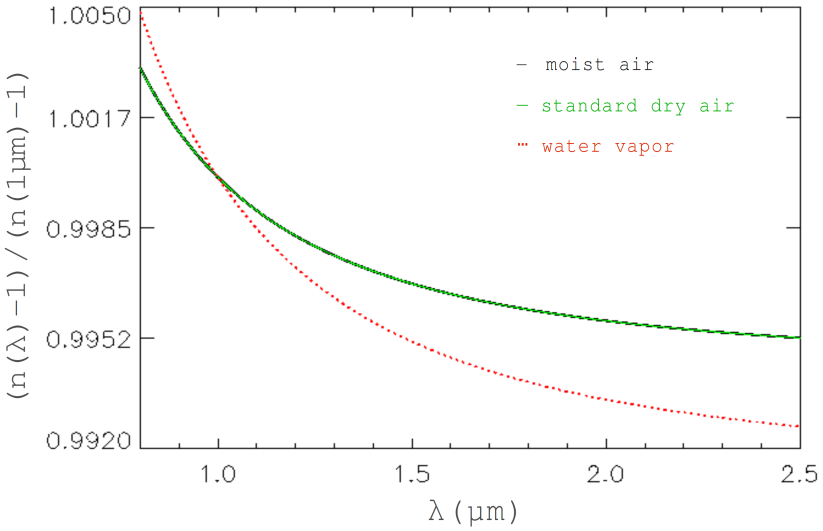

Figure 3.7: Behaviour of $(n-1)/(n(1\mu\text{m})-1$, $(n_{as}-1)/(n_{as}(1\mu\text{m})-1)$ and $(n_{ws}-1)/(n_{ws}(1\mu\text{m})-1$ between 0.8 and 2.5 μm.

To infer which is the frequency shift experienced in a given spectral range by the cavity FSR due to the frequency dependence on n, we can differentiate the FSR Equation, FSR $= c/2nL$ (without the dispersion term due to the mirror coating and substituting the cavity length L with the optical path nL): $d(\text{FSR})/\text{FSR} = dn/n$. We can, hence, compute the frequency shift ΔFSR, moving from λ_1 to λ_2, as:

$$\frac{\Delta\text{FSR}}{\text{FSR}} = \frac{n(\lambda_2)-n(\lambda_1)}{n(\lambda_1)}\,. \tag{3.23}$$

For the limited spectral range between 1.5 and 1.65 μm (the wavelength range emitted from an Er-doped OFC without octave spanning amplification), we obtain ΔFSR = 7 MHz, which is a resonable shift for a 100 MHz repetition frequency, so that in this case the filtering cavities can be placed in air. In the case of octave spanning spectrum (1−2 μm), the shift becomes ΔFSR = 70

MHz, which means that, if cavity modes and comb modes are superimposed at 1 μm, at 2 μm the wanted mode is almost completely suppressed, while the first adjacent one is transmitted. Thus, in this case corrections to $n(\lambda)$ must be done. Alternatively, we can put the cavity under vacuum conditions. I note that, if we start from higher repetion rate (as, for example, $f_r = 250$ MHz), the effect of $n(\lambda)$ on the transmitted mode can be considered negligible.

3.4.3 Spectral bandwidth

The spectral bandwidth of a cavity refers to a spectral window in which the cavity has a sufficiently high finesse (imposed by the conditions described in Section 3.3.1) and, at the same time, a nearly uniform FSR. Looking for an astro-comb working roughly between 1 and 2 μm, we can infer which is, as maximum as possible, the spectral bandwidth around 1500 nm (the center of spectral range of operation) with high finesse and low dispersion losses.

To this aim, it is necessary to derive which is the GDD value corresponding to the maximum allowed spectral shift of a transmission peak with respect to the wanted comb mode to still guarantee a good side mode suppression. Suppose we have GDD = 0 at a frequency f_1; a reasonable request starting with a 100 MHz repetition rate comb would be to ask for a spectral bandwidth $\Delta f = f_2 - f_1$ so that the FSR varies of 0.1% (16 MHz over FSR = 16 GHz). From Equation 3.16, we have that FSR(f_1) is simply FSR(f_1) = $c/2L$, with $L = 9.735$ mm (due to the fixed condition GDD = 0 at f_1), while, for FSR(f_2) to be FSR(f_2) < 16.016 GHz, we can infer the maximum value of the term $(\partial\phi/\partial f)_{f_2}$. Integrating Equation 3.19, we can, hence, calculate the maximum allowed GDD: asking for a 1 μm-wide bandwidth from 1 to 2 μm, the requirement would be GDD < 150 fs^2. This rough estimate gives us an upper limit for the dispersion allowed by custom-made mirrors to be used for the astro-comb filtering cavities.

3.5 Cavity mirrors

To produce an octave spanning comb spectrum with a 16 GHz mode spacing, I considered three different solutions by taking into account the above requirements for the cavity mirrors in terms of reflectivity, dispersion and spectral coverage. I have analyzed their relative feasibility,

and two of them were implemented. The first possibility is to use two F-P cavities in series, with dielectric coated mirrors having a reflectivity of 99.5%: as will be explained in Chapter 4, the coating dispersion causes a GDD higher than required in the OFC spectral range of operation (1−2 μm), so that it has been possible to filter the comb spectrum just in the limited range 1.5−1.65 μm. In this case, to obtain an octave spanning spectrum, it is necessary to broaden the spectrum after the filtering process using a non-linear frequency conversion in a highly non-linear fiber. This is the approach followed, up to now, for other similar systems (see, e.g., [85, 86]). The system requirements in terms of optical layout and available power will be described in detail in Chapter 4, while in Chapter 5 I will describe the final system layout in the case of dielectric mirrors cavities and the experimental results I obtained.

In Chapter 6, I will present a new and original approach: to overcome the problem of the coating dispersion, I propose to filter directly the octave spanning comb spectrum with silver coated mirrors. In this case, the advantage of having virtually no dispersion coating problems (but the intracavity dispersion needs to be taken into account) is paid with the necessity of three F-P cavities in series due to the lower mirror reflectivity. Since the beginning, I considered the feasibility of both this two approaches simultaneously, but I was forced to give up the metallic mirrors approach since no optics supplier provided suitable mirrors at the time. I was, at last, able to find suitable metallic mirrors just some months ago, hence I will discuss the results obtained up to now.

A third solution I considered has been to use cavities made of two Brewster angle prism retroreflectors, which in principle guarantees high finesse and no dispersion in a wide spectral range (larger than 1−2 μm) [84]. The characteristics of this approach and its limitations, which made it, at the end, not suitable for our application, are described in the following Section.

3.5.1 Prism retroreflectors

The major advantage of using retroreflectors prisms at Brewster angle is that the bandwidth of the cavity is limited only by the spectral regions of low internal transmission loss of the material used to construct the prisms. Using fused silica, the whole range of our interest ($1-2$

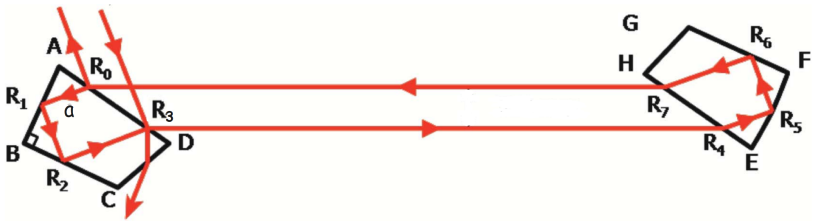

Figure 3.8: Top view of prism cavity design.

μm) can be covered. Figure 3.8 shows a top view of the typical cavity design.

First of all, let's see how such a prism works as a total reflector. A light ray enters the long face (AD) at R_0 with an external angle of incidence nearly at Brewster angle θ_B ($\theta_B = \tan^{-1} n$, where n is the refraction index of fused silica) and with an internal angle of incidence equal to the complement of θ_B. The internal ray strikes face AB at R_1 with an angle of incidence equal to 45°, so that $\angle$DAB = 135° - θ_B. As long as n is greater than $\sqrt{2}$, this ray will undergo total internal reflection when it strikes side AB. It will, then, propagate to the next side (BC) and experience a second total internal reflection off this face at R_2 with an angle of incidence equal to 45° as long as $\angle$ABC = 90°. This ensures that this reflected ray, R_2R_3, is exactly parallel in the horizontal plane to the ray incident on side AB, R_0R_1, and this ray will leave the prism at Brewster angle for the prism-to-air interface at R_3, which is just the complement of Brewster angle for the air-to-prism interface. The prism exiting ray is parallel to the incident one. By the law of sines, the ray will be centered on the AB face if the length AR_0 is given by:

$$\frac{a}{2}\frac{\sin 45°}{\sin\theta_B} = \frac{a}{2\sqrt{2}n}\sqrt{1+n^2}\,, \tag{3.24}$$

where the second equality results from $\tan\theta_B = n$. Likewise, the propagation distance R_0R_1 is given by:

$$\frac{a}{2}\frac{\sin(135° - \theta_B)}{\sin\theta_B} = \frac{a}{2\sqrt{2}}\left(1+\frac{1}{n}\right)\,. \tag{3.25}$$

The propagation distance R_1R_2 is $a/\sqrt{2}$ while the distance R_2R_3 is:

$$3(R_0R_1) - (R_1R_2) = \frac{a}{2\sqrt{2}}\left(1+\frac{3}{n}\right)\,. \tag{3.26}$$

Thus, the total path inside each prism is $L_p = \sqrt{2}\, a\, (1 + n^{-1})$. Therefore the distance R_3A is three times R_0A and, in order to mantain the maximum aperture, the distance AD should be:

$$\mathrm{AD} \;\geq\; 4(R_0A) = \frac{2a}{\sqrt{2}\sin\theta_B} = \frac{2a\sqrt{1+n^2}}{\sqrt{2}n}\,. \tag{3.27}$$

The aperture will be mantained if BC $\geq$ AB. For $n \leq 3$ (which is the case of fused silica, for which $n = 1.45$) it is preferred to take $\angle\mathrm{BCD} = 3\theta_B - 45°$. This allows the input ray to the cavity, which strikes surface AD at R_3 near Brewster angle, to leave the prism by striking surface CD near Brewster angle and minimize reflections and thus scattered light inside the prism. In this case, the prism has $\angle\mathrm{CDA} = 180° - 2\theta_B$, $\angle\mathrm{BCD} = 2\theta_B - 45°$ and it results:

$$\mathrm{BC} \;=\; a\,\frac{5 + 3n + n^2 - n^3}{(1+n)(4n - n^2 - 1)}\,, \tag{3.28}$$

$$\mathrm{CD} \;=\; a\left[\frac{\sqrt{2}\,(1+n^2)^{3/2}}{n(n+1)(4n - n^2 - 1)}\right]\,. \tag{3.29}$$

For what concerns the prism size, bulk scattering and absorption loss scale linearly with the horizontal size of the prisms, so that one would like to keep them as small as practical for that issue. On the other side, fabrication and alignment sensitivities scale inversely with the size of the prisms and also diffraction losses limit the size. A good compromise can be found by making the vertical height of the order of a.

An optical cavity is formed by facing two such retroreflectors toward each other such that corresponding faces are nearly parallel (see Figure 3.8). Vertices E, F, G, H in the second prism correspond to A, B, C, D, respectively, in the first prism and the intersection points R_4, R_5, R_6, R_7 correspond to R_0, R_1, R_2, R_3. Let L_g be the distance along the optical axis from Brewster face AD to Brewster face EH. The prism must be placed such that a ray leaving R_3 at Brewster angle will strike R_4, which is the point on the second prism that corresponds to R_0. Such a cavity would be at the borderline of optical stability, so that to form a stable optical cavity some focusing element is needed. A convenient approach is to construct a convex curved surface on one face, for example on face EF centered in R_5 with radius of curvature R_c. The effective focal length of the prism retroreflector, thus, result $R_c/(2\sqrt{2}n^3)$ on tangential plane and $R_c/\sqrt{2}n$ on

sagittal plane [84]. To form a stable optical cavity, the prism separation L_g must satisfy the condition:

$$L_g < \frac{R_c - \sqrt{2\,L_p}}{\sqrt{2}\,n^3}\,. \tag{3.30}$$

The adequate prism dimensions are determined by the required FSR. Neglecting any type of dispersion, we have that:

$$\mathrm{FSR} = \frac{c}{2\,(nL_p + L_g)}\,. \tag{3.31}$$

In a more comprehensive analysis, the dependence of FSR on wavelength due to the variation of n needs to be taken into account:

$$\mathrm{FSR}(\lambda) = \frac{c}{\left[L_0 - 2\lambda\left(\frac{dn}{d\lambda}\right)\left(L_p + \frac{dL_p}{dn} + \frac{dL_g}{dn}\right)\right]}\,, \tag{3.32}$$

where $L_0 = 2[L_g + nL_p]$ is the round trip optical path length. Nevertheless, considerations by using Equation 3.31 are sufficient for our purpose, which is the study of the feasibility of using such kind of filtering cavities.

The difficulty in using this kind of cavities arises when very short cavity lengths are required. For example, in the case of a FSR of 20 GHz and a manageable value of L_g of 1 mm, it results a L_p value of 4.46 mm. In this case, we find the results shown in Table 3.1 for the prism angles and facets dimensions. In addition, by considering the stability condition (Equation 3.30), we can infer $R_c > 24$ mm. The required high optical tolerances for prisms with dimensions and

AB	1.87 mm
AD	3.21 mm
BC	2.37 mm
CD	1.50 mm
$\angle$ABC	$90°$
$\angle$DAB	$135° - \theta_B = 79.6°$
$\angle$CDA	$180° - 2\theta = 69.2°$
$\angle$BCD	$3\theta_B - 45° = 121.2$

Table 3.1: Prism retroreflector parameters.

angles such of those reported in Table 3.1 are difficult to achieve in the manufacturing process, as declared by the supply companies. Therefore, this approach cannot be followed for the present astro-comb application, while is a good alternative option to mirror cavities at lower FSR (see [84]), when high finesse and wide spectral range of operation are needed.

3.6 State of the art for comb filtering with F-P cavities

In this Section, I will outline the main results obtained by other research groups in the field of astronomical application of laser comb. In fact, since some years a few research groups are working on the use of OFC as the calibration source for high resolution astronomical spectrographs.

The only approach that has been developed during last years is to filter a limited portion of the comb spectrum with F-P cavities in series made of dielectric coated mirrors, in the visible or in the near-IR domain, and then to spectrally broaden it via a HNLF, although no octave spanning astro-comb has been generated yet. The idea of using a comb for this astronomical application has been proposed nearly at the same time in 2007 by Hänsch group at Max Plank Institute of Quantum Optics (MPQ) in Munich [67] and by Diddams group at National Institut of Standards and Technology (NIST) and Center for Astrophysics and Space Astronomy at University of Colorado (Boulder) [68].

Each group developed the common idea in different ways. In Munich they were building up a system for visible wavelengths to be placed at the HARPS spectrograph [75, 86, 38] (and they are designing an analogous system for the planned 42 m E-ELT[6] telescope where the proposed CODEX spectrograph will be placed [88]). They started with an Yb-doped fiber frequency comb with a repetition rate of $f_r = 250$ MHz and a central wavelength of 1030 nm. A nearly 10 nm wide comb spectrum around 1030 nm is filtered with two F-P cavities in series, the first with $\mathrm{FSR}_1 = 2$ GHz and the second with $\mathrm{FSR}_2 = 18$ GHz; each cavity is tilt-locked by mean of a continuous wave laser superimposed to the comb light (with orthogonal polarization), which is in turn phase-locked to a comb mode itself. To obtain a comb spectrum at optical wavelengths,

[6] http://www.eso.org/public/teles-instr/e-elt.html.

a further step is necessary, which is frequency doubling of comb light in a periodically poled potassium-tytanil-phosphate crystal to generate light centered at 514.9 nm. In such a way they were able to calibrate one echelle order of HARPS spectrograph (instead of 72 orders). From Equation 3.1 they estimated a statistical uncertainty of the comb calibration (assuming Gaussian line profile) of 15 cm/s, which corresponds to the photon noise limit in the determination of lines position. They plan to reduce this calibration uncertainty by using all the 72 echelle orders. To this aim, the spectral broadening is mandatory. They reported the attempt to broaden the spectrum in a non-linear photonic crystal fiber (PCF) to achieve a spectral coverage of 22 echelle orders (equivalent to 110 nm), but they concluded that the broadened spectrum does not improve nor reproduce the results obtained for a single echelle order, since the broadening stage seems to introduce instability in line profile and position [38]. Moreover, they measured for the first time the contribution of the CCD pixel irregularities to the calibration curve by scanning over the CCD pixels individually slightly varying the offset frequency [86]. They also analyzed the systematic calibration error sources (inhomogeneous illumination of the fiber input facet and interference between each frequency component and spatial fiber modes), which cause a shift in the barycenter of the beam entering the spectrograph [86].

At NIST, instead, they built a system in the near-IR, starting with an Er-doped fiber frequency comb centered at 1550 nm with $f_r = 250$ MHz and filtering it with two identical F-P cavities with FSR = 12.5 GHz [85], with the aim of using this system as the calibration source for the University of Florida's FIRST spectrograph [89]. They filtered a nearly 50 nm wide portion of comb spectrum around 1550 nm with two cavities of finesse $F = 2000$ ($R = 99.8\%$) which corresponds to a -38 dB side mode suppression for the single cavity. They introduced two semiconductor optical amplifiers and a high power EDFA between the cavities (in this case the second cavity does not have power losses due to mode filtering since it has the same FSR as the first cavity) to obtain 400 mW of power after the filtering process for the broadening in a HNLF (they used a silica-based HNLF with a dispersion slope of +0.019 ps^2/(km nm), a non-linear coefficient of 30/(W km) and zero dispersion at 1550 nm [90]). In this way they generated a comb spectrum between 1380 and 1820 nm, covering the H-band transmission window of the

Earth's atmosphere. Optically heterodyning the 12.5 GHz spaced comb with a tunable cw laser, they were able to measure the suppression of the 250 MHz offset modes, the asymmetry in mode suppression and how the mode suppression varies with wavelength. They observed a general degradation of the side mode suppression, measuring values between -20 (at 1380 nm) and -45 dB (at 1570 nm) over the generated spectrum, while they reached a -60 dB suppression after the second F-P cavity. They envisaged several reasons for this observed general worsening, such as the increased intensity noise in the amplification stage which can degrade the coherence of the optical spectrum when passing through the HNLF and four-wave-mixing (FWM) between the 12.5 GHz spaced modes and the suppressed 250 MHz spaced modes [85]. For what concerns the power losses, they recorded an intracavity loss of a factor 4 for each cavity.

The Walsworth group at Harvard-Smithsonian Center for Astrophysics in Cambridge (USA) is working on astro-comb as well [91, 92, 93], to use it in the next future as the calibration source for the TRES (Tillinghast Reflector Echelle Spectrograph) optical echelle spectrograph at the Smithsonian Astrophysical Observatory on Mt. Hopkins in Arizona. They used a 1 GHz repetition rate Ti:Sa femtosecond laser as the comb source and generated a 100 nm wide spectrum around 850 nm with 25 GHz mode spacing, filtering the comb with a single F-P cavity. The cavity is stabilized by an injected diode laser signal that is itself stabilized to the Rb D1 line (at 794.7 nm) using a dichroic-atomic-vapour laser lock (DAVLL [94]). With this system they obtained a final side mode suppression of -25 dB. They also addressed to the problem of broadening an astro-comb in a photonic crystal fiber [95]. They pointed out that numerical modeling shows that cascaded FWM dramatically degrades the input comb's side mode suppression and causes side mode amplitude asymmetry. These two detrimental effects can systematically shift the center-of-gravity of astro-comb spectral lines leading to wavelength calibration inaccuracy and instability. They concluded that this performance penalty has to be compensated by a stronger-than-required side mode suppression before the spectral broadening. They started with a 1 GHz Yb-fiber laser operating at 1.06 μm and they filtered it with a 16 GHz F-P cavity configured for double-pass ($m = 16$) with finesse $F = 200$. They obtained a 30 nm wide spectrum of 16 GHz spaced modes with a side mode suppression of -56 dB. This spectrum is then broadened in a 2

cm SF6-glass photonic crystal fiber. As expected, the highly non-linear process is accompanied by the rapid growth of side modes. The dominant effects are self-phase modulation (SPM) and dispersion. SPM, a special type of degenerate FWM modulation, causes spectral broadening by redistributing the total power among frequency components. In particular, for initially weak side modes, nearby strong astro-comb lines act as pumps that provide gain through FWM. Moreover, optical amplification is a phase-sensitive non-linear process, i.e. the phase relations of spectral lines determine the power flow among them. Although the first side mode on either side of an astro-comb line experience identical suppression from the F-P cavity, these side modes receive opposite phase shifts relative to the astro-comb line sitting between them and this phase asymmetry induces differences in growth of side mode power. After the spectral broadening, they observed that the suppression difference between the upper and the lower first side mode is as large as 20 dB and that the upper side mode becomes even stronger than its nearest astro-comb line at some wavelength. This effect results in a strong asymmetry of the calibration lines, which is completely detrimental to reach a better than 1 m/s calibration.

Chapter 4

The experimental apparatus: requirements and optical layout

As I focussed in the previous Chapter, the filtering F-P cavities are the crucial point of the experimental apparatus. In this Chapter, I will describe the main problems to deal with and the solutions I took to optimize the cavities layout.

There are two main issues to be considered during the apparatus design: first of all which are the mirror coating properties we need for an adequate side mode suppression and to avoid coincidences between transversal cavity modes and unwanted comb modes. Secondly, which are the physical constraints to reach an optimized apparatus, i.e. the minimum power needed after the filtering process and the laser beam dimensions at the cavity mirrors.

4.1 Mirror requirements

As described in Section 3.3.1, the goal of achieving a -32 dB side mode suppression cannot be reached using a single F-P cavity, since in this case the required mirror reflectivity (i.e. finesse) would be so high that it could be obtained just for a very narrow wavelength range, because of comb-cavity mismatches caused by coating dispersion (see Section 3.4). As already shown, the required side mode suppression (-32 dB) can be obtained with two F-P cavities in series of $F = 500$ each one (reflectivity $R = 99.4\%$), or alternatively with 3 cavities in series with

$F = 250$ ($R = 98.7\%$). In addition, GDD (Equation 3.19) must be taken into account to achieve the maximum possible filtering spectral converage.

It is interesting to consider the possibility of filtering the comb spectrum with F-P cavities of different FSRs in series. The only condition to be imposed is that the FSR of the second cavity must be an integer multiple of that of the first cavity, hence the first cavity would have $\mathrm{FSR}_1 = m_1 f_r$ and the second cavity $\mathrm{FSR}_2 = m_2\ \mathrm{FSR}_1$, with $m_2 = n m_1$ (n integer). In this case, the behaviour of suppression for the unwanted modes changes with respect to the case of two identical cavities in series, so that choosing a convenient value for FSR_1 can give advantages in relaxing the mirror reflectivity requirements. Suppose to have $\mathrm{FSR}_1 = 1.6$ GHz and $\mathrm{FSR}_2 = 16$ GHz: to produce a comb spectrum made of modes spaced 1.6 GHz with the 100 MHz adjacent modes suppressed by a factor -32 dB, it is sufficient a cavity finesse of 322. When the unwanted modes are filtered out with the second cavity (FSR = 16 GHz), in this configuration the most significant unwanted modes are no more the 100 MHz adjacent ones (which are already filtered by the first cavity up to -32 dB), but instead the 1.6 GHz adjacent modes, because these last modes are those which are transmitted by the first cavity. A finesse of 322, hence, still ensures that the 1.6 GHz adjacent modes are suppressed up to -32 dB, while the 100 MHz adjacent modes are suppressed to -44 dB with the same finesse. In addition, the advantage of using this second approach in terms of required initial comb power will be clear in Section 4.2.1.

4.1.1 Dielectric coated mirrors

In the case of 2 F-P cavities in series, the only possibility to reach such reflectivities in a broad spectral range is to use dielectric coated mirrors (for the choice of the mirrors properties I refer to the case of two cavities in series with the same FSR). Asking some optics suppliers for the lowest achievable GDD mantaining an almost constant reflectivity of 99.4% in the whole spectral range $1-2$ μm, the best proposed solution was a GDD varying between -5000 and 5000 fs^2. From Equation 3.19, I computed that such a variation corresponds to a shift in FSR of more than 200 MHz between the center (1.5 μm, where GDD is null) and the side bands (1 and 2 μm) of the spectral range, so that at the edges possible filtered mode hopes with respect to the original comb

mode to be transmitted can occur. I can overcome this difficulty with two possible solutions. First, the comb can be filtered with two cavities in a limited spectral region around 1.5 μm, in which the high reflectivity and low GDD requirements are fulfilled. The spectrum can, then, be broadened to a large spectral coverage by using the well established highly non-linear fiber (HNLF) technology used to get self-referenced near-IR fiber combs. A second possibility would be, instead, to split the comb spectrum in several parts and filter with adequate cavities each portion of the spectrum. The second solution, while simpler from a conceptual point of view, results complex to develop for practical purposes. In fact, I evaluated that to cover the whole $1-2$ μm region the spectrum must be splitted at least in five portions, which means ten cavities to be well and independently aligned and electronically controlled, hence producing a complex set-up. Therefore, I chose to follow the first option and looked for 99.4% constant reflectivity mirrors in a reduced spectral range around 1.5 μm.

The best mirrors I found are custom made by Layertec GmbH[1] and their nominal reflectivity and GDD behaviour with wavelength are shown in Figure 4.1. The mirror substrate (diameter 12.7 mm) is made of Infrasil, a type of fused silica glass almost transparent in the near-IR. The high-reflection coating is deposited on the front side of the substrate, while on the rear side an anti reflection (AR) coating ($<0.25\%$) is guaranteed over the range $1500-1650$ nm. The high-

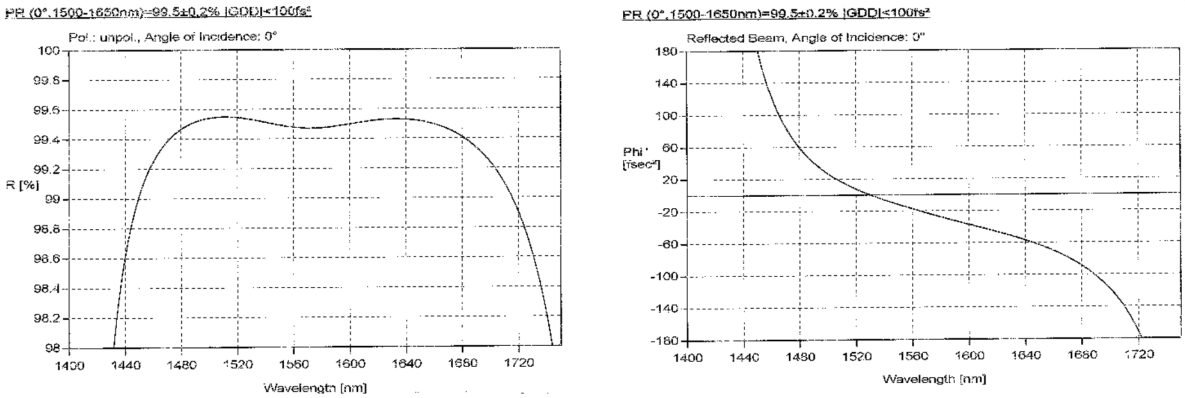

Figure 4.1: Nominal specifications for reflectivity R at normal incidence and GDD as provided by Layertec GmbH.

[1] http://www.layertec.de/en/home/index.

reflection coating, instead, provides a nearly constant reflectivity of $R = (99.5 \pm 0.2)\%$ over the same spectral range at normal incidence (angle of incidence 0°). The choice of the 1500−1650 nm interval has been dictated by the fact that the master mode-locked fiber laser of our FC1500 comb operates in such spectral region. For what concerns the GDD, it stays always below 100 fs^2 in the range 1500−1650 nm, which corresponds to a maximum shift in FSR of 5 MHz between the central wavelength and the edges, a reasonable value for our application.

As discussed in Section 3.3.2, the choice of the mirror radius of curvature is crucial as well to achieve a -32 dB suppression, because a suitable choice guarantees that higher order transversal modes are not transmitted during the filtering process. In Figure 3.6 I showed that a good choice would be to build hemifocal cavities with one plane-plane mirror and one plane-concave mirror with a radius of curvature $r = 100$ mm. For this reason, half of the substrates has plane-plane surfaces and half has plane-concave ($r = 100$ mm) surfaces. Moreover, the thickness of the plane-plane mirrors needs to be as smaller as possible: as we will see, it will be necessary to actively control the cavity length to staedily mantain the overlap between cavity peaks and wanted comb modes, so that a piezoceramic element will be mounted on the plane-plane mirror to provide fine adjustments of the cavity length. Thicker mirrors, hence, guarantee a faster response of the cavity to the locking system.

The nominal characteristics of the dielectric coated mirrors used to build the filtering cavities are reported in Table 4.1.

Properties	Provided Values
Reflectivity (nominal)	$(99.5 \pm 0.2)\%$
Transmission (nominal)	0.5%
Diameter (pl-pl)	(12.7 ± 0.1) mm
Diameter (pl-conc)	(12.7 ± 0.1) mm
Thickness (pl-pl)	(2.31 ± 0.1) mm
Thickness (pl-conc)	(6.35 ± 0.1) mm
Radius of curvature	100 mm
Anti Reflection coating (0°)	$< 0.25\%$

Table 4.1: Nominal characteristics of dielectric coated mirrors as provided by Layertec GmbH.

4.2 Physical constraints

In this Section I will approach two different issues. The first concerns the required power in the filtering process. An estimate of the available power is, in fact, crucial to obtain an octave spanning spectrum.

The second issue, instead, concerns the spatial coupling of the laser beam into the cavity. This is a common problem when continuous or pulsed laser light is coupled into a F-P cavity. The maximum coupling is obtained when the Gaussian spatial mode of the input light matches the fundamental mode supported by the cavity.

4.2.1 Required power

To evaluate the required power after the filtering process, a first calculation to be done is which is the minimum power that one resolution element of the spectrograph can detect. In fact, it is necessary that the output power per comb line is higher than the minimum power detectable by the spectrometer. A rough estimate, considering the case of Giano, can be obtained assuming first of all, in the worst case, an overall optical efficiency, given by the ratio of the number of electrons generated by the array over the number of incident photons, $\eta = n_e/n_\gamma \sim 10\%$ [36]. Assuming that a reasonably fast and accurate calibration would require $10^3 - 10^4$ electrons per second per resolution element, a single comb line before the spectrometer must hold at least $10^4 - 10^5$ photons per second, which correspond to $2 \times 10^{-15} - 2 \times 10^{-14}$ W of power. If we had a comb mode every 16 GHz, we have roughly 9×10^5 modes between 1 and 2 μm, so that the minimum total mean power before the spectrograph (assuming that the modes have all the same intensity) needs to be $\sim 2 - 20$ nW. In the case, instead, of a comb mode every 16 GHz in the range 1.5−1.65 μm, there would be roughly 1140 modes, so the minimum total mean power would be $\sim 2 - 20$ pW.

To filter the FC1500 comb in the region 1500−1650 nm, I used its secondary fiber coupled output port in this limited range, with a total mean power of approximately 30 mW (see Section 2.4.1). Assuming a loss factor of 160 in power due to the fact that, at the end, we have filtered just one comb mode every 160 and considering at least a loss factor of 2 for each cavity due to

mirror absorption and other cavity losses, we would get only 45 μW of mean power after the filtering if we start with 30 mW (corresponding to a total loss factor of 640). While this value is enough to use the filtered comb as the calibration source for Giano in the reduced 1500−1650 nm spectral region, the experimental development is difficult to carry out in this case. In fact, after the first cavity filtering, only a mean power of 90 μW is available (loss factor of 160×2), which is not enough to actively control in an easy way the second cavity. Such a technical problem could be partially mitigated by using two cavities with different FSRs. After filtering with a first 1.6 GHz cavity, a loss factor of 32 (16×2) in power must be considered, i.e. a mean power of about 0.9 mW for a 30 mW input power is available for the second 16 GHz cavity. This cavity gives an additional power decrease factor of 20 (10×2), producing as a result the same final power as in the case of two identical cavities.

On the other hand, such a final mean power of the filtered comb is absolutely not enough for the comb broadening to the 1−2 μm region by using the HNLF technology. Such non-linear process needs tens mW of power to be coupled into the fiber for an efficient broadening (i.e. which covers an optical octave). As a consequence, some laser amplification processes must be used to bring up the gap of more than two orders of magnitude between the needed power for broadening and the estimated power after filtering a 30 mW comb. Near-IR fiber laser technology provides again the solution, thanks to the Er-doped fiber amplifier (EDFA). In particular, the device EDFA P250-Custom, provided by MenloSystems GmbH, uses a silica fiber doped with Er ions as the gain medium to amplify the 30 mW comb input signal up to 450 mW of mean power in the 1500−1650 nm range. Higher amplification is difficult to achieve due to the high peak-power of the short input pulses. An EDFA before the filtering cavities gives mean power values of about 14 mW and 0.7 mW after the 1.6 GHz and 16 GHz cavities, respectively. This is still not enough for HNLF broadening, and at least two more amplifiers are necessary, one between the two cavities and the other after the second cavity, to achieve such a comb spanning. The elevate cost of the final set-up[2] on one hand, and the complexity of the final arrangement (with several air-fiber couplings, see [85]) on the other hand make this solution difficult to develop in a practical astro-comb application. Nevertheless, I used an EDFA before the first filtering cavity

[2]Each EDFA costs about 20000 euro.

to get the power requirements in the 1500−1650 nm spectral range more relaxed, helping the experimental control of the filtering process. In addition, this configuration allowed me to test the experimental conditions for a further broadening by using dielectric mirror cavities and other EDFAs. Figure 4.2 shows the scheme of the system layout.

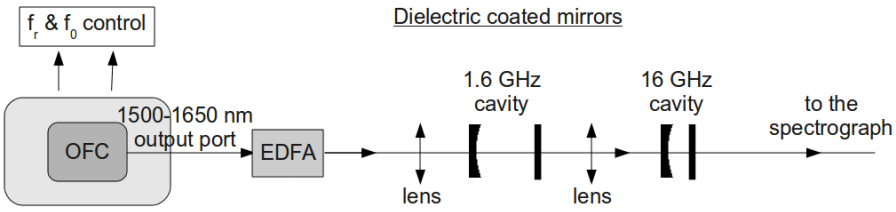

Figure 4.2: Scheme of the system layout in the case of dielectric coated mirrors.

The conclusions that can be draft considering just this limited range, especially regarding the side mode suppression and the cavity losses, should not differ with respect to the case of an octave spanning spectrum, so that their analysis should be comprehensive of the main problematics encountered in developing this type of system.

4.2.2 Spatial coupling requirements

The geometrical configuration choosen for the filtering cavities (i.e. hemifocal configuration) imposes the spatial parameters of the fundamental Gaussian mode of the standing-wave inside the cavity. They can be calculated using the *paraxial wave approximation* as described in Appendix B.

In the case of this Thesis, for a cavity of length L, imposed by FSR, I have a first plane mirror and a second curved mirror, with an assigned radius of curvature $r = 100$ mm, so that the ideal beam behaviour consists in a plane wave front on the first mirror, i.e. a waist, and a wave front with a radius of curvature of 100 mm on the second mirror, i.e. after a distance $z = L$. Using Equations B.11 (reproduced here for clarity):

$$w^2(z) = w_0^2 \left[1 + \left(\frac{z}{z_R}\right)^2\right], \qquad r(z) = z\left[1 + \left(\frac{z_R}{z}\right)^2\right],$$

the beam waist can be computed as a function of r and $z = L$:

$$w_0 = \left[(r - L) \, \frac{\lambda^2}{\pi^2} \, L \right]^{1/4} . \tag{4.1}$$

Considering a wavelength $\lambda = 1575$ nm (at the center of the range 1500−1650 nm), in the case of FSR = 1.6 GHz ($L = 93.7$ mm) a waist $w_0 = 0.110$ mm is needed on the cavity plane mirror, while for FSR = 16 GHz ($L = 9.37$ mm) it is necessary a waist $w_{02} = 0.121$ mm.

Computation of the best lens: the first cavity

As already noticed at the beginning of Section 4.2, the input laser beam at each cavity must fulfil the requirements computed from Gaussian optics, in order to maximize the coupling efficiency. I start with a collimated beam at the output of the EDFA, which has a waist w_0^f at the fiber collimator position. Such a beam must be focused at the z-axis position where the plane mirror will be placed, with the above calculated w_0 waist value for each cavity. In fact, a converging lens is able to change the $r(z)$ and $w(z)$ parameters of the input beam, as described in Appendix B.1. By considering the above calculated value $w_0 = 0.110$ mm for the first cavity and by measuring the output-collimator waist w_0^f, I calculated the needed amplification factor α (see Appendix B.1). The focal length of the lens can, hence, be computed as a function of Z_0 by using Equation B.21, which is:

$$\alpha^2 = \frac{f^2}{Z_0^2 + z_{R1}^2} .$$

To measure the waist w_0^f immediately after the fiber collimator, I used the "knife edge technique": a knife edge is fixed on a calibrated translation stage and is positioned on the top of the beam; a power meter is placed immediately after. Translating the knife edge through the beam, the power at each knife edge position can be read on the power meter as the knife edge increasingly "cuts" the beam until the beam is completely blocked and the measured power is zero. At each position, the power meter records the integral of the Gaussian beam between $-\infty$ and the knife. Hence, the behaviour of the measured power as a function of the position of the

knife with respect to the beam is fitted by the following expression [77]:

$$P = P_0 + A \,\mathrm{erf}\left(1.414\,\frac{y - y_0}{w}\right) , \tag{4.2}$$

where P is the measured power at each knife edge position (along the y-axis), P_0 is the maximum power (i.e. the beam power without the knife), A is a constant, y_0 is the knife position which corresponds to a half of the maximum power and w is the spot size as defined from Equation B.7. The function erf() is the "error function", which is a sigmoid-shaped function described by the expression:

$$\mathrm{erf}(z) = \frac{2}{\sqrt{\pi}} \int_0^z e^{-t^2} dt \,. \tag{4.3}$$

Figure 4.3 shows the behaviour of the measured power as a function of knife position (black squares). A fit with Equation 4.2 is also shown (red curve). The table on the left displays the values of the fitted parameters (P_0, y_0, A, w). The fitted value for the spot size of the beam exiting from the collimator results $w = (0.43 \pm 0.02)$ mm. The beam size has been measured only by cutting the beam along the y-direction due to the fact that the circular geometry of

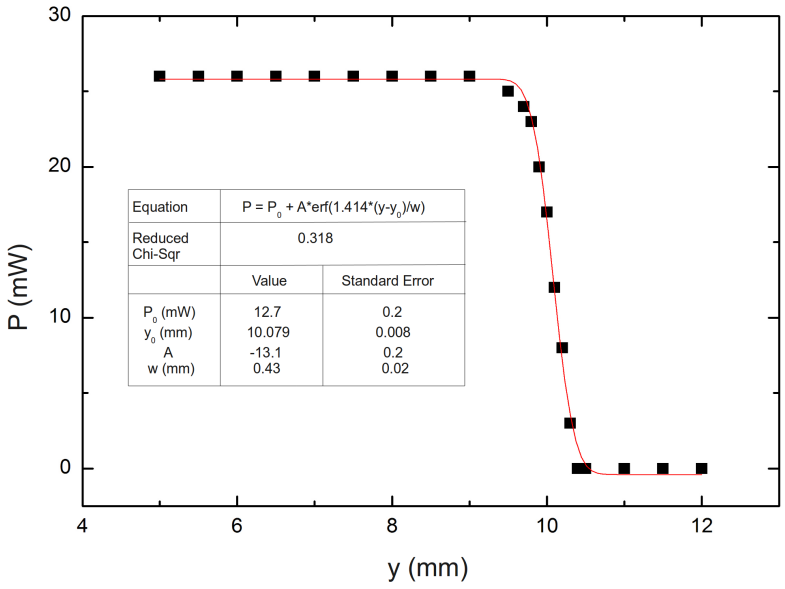

Figure 4.3: Measured power as a function of the knife position (black squares) and the fit with Equation 4.2 (red curve). The table shows the values of the fitted parameters.

the fiber guarantees a circular non-astigmatic shape of the output beam (i.e. a TEM_{00} mode). Measuring in the same way the spot size at different distances from the collimator, I checked that it is well diffraction-limited collimated, with a Rayleigh distance of 40 cm where the spot size stays constant at the above indicated value.

Hence, the value of α for the first cavity results $\alpha = w_0/w_0^f \sim 1/4$,

and I can now calculate the focal length f of the lens as a function of Z_0. Some practical constraints must be considered for both the Z_0 and f parameters.

One can think that the simplest practical configuration would be the so called "f-f configuration", which is the case of $Z_0 = Z_i = 0$. Given w_0^f and w_0, this would imply a focal length of about 100 mm, so that the collimator-to-lens distance would be of 10 cm. However, on one side the physical space between the EDFA output and the cavity taken up by the optical components necessary for optical isolation (feedback from the cavity to the comb must be avoided to mantain frequency stability of the comb) and for optical alignment, and on the other side the necessity to compact all the system in a 60×45 cm breadboard, impose a collimator-to-lens distance of about 30 cm. Hence, the non-zero resulting value for Z_0 implies a non-zero value for Z_i, i.e. the waist w_0 will not be localized at a focal length distance from the lens.

For what concerns f, a compromise needs to be found, because only certain discrete values of focal lengths are usually commercially available. With all these considerations in mind, the best solution I found to satisfy both the requirements is to use a lens of $f = 125$ mm positioned at a distance of 28 cm from the fiber collimator ($Z_0 = 15.5$ cm): the lens waist can be found at a distance of 13.5 cm from the lens ($Z_i = 1.0$ cm). Since I have observed that the lens position is critical for the cavity alignment and for a good spatial coupling, I decided to mount the lens on a "x-y-z translator", so that a fine adjustment can be done in all directions.

Computation of the best lens: the second cavity

After the beam has passed the first cavity plane mirror, it starts to diverge and reaches a size of $w_R = 0.44$ mm (computed from the first of Equations B.11) on the first cavity concave mirror, while the wave front has a radius of curvature of 100 mm. The same considerations made for

the first F-P cavity needs to be done for the second cavity as well, so it is convenient to have a collimated beam again after the first cavity.

The simplest solution would be to put another $f = 125$ lens[3] at a distance of 13.5 cm from the waist position, in such a way to have again an output collimated beam as the starting one. Unfortunately, the size of the supports of the cavity mirrors (one must be mounted on a z-translation stage for a coarse control of the cavity length) and the dimensions of the metallic box used to cover each cavity and hence to increase its passive stability (as will be discussed in Section 5.1), give a minimum accessible distance of 15 cm from the first cavity waist. Moreover, the plane-concave mirror has a finite thickness of 6.35 mm, so that its presence modifies the beam propagation. The effect produced by crossing through the mirror can be interpreted as if the beam would cross through a lens with an equivalent focal length, whose inverse is given by the Lensmaker's formula (introducing also the refraction index of the material of the mirror):

$$\frac{1}{f} = (n-1)\left(\frac{1}{r_1} - \frac{1}{r_2}\right), \tag{4.4}$$

where n is the refraction index of fused silica ($n = 1.44$ at 1.5 μm) and r_1 and r_2 are the radii of curvature of the entrance and exit faces, respectively ($r_2 = +\infty$). The concave mirror, thus, acts as a diverging lens.

Considering its contribution, a collimated beam can be obtained by placing a $f = 175$ lens at a distance of 21.5 cm from the waist. I measured the spot size and verifyied that it is collimated; the resulting waist is $w_0^i = (1.07 \pm 0.01)$ mm. The beam dimension is more than two times its initial size, so I introduced two lenses of focal length 100 and 50, respectively, to build a telescope of factor 2, so that the beam size is reduced to half its initial value. After this 3-lenses system, we have a collimated beam of waist $w_{02}^i = 0.53$ mm. In the case of the second cavity ($L = 9.37$ mm instead of $L = 93.7$ mm), the required waist at the cavity plane mirror results $w_{02} = 0.121$ mm. Going on again as for the first cavity, I found that the best solution is to introduce a $f = 125$ lens at a distance of 20 cm from the $f = 50$ lens; the desired waist is generated at a distance of

[3]The conventional notation is to point out the focal length value in mm, without specifying the unit of measurement.

12.9 cm from the lens.

Definitive optical set-up of the filtering cavities

A scheme of the definitive optical layout is depicted in Figure 4.4. The light path is shown by the red dotted line. As can be seen, it is necessary to introduce an optical isolator also between the two cavities to avoid frequency instabilities of the first cavity due to feedback from the second one. After each cavity, a beam splitter (BS) mirror peaks up a fraction of the filtered light and sends it to a photodetector (PD); such light is used for the cavity length control (as will be explained in Section 5.1.3).

After the second cavity, a lens of $f = 175$ placed at 21.5 cm from the cavity waist collimates again the filtered light to be sent to Giano. I used this light to analyze the filtering performances as described in the next Chapter.

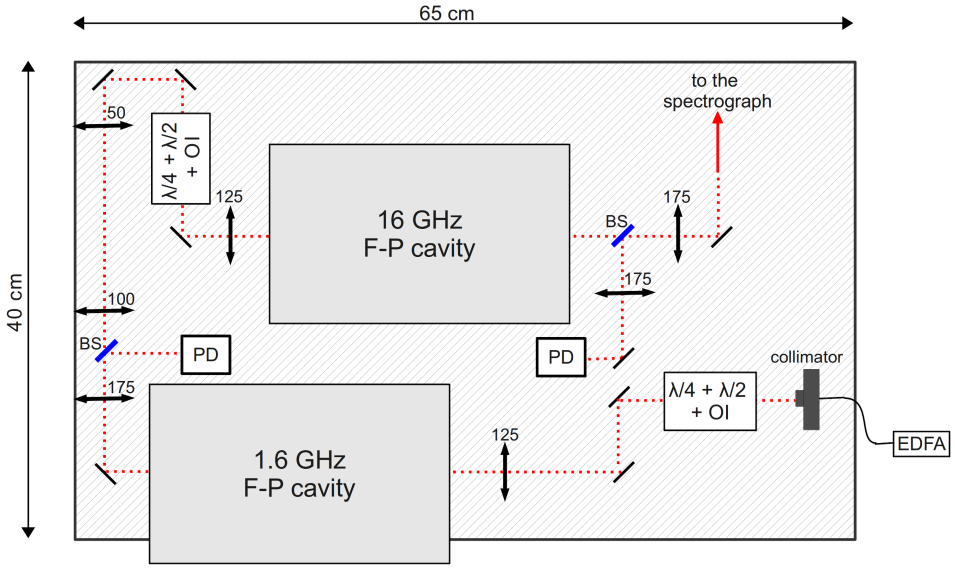

Figure 4.4: Scheme of the optical system layout. The dotted red line represents the beam path. The beam splitter (BS) mirrors pick up a fraction of the filtered light after each cavity and send it to a photodetector (PD) for the locking control system.

Chapter 5

Experimental results with dielectric coated mirrors

In this Chapter I will describe the experimental results obtained using two F-P cavities in series, with free spectral range 1.6 GHz and 16 GHz respectively, in the limited spectral range between 1500 and 1650 nm. The cavities are both made of dielectric coated mirrors (nominal reflectivity: $R = (99.5 \pm 0.2)\%$), the first plane-plane and the second plane-concave with a radius of curvature of 100 mm.

First of all, I will describe which is the final system layout. Then, I will present the experimental results, with special attention on the side mode suppression and spectral coverage for each cavity by itself and for the two cavities in series.

5.1 The final system layout

In the previous Chapter, I described the optical set-up for coupling the comb light into the cavities. Here, I complete the description by giving the details on how the cavities are built and how they work for the astro-comb application. The crucial point for a good operation of each cavity as a comb filter is to achieve a cavity length L which ensures both the conditions: 1) FSR $= c/2L$, for the wanted FSR; 2) FSR $= mf_r$, i.e. FSR being an integer multiple of the repetition rate ($f_r = 100$ MHz). These two conditions impose a well defined cavity length, which

must be achieved with an absolute accuracy determined by the comb wavelength (i.e. at the micron level). Moreover, this length must be mantained constant over long time periods, at least of the order of the integration time used to calibrate the spectrograph. In this respect, cavities with high passive length (i.e. frequency) stability should be designed. In addition, active control of such cavity length will give the final cavity stability required for this application.

5.1.1 Cavities set-up

Since the compactness and the stability over long time are pressing conditions, my first approach has been to use rigid cavities made of super invar[1]: the mirrors are fixed inside the super invar structure in such a way that the plane mirror is at the wanted distance from the curved one. The plane mirror is glued on a piezoceramic element (PZT[2]), used to actively control the plane mirror position (i.e. the cavity length) within 16 μm (corresponding to the maximum voltage held by the PZT element, 150 V). Pictures of the super invar structure and of the mirror PZT and support are shown in Figure 5.1.

The experimental set-up of such rigid cavities has revealed two main problems. First of all,

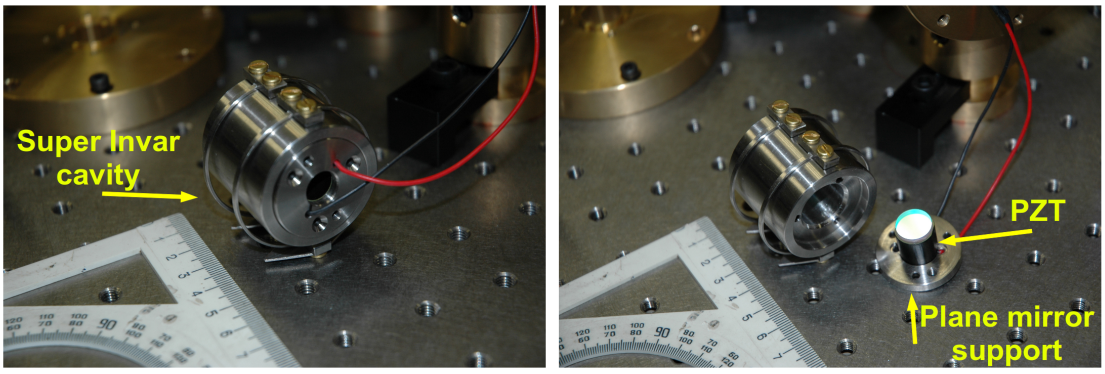

Figure 5.1: Pictures of the super invar rigid cavity at 1.6 GHz: the detail of the plane mirror mounted on a PZT, which is in turn fixed on a rigid support, is also shown.

[1]Super invar is an alloy of Ni, Co and Fe wich has a near zero coefficient of thermal expansion at room temperature.

[2]I choose PZTs which ensure a maximum expansion of 16 μm with a 150 V voltage. From the relation $\Delta L/L = \Delta\text{FSR}/\text{FSR}$, we obtain a maximum FSR shift of 0.3 MHz for the first cavity and 27 MHz for the second one.

the short range over which the cavity length can be changed (16 μm) was not enough to get the comb-cavity mode matching condition: $c/2L = 160 f_r$. In fact, comb transmission from such a cavity was not observed, even by slightly changing the value of f_r, so that a larger mechanical variation of the mirrors distance is needed. Secondly, parallelism between mirrors must be good enough to excite only the fundamental longitudinal mode of the cavity. I verified that this was not the case of our invar cavity, where multiple transmitted peaks were observed when the cavity was illuminated with a continuous wave (cw) laser (as expected for localized interference in a non-parallel F-P cavity). As a consequence, high precision mechanical development of such invar cavity must be realized in order to be able to tilt one mirror with respect to the other. As a conclusion, this approach, even if potentially suitable for what concerns long term passive stability of the cavity, needs large mechanical improvements in terms of wide tunability of the cavity and parallelism of the mirrors.

To relax the above mechanical limitations, I developed a different cavity design, in which mirrors are supported by tilting knob holders, independently. A picture of the 16 GHz cavity is shown in Figure 5.2: the mirrors mounted on the two-knob tilters can be recognized. Since the mirrors distance is a very critical parameter as explained above, it is not sufficient to manually place the mirrors at the wanted distance. The solution was to mount the curved mirror support on a micrometric translation stage with 1 cm travel, as shown in Figure 5.2. The cavity length resonant with the required harmonic comb frequency ($16 f_r$ or $160 f_r$) is achieved following this procedure: after the two mirrors are placed roughly at the right distance and are aligned (see next Subsection for details), the curved mirror can be translated along the beam axis by using a micrometric screw up to the exact distance at which the comb is resonant within the cavity. As in the invar design, final fine adjustments and control of the cavity length are achieved with the PZT element glued on the plane-plane mirror rear surface (see Figure 5.2).

In addition to the fact that, due to not compensated thermical fluctuations, this approach makes cavities more sensitive to long term drifts with respect to the case of invar cavities, free-air medium between mirrors is not free from refraction index fluctuations due to air displacements. Moreover, such cavities are very sensitive to acoustic noise. To avoid or minimize these effects,

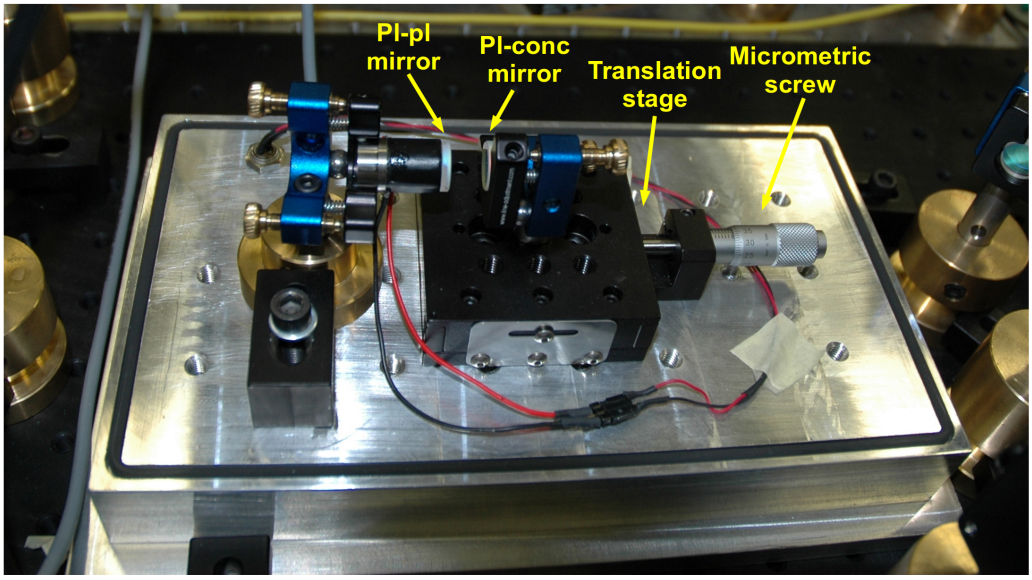

Figure 5.2: Picture of the second F-P cavity: mirror mounts and translation stage with micrometric screw can be recognized.

I placed the cavities inside boxes made of anticorodal[3]. A 3D model of these boxes is shown in Figure 5.3. Each box is composed by two parts: a basement and a cover. The basement, which can be fixed on the optical breadboard, is filled by 3 cm spaced threaded holes to fix the mirror supports, as shown in Figure 5.2. When the alignment is optimal, the cover is put upon the basement to almost close the cavity. Two holes with a diameter of 2 cm are made on the entrance and exit face of the cover in correspondence of the cavity optical axis to let the beam enter and exit the box; two fused silica windows (which are transparent to near-IR radiation) are glued on the holes to close the box. The windows are coated with an antireflection coating, made by L.A.V. coatings[4], which ensures a back reflection always below 0.5% in the whole spectral range $1-2$ μm. With such antireflection coating, putting the windows in their final position with respect to the cavities, spurious interferences between windows and back surface of the mirrors (or other optics) were not observed. I designed the boxes to assure the possibility of making vacuum inside. To this aim, I prearranged a threaded hole on the top of the cover to insert a

[3]Anticorodal is an alloy of Al with Mg, Cu and Mn.
[4]http://www.lavcoatings.it/.

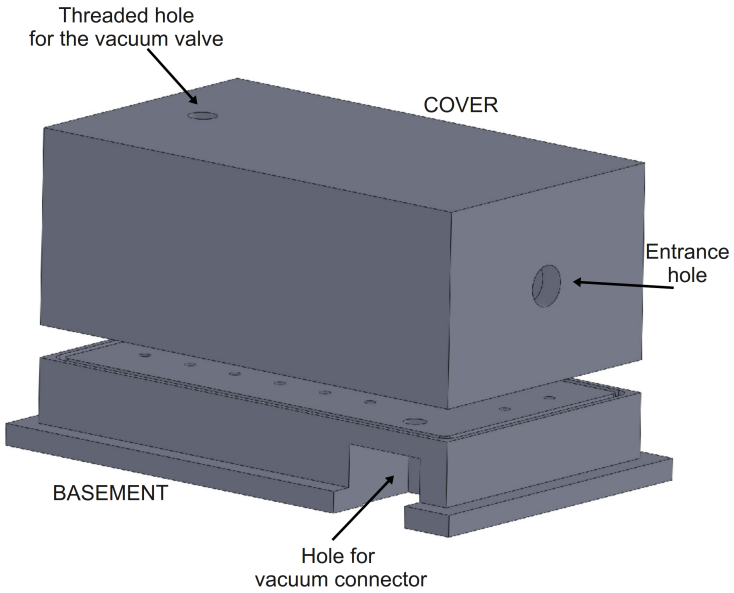

Figure 5.3: 3D model of the box that contains each cavity.

valve to realize the vacuum and a hole around the surface of the basement where the cover is placed, which contains an o-ring made of Viton[5]. Another hole in the back of the basement is used to place the appropriate vacuum connector for the PZT.

5.1.2 Cavity alignment

Once the cavity mirrors are placed as described above, the cavities need to be aligned. The first step is to roughly center the mirrors with the beam path by moving coarsely the mirror supports on the box basement. To help this procedure, the beam path was previously well defined in terms of mantaining over a long propagation path the same height and the same transversal position with respect to the optical table. This was done by using coupling mirrors in front of the cavity as shown in Figure 5.4, which is a detailed view of the system layout for the 1.6 GHz cavity, already schematically shown in Figure 4.4.

The second step is to make the high reflectivity surface of each mirror perpendicular to the beam axis. I removed temporarly the input mirror (the plane-plane one) and, thanks to a near-

[5]Viton is a brand of synthetic rubber and fluoropolymer elastomer.

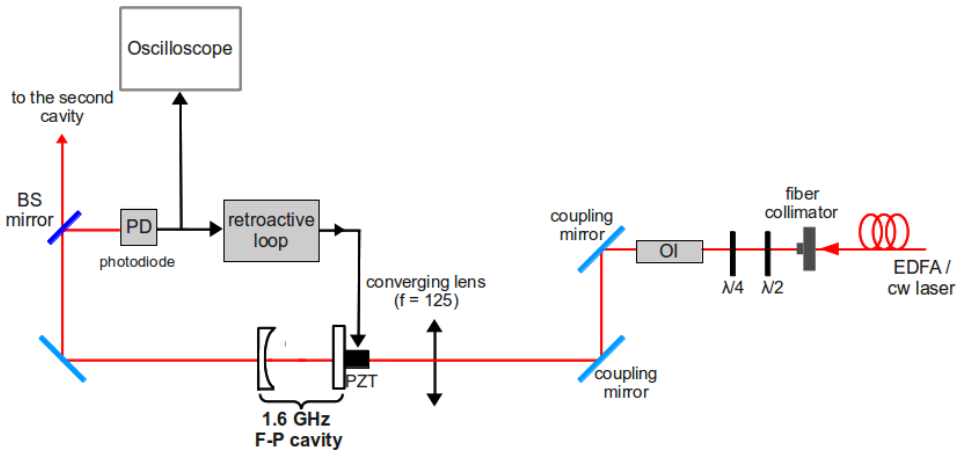

Figure 5.4: Detailed view of the system layout for the 1.6 GHz cavity.

IR viewing card, I superimposed the reflected beam with the incident one by using the tilting knobs of the mirror mount. Then, I reintroduced the input mirror and the reflected beam from this mirror was similarly superimposed with the input beam.

The third step requires fine alignment of the mirrors to achieve the parallelism between them. This must be done by observing the cavity transmitted spectrum on an oscilloscope. As shown in Figure 5.4, I put a beam splitter (BS) mirror after each cavity to collect a small fraction of the transmitted light (less than 0.5%) and to focus it onto a photodetector (InGaAs detector model DET10C by Thorlabs GmbH) connected with the oscilloscope. A sawtooth ramp is applied to the PZT to scan the cavity FSR while transmission spectrum is recorded. Prealignment is easier to achieve with a cw laser than with a pulsed one as a comb[6]. To this aim, I used a cw laser at 1554 nm (model DL100 DFB by TOptica[7]). This is a single mode diode laser with a FC/APC connectorized fiber pigtail as the output. The output fiber can be connected into a fiber collimator, replacing temporarily the EDFA output; in this way, the cw laser light follows the same optical path of the comb light.

[6]The light from any laser is resonant with a F-P cavity when the optical path length ($2nL\cos\theta$) difference between two subsequent reflections on the cavity mirrors is an integer multiple of the laser wavelength. Since the optical path length depends on the cavity length L, for a cw laser at, for example, 1550 nm, the wavelength is so small with respect to L that in practice, when the cavity is aligned, we can see transmission from the cavity at each mirror distance around L.

[7]http://www.toptica.com/.

Fine cavity alignment is achieved by moving the cavity mirrors mount knobs and the two coupling mirrors in front of each cavity (see Figure 5.4), whereas the transmission spectrum of the cw laser observed on the oscilloscope is optimized. I iterated the procedure until the transmitted power is contained as much as possible in the fundamental longitudinal cavity mode. At this stage, the focusing position of the coupling lens is also fine controlled in order to avoid excitation of unwanted transversal cavity modes. An example of the signal visualized on the oscilloscope for the 16 GHz cavity when it is aligned is shown in Figure 5.5: the two peaks define one FSR, in this case FSR = 16 GHz. The x-scale in this Figure refers to the duration of the sawtooth ramp applied to the PZT. Some transverse modes can be glimpsed between the two major peaks, but I verified that their amplitude stays always below a factor 32 dB with respect to the main peaks. A rough estimate of the cavity finesse can be computed as the ratio between the FSR value (measured as the distance between the two main peaks) and the FWHM linewidth of a single transmission peak. In this way I obtained a finesse value around 500, which corresponds to a reflectivity of 99.4%, consistent with the nominal value of the mirror coating. Such a value

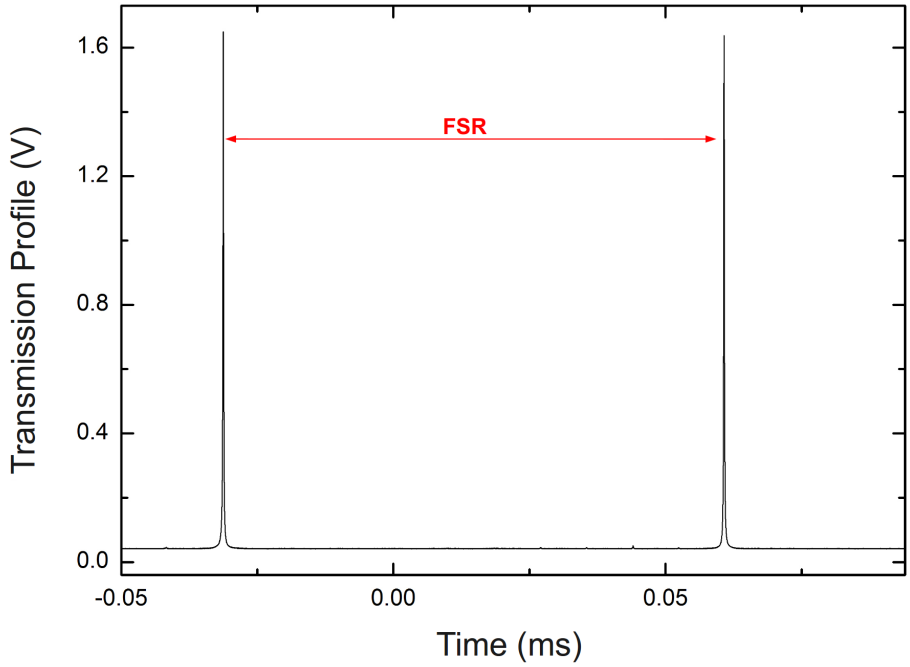

Figure 5.5: Image of one FSR for a well-aligned 16 GHz cavity as visualized on the oscilloscope.

is also an indication of the good cavity alignment.

Afterwards, I put again the EDFA output fiber into the fiber collimator and looked for the comb signal. At this point, usually no signal is visible on the oscilloscope. Rotating the micrometric screw of the translation stage of the curved mirror, I found a unique position at which a signal like the one shown in Figure 5.6 is visible on the oscilloscope: the comb is now resonant with the cavity. This signal is obtained in the same way as for Figure 5.5, i.e. scanning the cavity length, and the displayed envelope is repeated every FSR.

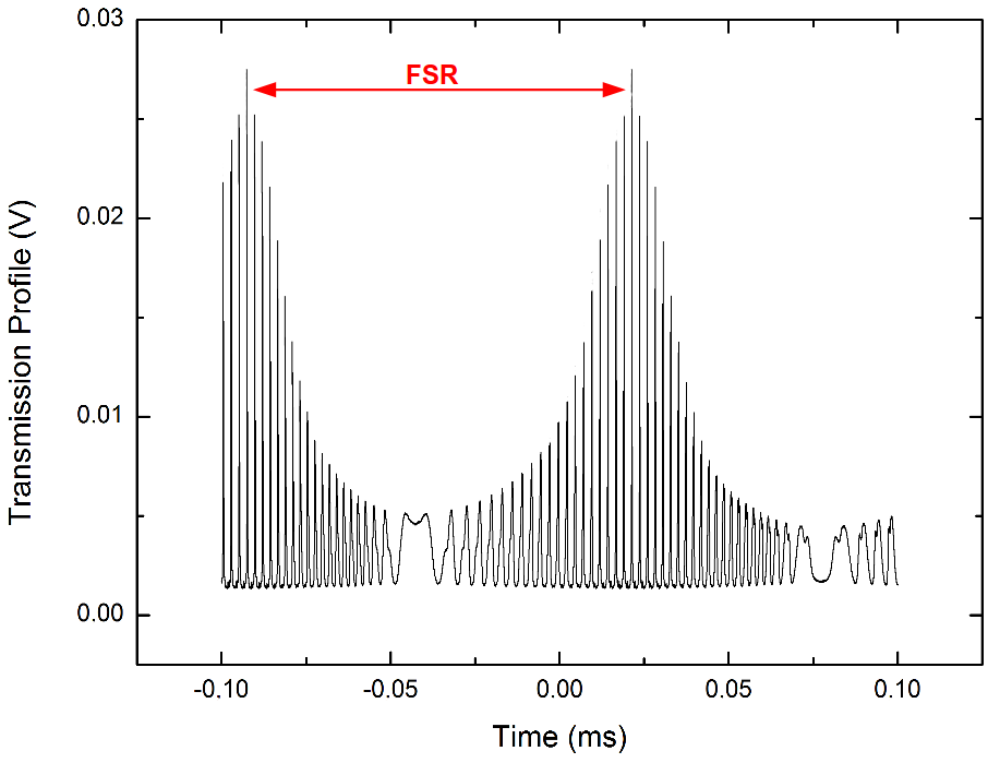

Figure 5.6: The filtered comb after the 1.6 GHz cavity as it appears on the oscilloscope.

The different peaks inside one FSR in this Figure can be interpreted in the following way. We have a laser frequency comb, which has a spectrum containing an equidistant grid of frequencies $f_n = f_0 + nf_r$, and a F-P cavity, which has resonances spaced by its free spectral range FSR $= c/2L$. The round trip length L of the cavity is adjusted such that every Mth mode of the frequency comb is resonant with subsequent modes of the cavity and is transmitted through it ($M = 16$ for the first cavity and $M = 10$ for the second cavity, in the case of cavities placed in

series). The comb frequencies which are transmitted are spaced by the quantity Mf_r, and they all contribute at the same time to give the intensity of the highest peak in the Figure. This is the desirable filtering situation, where a comb mode is transmitted every 16 (10) ones. As the cavity length is tuned with the PZT (i.e. FSR is changed a bit), the next set of Mf_r spaced comb modes (M is not an integer anymore) are brought into resonance, but now the transmitted comb modes and the resonance peaks of the cavity are not exactly overlapped, so that the transmitted modes are a bit suppressed (see the first peak at each side of the main peak in Figure 5.6). At this cavity length, filtering is a bit larger than a factor 16 (10) due to this Vernier effect [58]. Going on scanning the cavity, subsequent sets of Mf_r spaced modes are in resonance, with increasingly less transmitted power because of the worsening of the overlap. After scanning the cavity round trip length by a wavelength (i.e. one free spectral range), M groups of Mf_r spaced combs have passed by and the situation is as the beginning, the initial group is transmitted. After the initial alignment with the cw laser, the comb light can be used directly to recover small disalignments in day to day operation. I noticed that such small realignment is not frequently necessary and only some small PZT adjustment is usually enough to almost mantain the resonance condition over different days operation.

Finally, I report the procedure to align the two cavities in series. In fact, to fix the required cavity length for the 16 GHz cavity I need to use, as the input source, the comb light already filtered by the 1.6 GHz cavity. On the other hand, I already noticed the difficulty to align, from the beginning, a F-P cavity by using directly pulsed comb light. To solve this problem, I aligned the first cavity by using the cw laser following the above procedure. Then, I locked such cavity to one transmission peak of the cw laser following the procedure described in the next Subsection. This transmitted cw light is used to align the second cavity as done for the first one. I emphasize that the steps must be followed in this order, and that prior alignment of the second cavity with cw light without the first cavity along the optical path did not lead to a satisfactory alignment result, due to the fact that the optical components of the first cavity modify the Gaussian beam propagation and hence the coupling conditions of the second cavity. Once both cavities are aligned using the cw laser, the EDFA output fiber is placed in the fiber

collimator. The resonant condition for the comb in the first cavity was searched as explained above, and then locked to the maximum comb transmission (highest peak in Figure 5.6). In such a way, we have a 1.6 GHz comb spectrum at the output of the cavity, to be used to find the resonant condition for the second cavity.

5.1.3 The locking system

In order to use the cavities as a comb filter for calibration purposes, the resonant cavity length must be actively controlled, i.e. locked to the maximum transmission. The basic idea of a locking system is the following. A continuously recorded signal gives information on how cavity length fluctuations and drifts decrease the cavity transmission. This signal is called "error signal". Then, an electronic device, called proportional-integral-derivative (PID) amplifier, processes such error signal in terms of needed gain and appropriate sign, giving a correction signal used to control the actuator element. The actuator converts the correction signal into a mirror translation to compensate the fluctuation detected by the error signal, closing in such a way the locking loop. In our case this actuator is the PZT element.

The error signal is given by the fraction of the transmitted light detected by the DET10C photodiode (see Figure 5.4). If the aim is to mantain the maximum cavity transmission, such signal cannot be used as the error signal. In fact, transmission is a symmetric function with respect to the desired locking point, hence there is no way to discriminate fluctuations that increase the cavity length from those which decrease it. To this aim, I modulated the cavity length at low frequency (by applying to the PZT a sinusoidal signal of some kHz of modulation frequency and a modulation dept equal to the FWHM width of the transmission peak), and I obtained the first derivative of the transmission peak via a lock-in detection[8]. The output signal, thus, is proportional to the input signal derivative. Such dispersive signal can be used as a frequency discriminator to correct relative frequency fluctuations of the cavity against the comb modes. Figure 5.7 shows an example of the comb main peak with its derivative as visualized on the oscilloscope. The maximum of the transmission peak coincides with the passage through zero

[8] A lock-in amplifier is a device which takes a modulated input signal, multiplies it by a reference sinusoidal signal, extracting the fraction of the input signal in phase with the reference signal.

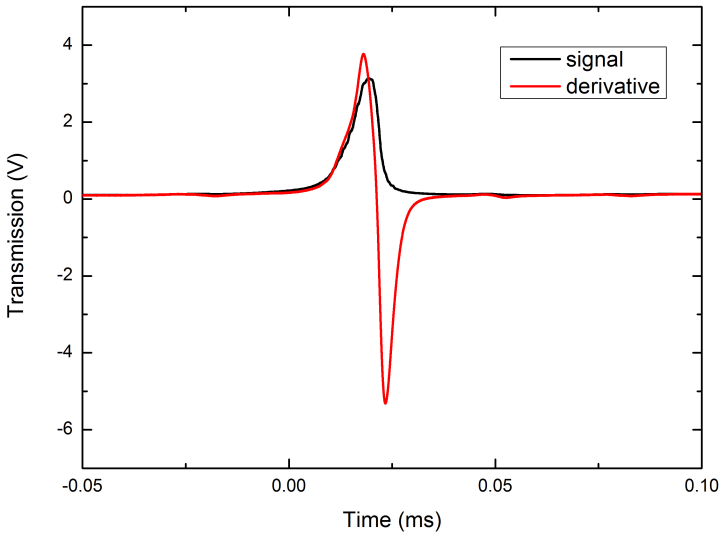

Figure 5.7: The comb main peak (black line) with its first derivative (red line) as a function of time (i.e. scanning the cavity).

of the derivative. Thus, we can lock the cavity to this 0 V point and the sign of the fluctuations can now be interpreted in the right way, since it corresponds to a positive or a negative value of the derivative.

The error signal is fed into the PID. This device behaves simply as an electronic amplifier with a tailored gain to control cavity fluctuations in the largest locking bandwidth as possible. In the case of F-P cavities, the most relevant frequency noise comes from acoustic and mechanical noise and temperature drifts. It appears clear that the time scales over which these noise sources are held and their relative magnitude are different, hence requiring a different gain to be corrected. The PID amplifier is adjusted to control them with the appropriate gain and response time. The signal is, then, inverted at the output of the PID, giving the right correction signal to be sent to the PZT. At this point, the feedback loop can be closed when the derivative signal crosses the zero value, mantaining the maximum transmission signal, as shown in Figure 5.8. The blue traces represent the transmitted signal (Figure 5.8-a) and the error signal (Figure 5.8-b) when the 1.6 GHz cavity is locked for a time interval of 20 seconds. As can be seen, the signal remains

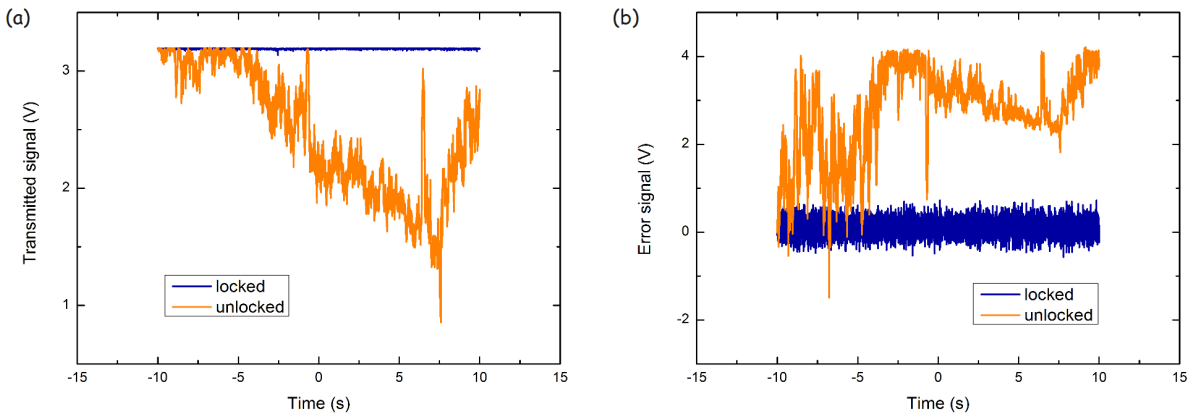

Figure 5.8: Transmitted signal (a) and error signal (b) in the case of a locked (blue) and unlocked (orange) cavity.

at its maximum transmission, while the error signal stays around zero. When the cavity is unlocked (orange traces), the signal, initially at its maximum transmission, quickly decreases (Figure 5.8-a), while the error signal drift away from the zero value (Figure 5.8-b).

To characterize the goodness of the locking, it is necessary to infer the time scale over which the system can be controlled. The used parameter is called "lock bandwidth", which gives the frequency interval where cavity length fluctuations are actively controlled. Whereas long term stability and controlled drifts are guaranteed automatically by the intergrator part of the PID[9], an estimate of the upper limit of the locking bandwidth must be inferred. Length fluctuations faster than this limit cannot be controlled. To measure such a response time, I computed, by Fourier transforming, the spectrum of the error signal when the cavity is unlocked and locked, respectively, and I subtracted the second spectrum from the first. In such a way, I observed that the resulting signal is > 0 up to about 500 Hz, while at higher frequencies it stays always around zero, showing that the locking system does not correct fluctuations beyond 500 Hz. This means that the system cannot be controlled for time intervals shorter than 2 ms.

[9] Anyway, when a sudden strong fluctuation larger than the dynamic range of capture occurs, the cavity becomes unlocked.

5.2 Analysis of the experimental results

In this Section, I will describe the experimental results obtained using dielectric cavities. I recorded the output spectra from each cavity by itself and from the two cavities in series with the aid of a spectrum analyzer and a low resolution spectrometer, placed after the second cavity, as shown in Figure 5.9. By using a folding mirror, the output light can be sent, in turn, to a fast

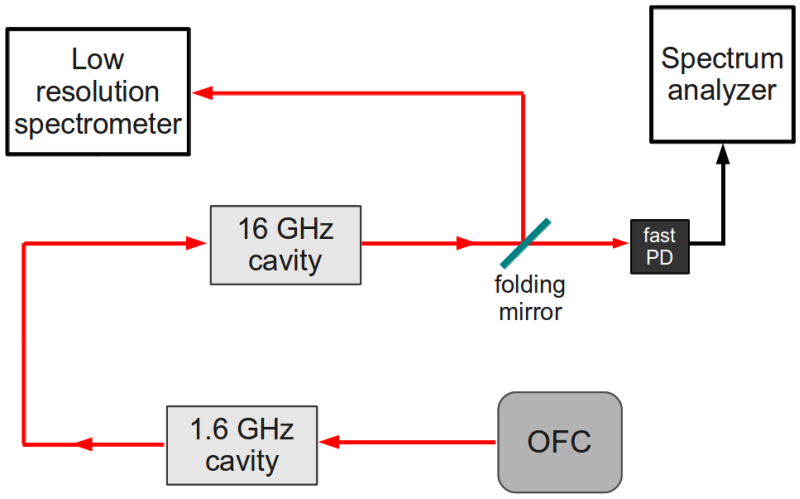

Figure 5.9: Layout for the measurement apparatus: after the second cavity, the outpur spectrum can be sent, by mean of a folding mirror, to a fast photodiode (PD) connected to a spectrum analyzer or to a low resolution spectrograph for the analysis.

photodiode connected to a spectrum analyzer to characterize the transmitted spectral features and the side mode suppression or directly to a low resolution spectrometer to infer the spectral bandwidth.

For what concerns the spectrum analyzer, this type of instrument is capable of measuring the amplitude of an input signal in the frequency domain. For this Thesis, I used the spectrum analyzer model MS2667C by Anritsu[10], which covers the range from 9 kHz to 30 GHz with a maximum resolution of 1 Hz. To be converted from the near-IR domain to the rf domain, the signal that reaches the spectrum analyzer is previously focused on a high-speed photodetector (model 1417M by Newport[11]). This detector has a flat response up to 25 GHz (i.e. it is able

[10] http://www.anritsu.com/en-GB/Home.aspx.
[11] http://search.newport.com/?q=*&x2=sku&q2=1417M.

to detect the output signal of both cavities) for an input signal in the spectral range 500−1650 nm. If we consider, for example, the first cavity, the expected signal on the spectrum analyzer would consist of a high peak at 1.6 GHz and smaller side peaks spaced by 100 MHz, suppressed by a factor which can be estimated by Equation 3.12. Moreover, we expect to find another high peak at 3.2 GHz, 4.8 GHz and so on, with the same pattern repeated every 1.6 GHz, since the first cavity transmits 1 comb mode every 16. In practice, on the spectrum analyzer we visualize the beatnotes of each comb mode with the others: since one mode every 16 is transmitted, the maximum contribution to the beating will be found every 1.6 GHz.

For what concerns, instead, the low resolution spectrometer, I used the Avaspec-NIR256 model by Avantes[12], which covers the spectral interval 900−2500 nm with a 7 nm resolution. Due to such a low resolution, individual spectral features cannot be detected with this instrument, but the overall spectral band, over which some transmitted signal is detectable, can be revealed. In this way, the effective spectral coverage of each cavity with respect to that of the comb output can be estimated.

5.2.1 Single cavity spectrum

To guarantee that each F-P cavity by itself behaves as expected, I studied first of all the transmitted output signal of each cavity alone as recorded on the spectrum analyzer and on the low resolution spectrometer. In this way, I can infer which are the side mode suppression of a single cavity, the power losses and the spectral bandwidth of each cavity.

First F-P cavity: 1.6 GHz

After optimizing the cavity length and locking the cavity output signal to the maximum transmission, I verified on the spectrum analyzer that a main peak of transmission appears every 1.6 GHz. I analyzed the interval of 1 GHz around 1.6 GHz, recording the amplitude of the 100 MHz spaced peaks, to infer the side mode suppression. In fact, since unwanted modes could come up due to the cavity geometry and alignment, it is important to estimate the suppression

[12] http://www.avantes.com/Spectrometers/AAvaSpec-NIR256/512-2.0/2.2/2.5TECNIRLine/Detailed-product-flyer.html

not only for the first adjacent mode but also for the following ones. The values of the suppression (expressed in dB) of the first 5 side beatnotes on the two sides of the 1.6 GHz beatnote are shown in Table 5.1. To visualize the obtained result, the spectrum between 1.1 and 2.1 GHz as recorded by the spectrum analyzer is shown in Figure 5.10.

Mode (GHz)	Suppression (dB)
1.1	-40.6
1.2	-45.3
1.3	-37.4
1.4	-36.0
1.5	**-33.0**
1.7	**-34.0**
1.8	-37.0
1.9	-46.8
2.0	-45.7
2.1	-42.2

Table 5.1: Suppression (expressed in dB) of the 100 MHz apart side modes with respect to the 1.6 GHz spaced modes due to the filtering of the 100 MHz comb with the 1.6 GHz cavity.

We can see that, apart from the beatnote due to the 1.6 GHz unfiltered modes, the most significant contribution comes from the beatnotes due to the first adjacent modes, as we expected. The following beatnotes, although they do not show a linear decreasing amplitude with respect to the 1.6 GHz beatnote, are all suppressed by a factor better than -36 dB. The suppression at 1.5 GHz results $\rho_{1.5} = -33$ dB, which corresponds to a cavity finesse $F_{1.5} = 361$, while the suppression at 1.7 GHz is $\rho_{1.7} = -34$ dB, which corresponds to $F_{1.7} = 405$. The finesse value inferred by the observed side mode suppression is worse than the value calculated with the cw laser (see Section 5.1.1). This could be ascribable to the fact that mirror coating can have a higher reflectivity around 1550 nm (at the wavelength of the cw laser) but could have a worse performance at the sides of the spectral range of the comb, resulting in a lower overall reflectivity. Nevertheless, as discussed in Section 4.2.1 a side mode suppression of at least -32 dB for the first cavity is enough for our aims. In conclusion, the performance of the first cavity satisfies the requirement in terms of desired filtering level.

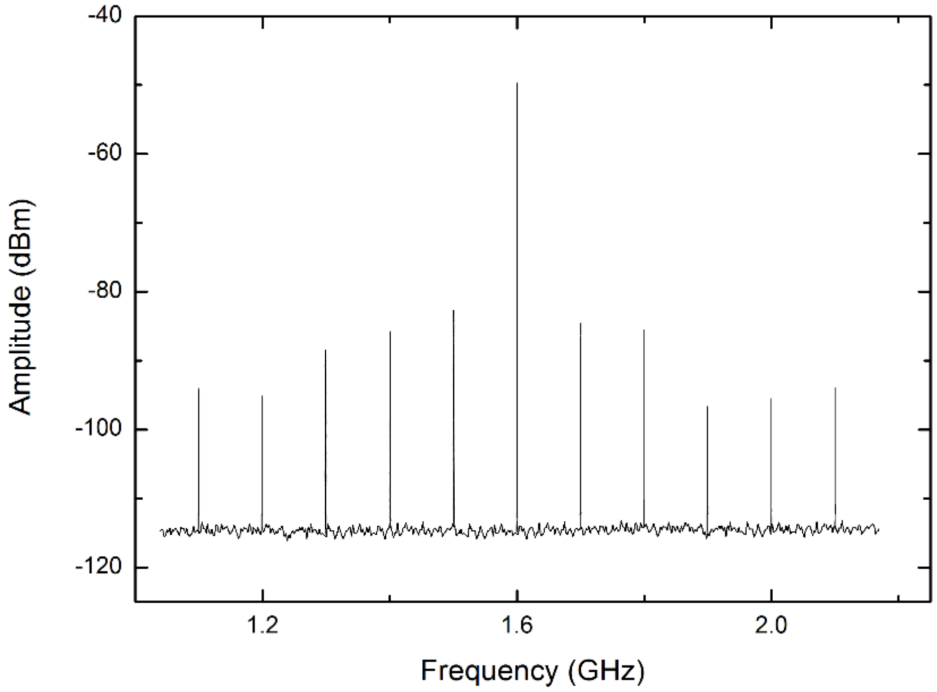

Figure 5.10: The observed beatnote spectrum after the first F-P cavity, illuminated by the 100 MHz comb spectrum.

For what concerns the power losses inside the cavity, I measured the total mean power immediately before and after the cavity with a power meter. For an input power $P_i = 177$ mW, I measured an output power $P_o = 2.56$ mW. The ratio $L = P_o/P_i$ gives the total losses of the first cavity: $L = 0.0145$. Multiplying L by a factor 16 (the losses due to the filtering itself) I obtained the losses L_c due to the cavity: $L_c = 0.23$. This means that we loose a factor 4 in power due to the cavity. These losses are mainly due to input coupling, mirror absorption and scattering, and not uniform intensity distribution of the input comb modes. The net effect is that the cavity behaves as an ideal cavity with a mirror reflectivity $R = 99.13\%$ ($F = 361$).

Second F-P cavity: 16 GHz

I inferred the properties of the spectrum generated by the second F-P cavity alone, as I made for the first cavity. The suppression of the 100 MHz apart spaced modes with respect to the 16

GHz spaced modes in a range of 2 GHz around 16 GHz are shown in Table 5.2.

As for the first cavity, the worst suppressed input comb modes contribute to the 15.9 GHz and 16.1 GHz beatnotes, as expected. The suppression of the 15.9 GHz beatnote with respect to the 16 GHz beatnote is $\rho_{15.9} = -12.0$ dB, which corresponds to a finesse $F_{15.9} = 350$ (reflectivity $R = 99.1\%$), while the suppression of the 16.1 GHz beatnote is $\rho_{16.1} = -12.8$ dB, which corresponds to $F_{16.1} = 342$ ($R = 99.08\%$). The obtained values of finesse are comparable with the ones obtained by analyzing the output spectrum from the first cavity.

As previously noticed, with this system configuration (one cavity with FSR = 1.6 GHz followed by a second one with FSR = 16 GHz) the advantage is that when the light from the first cavity enters the second one, the 15.9 GHz and 16.1 GHz spaced modes are already suppressed by a factor -33 dB and -34 dB, respectively (the side mode suppression measured with respect to

Mode (GHz)	Suppression (dB)
15.0	-32.3
15.1	-31.9
15.2	-32.2
15.3	-30.1
15.4	-27.3
15.5	-27.2
15.6	-26.2
15.7	-21.7
15.8	-18.2
15.9	**-13.0**
16.1	**-12.8**
16.2	-17.6
16.3	-21.4
16.4	-24.3
16.5	-26.8
16.6	-27.2
16.7	-28.2
16.8	-29.8
16.9	-31.3
17.0	-31.7

Table 5.2: Suppression (expressed in dB) of the 100 MHz apart side modes with respect to the 16 GHz modes due to the filtering of the 100 MHz comb with the 16 GHz cavity.

the 1.6 GHz beatnote is the same for each harmonic of FSR = 1.6 GHz). Hence, I expect that the 100 MHz adjacent modes are suppressed by a factor around -45 dB. The attention needs to be moved, instead, on the 1.6 GHz spaced side modes, i.e. the 14.4, 12.8, 11.2 GHz beatnotes and so on, on one side, and the 17.6, 19.2 GHz beatnotes[13], on the other side, with respect to the 16 GHz one. These modes will be less suppressed since they are totally transmitted by the first cavity. In Table 5.3 I show the suppression measured for the 1.6 GHz spaced modes with respect to the 16 GHz ones. As can be seen from Table 5.3, the 1.6 GHz side modes stay always

Mode (GHz)	Suppression (dB)
9.6	-38.4
11.2	-40.3
12.8	-32.1
14.4	-38.2
17.6	-36.5
19.2	-32.2

Table 5.3: Suppression (expressed in dB) of the 1.6 GHz spaced side modes with respect to the 16 GHz ones due to the filtering of the 100 MHz comb with the 16 GHz cavity.

below a factor -32 dB of suppression with respect to the main modes, so we can conclude that the second cavity guarantees the required side mode suppression for the modes we are interested in. Nevertheless, such result will be more clear for the suppression measurements made with two cavities in series, as reported below. What can be noticed is that the 3.2 GHz spaced modes (i.e. those that contribute to the 12.8 and 19.2 GHz beatnotes) are less suppressed that the 1.6 GHz spaced modes. This kind of disuniformities can be in part ascribed to disomogeneities in the intensity distribution of the comb modes at the beginning and to a non-flat response of the detector with frequency. On the other hand, the symmetry of the situation on both sides of 16 GHz can be envisaged also as a systematic effect which leads the 3.2 GHz spaced modes to be less suppressed than the 1.6 GHz ones. The recorded spectrum between 14.4 GHz and 16.6 GHz, as visualized on the spectrum analyzer, is shown in Figure 5.11.

[13]Beatnote frequencies higher than 20 GHz have not been measured due to the fact that the dynamic range of the spectrum analyzer did not allow to detect such small signatures at those frequencies.

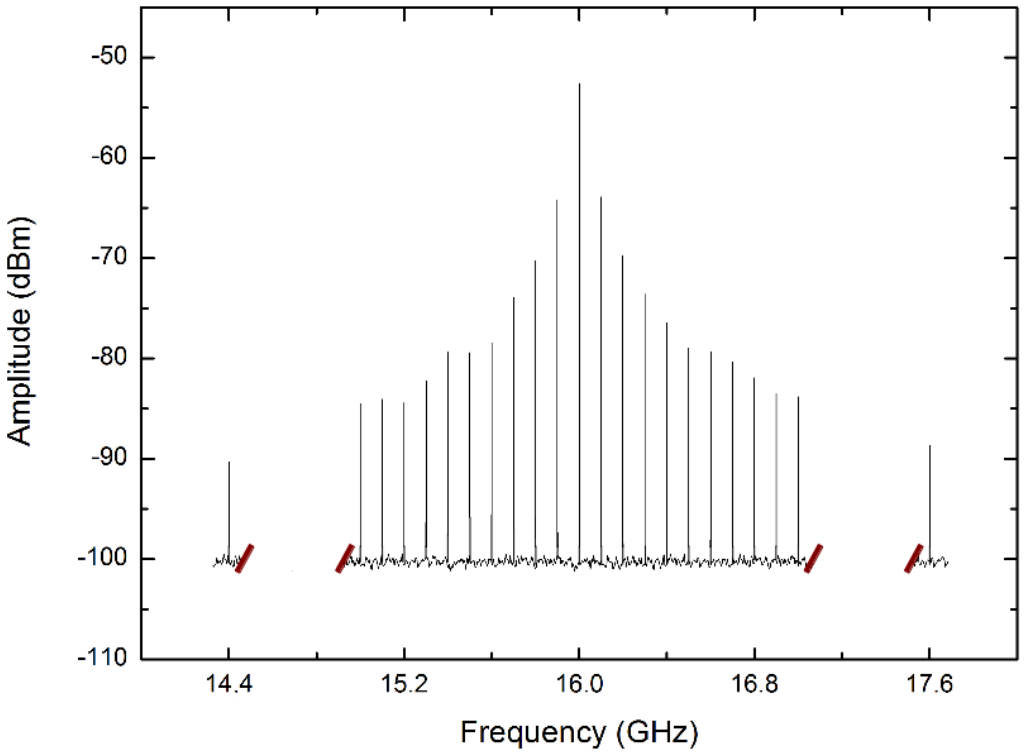

Figure 5.11: The observed beatnote spectrum after the second F-P cavity illuminated by a 100 MHz comb light.

For what concerns the power losses, as for the first cavity I measured the total mean power immediately before and after the cavity with a power meter and I obtained $P_i = 174.4$ mW and $P_o = 358$ μW. I, hence, measured a total loss $L = 0.00205$. Considering a filtering factor of 160 (from 100 MHz to 16 GHz), the losses due to the cavity itself can be estimated as $L_c = 0.33$, i.e. we loose a factor 3 in power due to the cavity coupling.

The second important parameter that characterizes the filtering cavities is the spectral coverage. I measured the filtering spectral coverage of each cavity alone when illuminated with a comb spectrum between approximately 1500 and 1650 nm. Figure 5.12 compares the spectral bandwidth of the EDFA output spectrum with that of the spectra after the first and the second F-P cavities. As can be seen, the EDFA output spectrum covers a spectral region of about 140

nm[14] between 1490 nm and 1630 nm. The output spectrum from the first cavity reduces the spectral bandwidth to a 80 nm wide region between 1510 nm and 1590 nm. The second cavity, instead, has an output spectrum that covers a 95 nm bandwidth between 1505 nm and 1600 nm. The first cavity, thus, results the most significant for the bandwidth decrease: this is due to the fact that, for the same mirror coating, it has a smaller FSR with respect to the second cavity and the dispersion at the sides of the spectral interval of interest is, hence, more relevant. Anyway, a nominal GDD < 100 fs^2 is, in general, not enough to avoid narrower coverage due to dispersion.

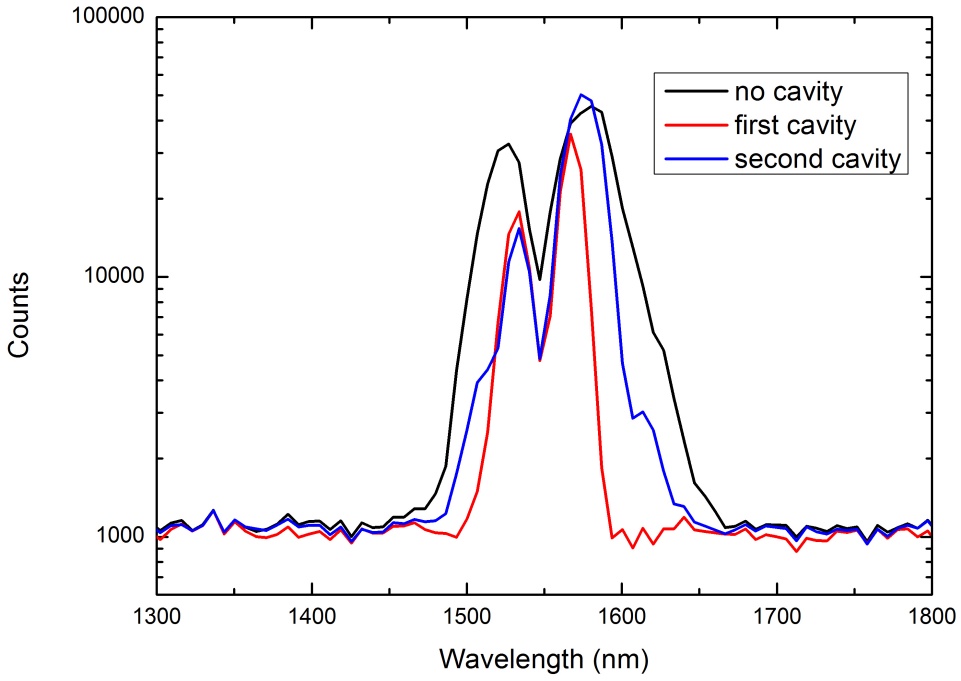

Figure 5.12: Spectral bandwidth of the output spectrum from the EDFA and from each of the two cavities alone when illuminated with the 100 MHz EDFA output.

5.2.2 Two F-P cavities in series

After having verified that the two cavities in series are well aligned by using the cw laser and optimized the trasmission signal on the oscilloscope, the comb light can be sent through the

[14]Computed as the $1/e$ width.

system and the output spectrum can be recorded on the spectrum analyzer. A plot of the filtered comb beatnote spectrum after the two cavities in series is shown in Figure 5.13. Due to the low power level that reaches the fast detector, the main peak (16 GHz) has a measured amplitude of -60.6 dBm, while the background has a mean amplitude of -104 dBm. This means that spectral features suppressed more than -43.4 dB cannot be observed. As noticed in the previous Section, we expect a suppression of the 100 MHz adjacent modes (15.9 GHz and 16.1 GHz beatnotes) of

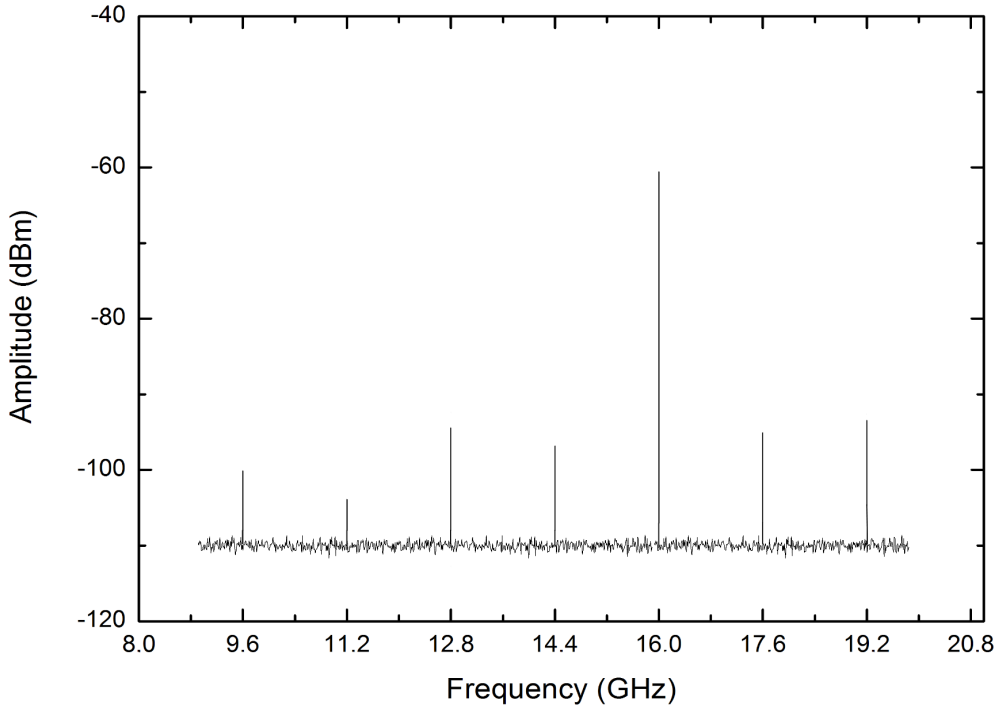

Figure 5.13: The observed beatnote spectrum after two F-P cavities in series.

a factor -45 dB. Hence, I was limited by the spectrum analyzer dynamic range, and thus I was only able to verify that no spectral features are visible at 15.9 and 16.1 GHz and this guarantees that these modes are suppressed by a factor at least -43.4 dB.

As explained, the most relevant modes are those spaced 1.6 GHz and 3.2 GHz from the 16 GHz ones. The suppression of these modes with respect to the main one is shown in Table 5.4. As can be seen, each unwanted mode is suppressed by at least a factor -32.7 dB. The worst cases are again those of the 3.2 GHz spaced side modes (12.8 GHz and 19.2 GHz beatnotes), but also

Mode (GHz)	Suppression (dB)
9.6	-39.5
11.2	-42.8
12.8	**-32.9**
14.4	-36.7
17.6	-34.5
19.2	**-32.7**

Table 5.4: Suppression (expressed in dB) of the 1.6 GHz spaced side modes with respect to the 16 GHz ones after the filtering of the 100 MHz comb with two cavities in series, FSR = 1.6 GHz for the first one and FSR = 16 GHz for the second one.

in this case the measured suppression is better than the required condition of -32 dB suppression.

Finally, I give an estimate of the total power losses. First of all, an overall factor 160 of power is lost due to the filtering process itself. I also measured the losses L_c due each cavity (a factor 4 for the first cavity and a factor 3 for the second one) and the total mean power in front of the optical fiber which brings the output light to the fast photodetector after removing the second cavity, to estimate the losses due to the passage through the 3-lenses system, the beam splitter mirrors and the optical isolator and due to the subsequent reflections on the mirrors in front of the second cavity and of the output fiber collimator. I measured a final power (without the second cavity) $P'_f = 1.95$ mW, so I estimated the losses due to the optical components between the output of the first cavity and the final optical fiber as $L_f = P'_f/P_o = 0.76$. Moreover, I measured a factor 0.6 of losses due to all the optical components between the EDFA output and the first cavity (expecially waveplates and isolator). If we start with a maximum mean power $P_i = 450$ mW, the remaining mean power in front of the final fiber collimator thus results: $P_f = 107$ μW.

To conclude the characterization of the filtered spectrum, in Figure 5.14 I show the low resolution spectrum after the two cavities in series and, for comparison, the spectrum from the comb EDFA itself. As can be seen, the final spectrum covers a 80 nm wide region between 1510 and 1590 nm, mainly limited by the first cavity spectral coverage. The final bandwidth results, hence, reduced with respect to the starting one. Nevertheless, a 80 nm spectral band is

still sufficient, if the necessary power is provided, to reach an octave spanning spectrum using a HNLF for the broadening.

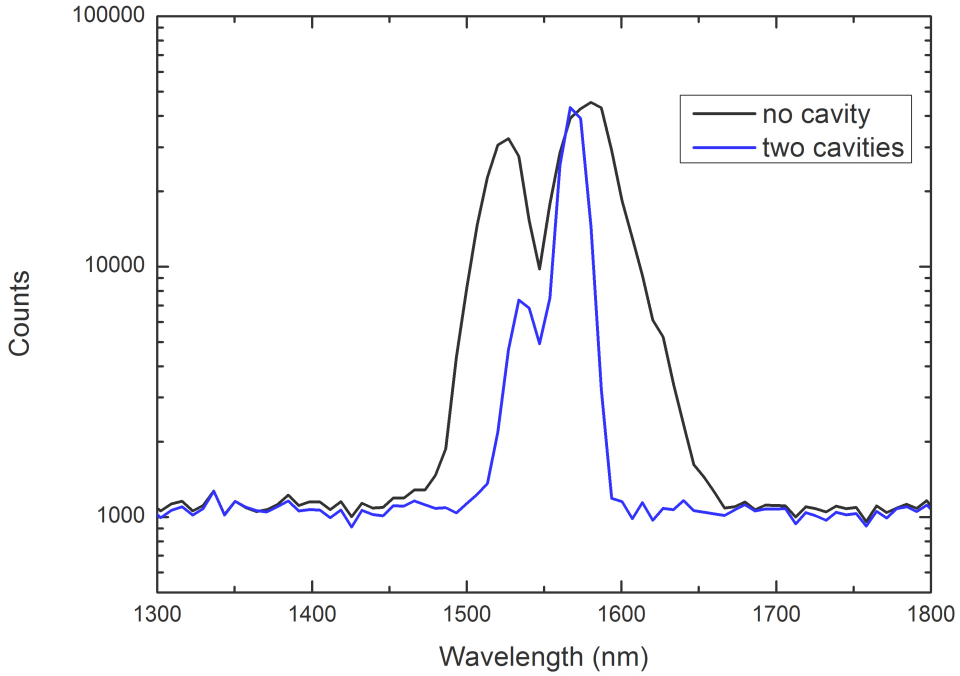

Figure 5.14: The spectral bandwidth after the two cavities in series (blue curve) and, for comparison, the EDFA output bandwidth (black curve).

Chapter 6

An alternative approach: metallic coated mirrors

In this Chapter, I will describe a new alternative approach to filter the comb light in the 1−2 μm range. As explained, the ideal situation would be to start with an octave spanning comb spectrum and to filter the whole spectrum directly with 2 high finesse F-P cavities in series to obtain a -32 dB side mode suppression. Due to the dispersion problem with high finesse F-P cavities, this approach cannot be realized in such a simple way. The set-up described up to now (and already realized in a 400 nm limited range around 1.5 μm [85]) is challenging to cover an octave or more spanning spectrum. Alternatively, one can think of giving up the high finesse requirement and use three cavities in series instead of two. In this case, the lower reflectivity implies the possibility of introducing metallic coated mirrors instead of dielectric coated ones, making possible to filter directly the whole octave spanning initial comb spectrum.

I designed metallic cavities that use mirrors with the same optical geometry than the dielectric ones (i.e. one plane-plane mirror and one plane-concave mirror with 100 mm of curvature radius). In this way, the cavity set-up and system optical layout remains unchanged (apart from the third cavity to be introduced after the second one). In addition, it is necessary to put the cavities in vacuum because the air dispersion would worsen the filtering in the case of an octave spanning spectrum (see Section 3.4.2). Unfortunately, it is very difficult to find a supplier that provides

metallic mirrors with some transmission and relatively high reflectivity due to the high absorption of light by such coatings. This fact has prevented, up to now, the use of this kind of non-dispersive cavities for purposes like the one described in this Thesis. The most suitable choice of metallic mirrors I found has arrived just few months before the end of this Thesis work. For this reason, I did not have enough time to develop the whole system with metallic coated mirrors, so in the following I will simply discuss the feasibility of this system. After having identified the most suitable metallic coated mirrors, I substituted them in the 1.6 GHz cavity and I measured the cavity properties (in particular, the side mode suppression, the mean output power and the spectral coverage) in the limited $1.5-1.65$ μm range to compare them with the performances of the 1.6 GHz cavity in the case of dielectric coated mirrors. In such a way I will be able to infer the advantages and disadvantages of this second approach and to conclude which of the two approaches is the most suitable for this astronomical application.

6.1 Metallic coated mirrors

Since up to now filtering the comb spectrum with metallic coated mirror cavities has been proposed just as an idea ("[..] metallic mirrors that are broad band with virtually no dispersion can be used virtually eliminating the bandwidth limiting dispersion." [75]), I first of all considered the feasibility of the idea. In the case of dielectric coated mirrors, multiple thin layers of dielectric material are deposited on a substrate: choosing the appropriate materials and thickness of the layers, it is possible to design a coating with the desired properties. For this Thesis, I chose a broadband coating with nominal reflectivity $R = (99.5 \pm 0.2)\%$. Moreover, I measured the transmission of a single mirror, which is $T = 0.45\%$. Since it must be that $R+T+A = 1$ (A are the losses due to absorption), it results that the dielectric coated mirror losses due to absorption are basically negligible.

This is not the case for metallic coated mirrors. In fact, in this case, we deal with a conductor material instead of an insulator one. The conduction electrons undergo collisions with the thermally agitated lattice or with imperfections, irreversibly converting electromagnetic energy into Joule heat. The absorption of radiant energy in a given metal is a function of its conductivity.

As an electromagnetic wave progresses into the conductor (along the z-axis), its initial amplitude I_0 is exponentially attenuated:

$$I(z) = I_0\, e^{-\alpha z}\,, \tag{6.1}$$

where $\alpha = 4\pi f n_I/c$ is the *attenuation coefficient* [98] (n_I is the imaginary part of the refraction index). The flux density drops to a value $1/e$ after the wave has propagated for a distance $z = 1/\alpha$, known as the *penetration depth*. For a material to be transparent, the penetration depth must be large compared to its thickness. The penetration depth for metals is, instead, exceedingly small so that in general metals are opaque. In this case, it results that $R + A = 1$ and no transmission at all is observed. Nevertheless, metals can become partly transparent when formed into extremely thin films on a substrate: asking for a given transmission $T = I_T/I_0$, from Equation 6.1 one can compute the corresponding thickness z_T knowing α of the metal.

For what concerns the reflectivity, the metals with higher reflectivity in the near-IR range are Au, Ag and Al. Asking some optics suppliers for the better material to use, silver coated mirrors seem at the end the most suitable. In fact, the coating needs to be deposited on fused silica substrates (transparent to the near-IR) and in the case of gold there are adherence problems to bond it on silica. In the case of Al instead, it oxidizes faster than Ag and finesse would deteriorate faster as a consequence.

6.1.1 Coating properties

As for 2 F-P cavities in series a good choice in terms of finesse was to put $\mathrm{FSR}_1 = 1.6$ GHz and $\mathrm{FSR}_2 = 16$ GHz, in the case of 3 cavities a good choice would be: $\mathrm{FSR}_1 = 1.6$ GHz, $\mathrm{FSR}_2 = 8$ GHz and $\mathrm{FSR}_3 = 16$ GHz. In this configuration a side mode suppression of at least -32 dB of each side mode can be obtained with a cavity finesse $F = 90$ ($R = 96.5\%$) for each cavity.

The requirements for the mirrors are, hence, the following: a thin silver coating (some tens of nm depending on the wanted transmission) deposited on fused silica substrates with a reflectivity of at least 96.5% and some degree of transmission. I chose to try two sets of mirrors by Layertec GmbH with the nominal characteristics shown in Table 6.1.

Properties	Provided Values (set I)	Provided Values (set II)
Reflectivity (nominal)	$(98.5 \pm 0.5)\%$	$(97.5 \pm 0.5)\%$
Transmission (nominal)	$(0.2 \pm 0.1)\%$	$(0.4 \pm 0.2)\%$
Diameter (pl-pl)	(6.35 ± 0.1) mm	(6.35 ± 0.1) mm
Diameter (pl-conc)	(12.7 ± 0.1) mm	(12.7 ± 0.1) mm
Thickness (pl-pl)	(2.31 ± 0.1) mm	(2.31 ± 0.1) mm
Thickness (pl-conc)	(6.35 ± 0.1) mm	(6.35 ± 0.1) mm
Radius of curvature	100 mm	100 mm
Anti Reflection coating (0°)	$< 0.7\%$	$< 0.7\%$

Table 6.1: Nominal characteristics of the two sets of metallic coated mirrors as provided by Layertec GmbH.

The plane-concave mirror substrates are of the same dimensions as the dielectric case, while for the plane-plane mirror substrates the thickness is the same as plane-plane dielectric mirrors but the diameter was halved. As a consequence, I also used a different type of PZT, with an internal diameter of 2 mm and an external one of 3 mm (piezo-stack model PSt 150/2x3/7 by Piezomechanik GmbH[1], able to a maximum expansion of 13 μm with 150 V). With the reduced plane-plane mirror dimension and the different PZT transducer, the response bandwidth of the locking electronics was increased. A plot of the expected reflectivity for both sets as provided by Layertec GmbH is shown in Figure 6.1. The reflectivity is variable along the spectral range

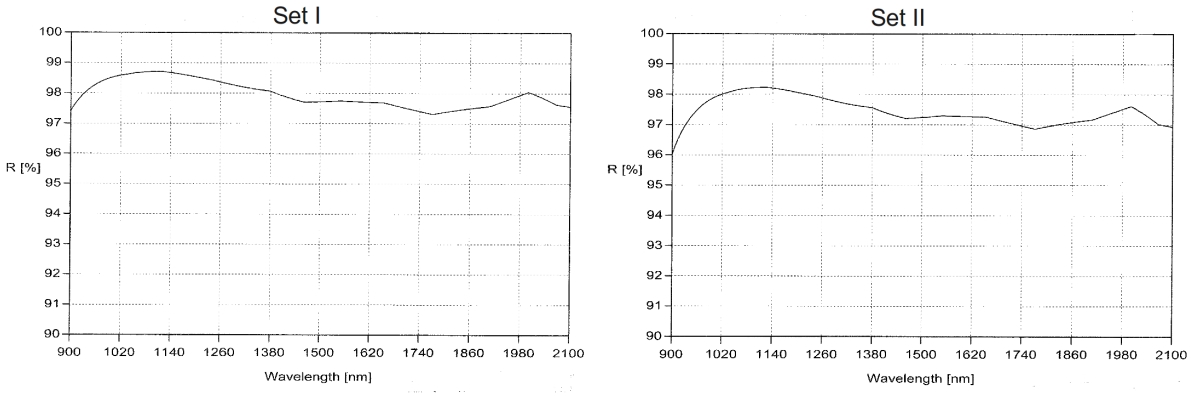

Figure 6.1: Plot of the expected reflectivity as a function of wavelength as provided by Layertec GmbH, for both sets of metallic coated mirrors.

[1] http://www.piezomechanik.com/en/home/introduction/index.html?1=.

of interest with a maximum change of 1%.

6.1.2 Mirror characterization

As for dielectric mirrors cavities, I used the cw laser at 1554 nm to align the metallic mirrors ones. I measured the finesse (i.e. reflectivity) at the cw laser wavelength by using the transmitted spectrum. A plot of such spectrum when one FSR was scanned is shown in Figure 6.2. Following the procedure I described in Section 5.1.2, I measured a cavity finesse $F = 221$, i.e. a reflectivity nearly $R = 98.6\%$, for set I mirrors, while, for set II, I obtained a finesse $F = 178$, which means a reflectivity $R = 98.2\%$.

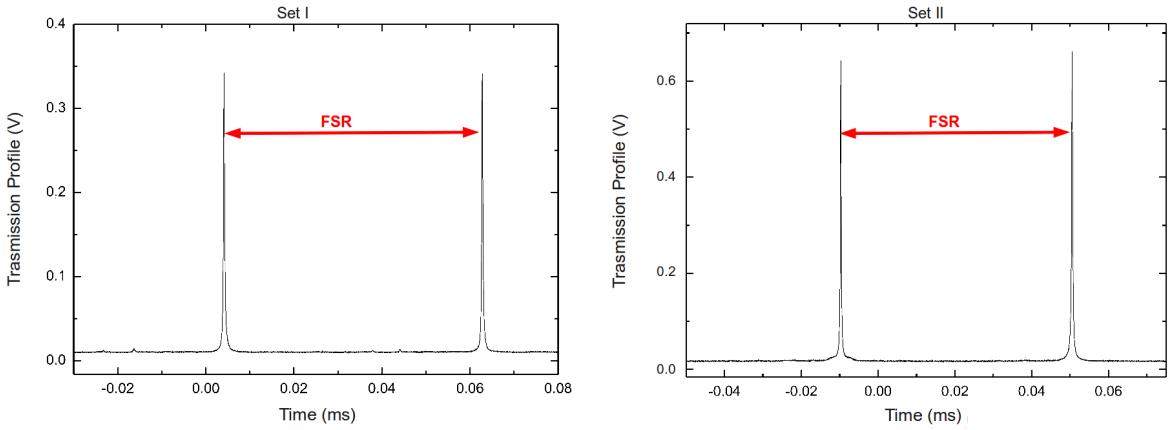

Figure 6.2: Plot of the transmission profile of the cw laser after the first F-P cavity for both sets of mirrors as a function of time.

These measured finesses are higher than the expected values for both sets of mirrors, as inferred in Figure 6.1. Anyway, this is a measurement with a monochromatic source, so that a lower reflectivity at other wavelenghts between 1−2 μm would be expected. As for dielectric mirrors cavities, reflectivity values for the comb light will be evaluated by using the side mode suppression measurements.

6.2 Characterization of the 1.6 GHz filtering cavity

As already explained, I limited my analysis to the 1.6 GHz F-P cavity. In addition, I limited the characterization measurements to the spectral range 1500−1650 nm for a better comparison with the analogous dielectric mirrors cavity. The experimental set-up to measure the side mode suppression, the transmitted mean power and the spectral coverage was the same used for dielectric mirrors cavities. I pointed out that the minimum cavity finesse for each one of the three cavities in series to reach the goal of a final -32 dB side mode suppression is $F = 90$. It means that, for a single cavity with 1.6 GHz free spectral range, the required side mode suppression of the 100 MHz adjacent mode is $\rho = -20.8$ dB (see Equation 3.12). Hence, I verified if this level of suppression can be reached with the metallic coated mirrors in the 1500−1650 nm range.

I also measured the total mean power after the cavity. In fact, while the computed power losses after the first cavity for the dielectric case are a factor 4, for the metallic case I expect more significant power losses, due to the higher absorption of the coating. Finally, I measured the filtering spectral bandwidth of such cavity for both sets of mirrors.

6.2.1 Results with set I metallic mirrors

This set is the one with the lower nominal transmission ($T = (0.2 \pm 0.1)\%$) and hence with the higher reflectivity. A plot of the 1.6 GHz beatnote and the side beatnotes as recorded by the spectrum analyzer is shown in Figure 6.3. The computed suppression of the 100 MHz apart modes in a 1.2 GHz range around 1.6 GHz with respect to the 1.6 GHz spaced modes are shown in Table 6.2. The less suppressed modes are the 100 MHz adjacent ones (1.5 and 1.7 GHz spaced modes) and they are suppressed by $\rho_{1.5} = -23.1$ dB and $\rho_{1.7} = -23.2$ dB, respectively. These values of suppression correspond to a cavity finesse $F_{1.5} = 116$ ($R = 97.3\%$) and $F_{1.7} = 118$ ($R = 97.3\%$). While these values are lower compared with those computed with the cw laser and even with those provided by Layertec, they are still better than the minimum performances required to reach a final -32 dB suppression.

For what concerns the mean output power, with an input power $P_i = 280$ mW immediately before the cavity, I measured an output power $P_o = 110$ μW. The total losses, thus, result

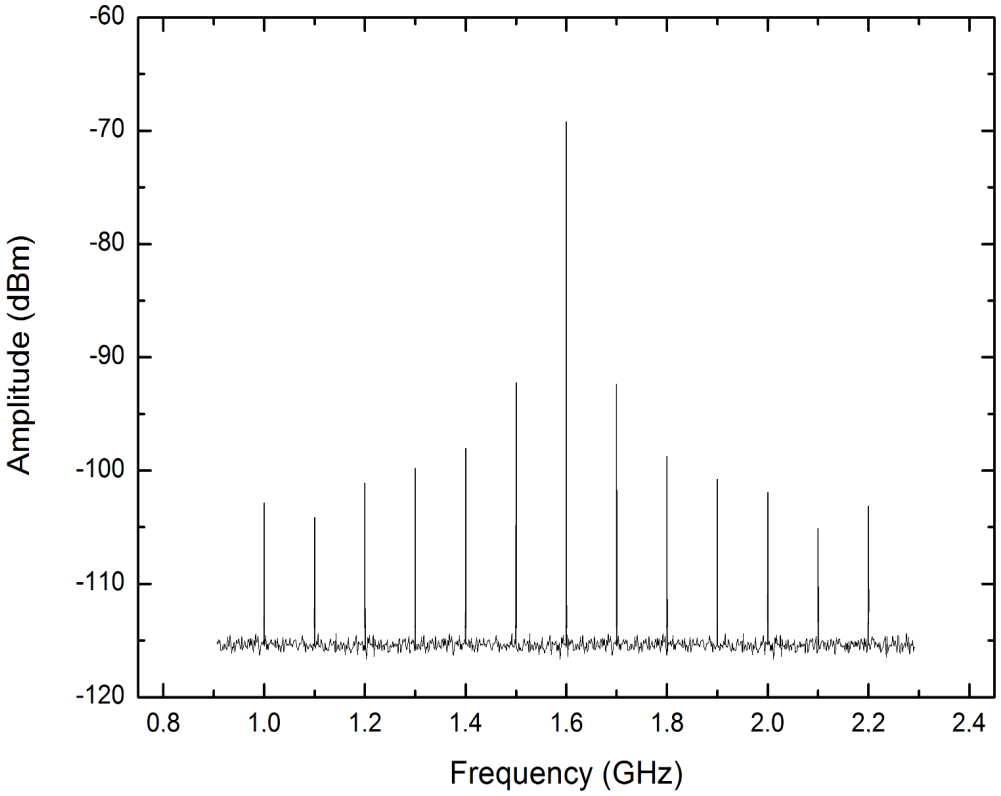

Figure 6.3: Plot of the 1.6 GHz beatnote and of the side beatnotes from suppressed modes in a 1.2 GHz range around 1.6 GHz in the case of the first set of metallic coated mirrors.

$L = P_o/P_i = 4 \times 10^{-4}$ and the cavity losses can be obtained multipling by the filtering factor ($m = 16$): $L_c = 6 \times 10^{-3}$. This means that the power losses due to the cavity mirrors are a factor 40 higher than the case of dielectric coated mirrors, due mainly to the higher mirror absorption of such metallic coatings.

Regarding the spectral bandwidth, one of the advantages of using metallic coated mirrors instead of dielectric coated ones is that no dispersion problems due to the coating are present. I checked that the spectral bandwidth after the filtering cavity is the same as without any cavity. The results are shown in Figure 6.4: as can be seen, the bandwidth of the spectrum after the cavity is not significantly different with respect to that at the EDFA output.

Mode (GHz)	Suppression (dB)
1.0	-33.7
1.1	-35.0
1.2	-31.9
1.3	-30.6
1.4	-28.8
1.5	**-23.1**
1.7	**-23.2**
1.8	-29.5
1.9	-31.6
2.0	-32.1
2.1	-35.9
2.2	-33.9

Table 6.2: Suppression (expressed in dB) of the 100 MHz apart side modes with respect to the 1.6 GHz modes for the first set of metallic coated mirrors.

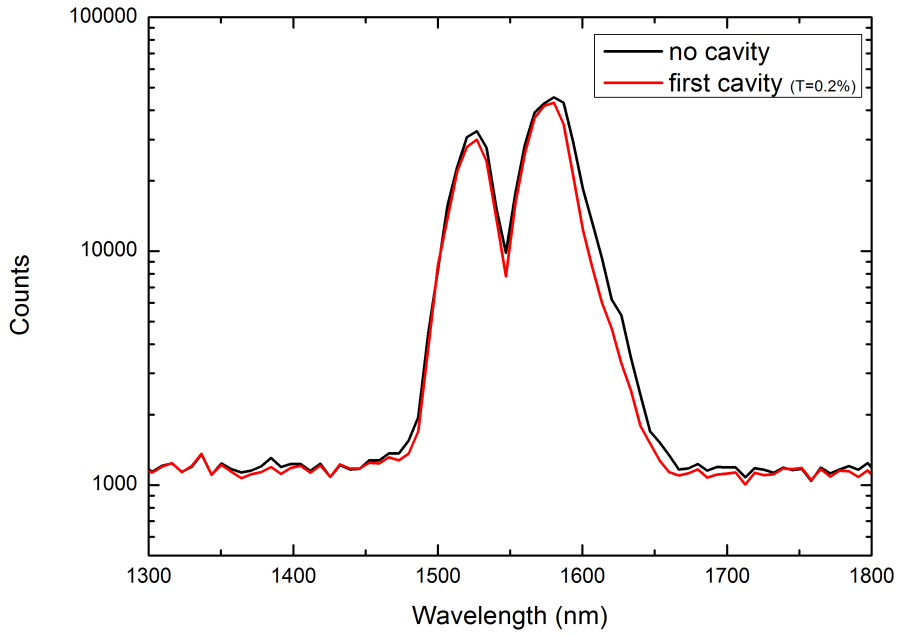

Figure 6.4: Comparison of the spectral bandwidth after the first cavity with that of the EDFA spectrum using set I mirrors.

6.2.2 Results with set II metallic mirrors

This set of mirrors has a higher transmission (nominal $T = (0.4 \pm 0.2)\%$) and a lower reflectivity, so we can expect a worse side mode suppression. The suppression computed for the 100 MHz apart side modes in a 1.2 GHz range around 1.6 GHz with respect to the 1.6 GHz modes are shown in Table 6.3. Now the suppression for the closest 100 MHz adjacent modes results

Mode (GHz)	Suppression (dB)
1.0	-30.1
1.1	-33.5
1.2	-31.0
1.3	-28.7
1.4	-26.1
1.5	**-20.5**
1.7	**-21.0**
1.8	-27.0
1.9	-29.3
2.0	-31.8
2.1	-34.8
2.2	-31.1

Table 6.3: Suppression (expressed in dB) of the 100 MHz side modes with respect to the 1.6 GHz mode for the second set of metallic coated mirrors.

$\rho_{1.5} = -20.5$ dB ($F = 86.5$ and $R = 96.4\%$) and $\rho_{1.7} = -21.0$ dB ($F = 91.6$ and $R = 96.6\%$), respectively. For the 1.5 GHz spaced modes the suppression is a bit lower than the minimum required, so that this set of mirrors is borderline for our application. A plot of the 1.6 GHz beatnote and of the suppressed side beatnotes as they appear on the spectrum analyzer is shown in Figure 6.5.

Although I found a worse side mode suppression, this set of mirrors can ensure lower power losses. In fact, starting with 280 mW of power in front of the cavity, I measured a power $P_o = 0.75$ mW after the cavity, leading to $L = 2.7 \times 10^{-3}$ and $L_c = 4.3 \times 10^{-2}$. The cavity losses are hence nearly a factor 10 smaller than the first set of mirrors.

For what concerns the spectral bandwidth, also this set of mirrors does not affect the spectral coverage of the EDFA output spectrum before the cavity, as shown in Figure 6.6.

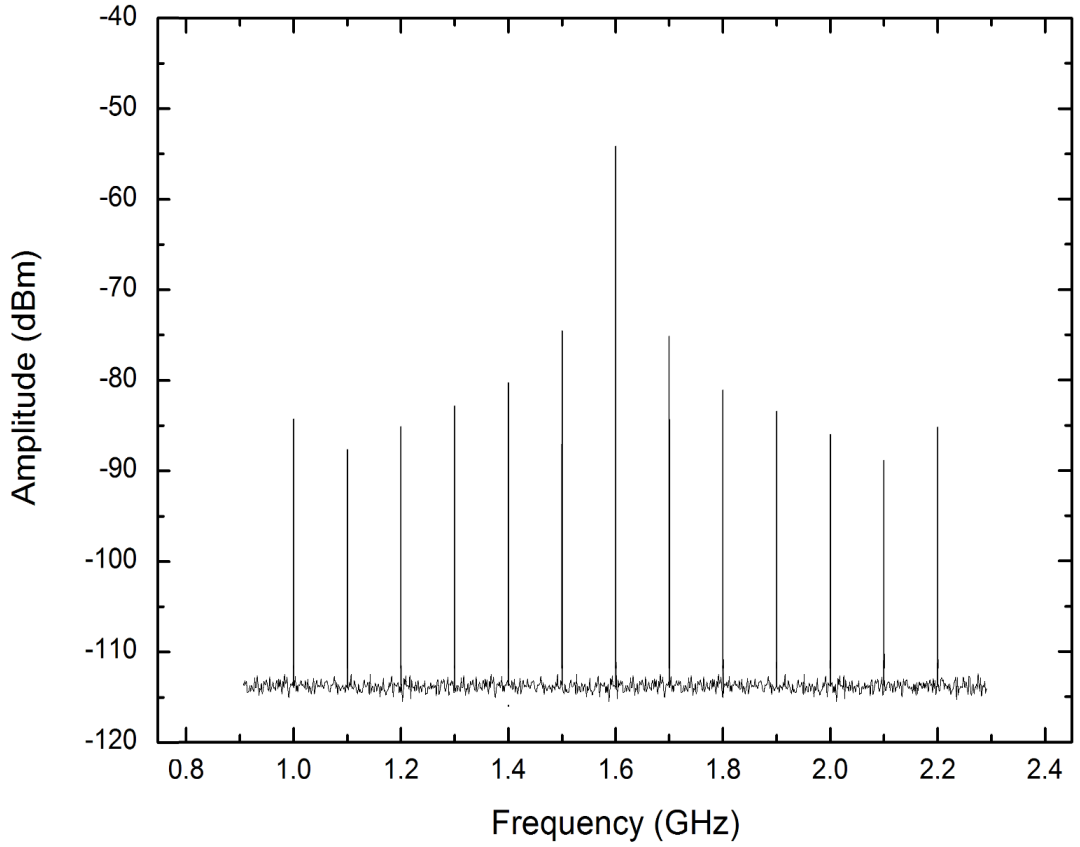

Figure 6.5: Plot of the 1.6 GHz beatnote and of the side beatnotes in a 1.2 GHz range around 1.6 GHz in the case of the second set of metallic coated mirrors.

6.3 Feasibility of this approach

The above characterization shows that a 100 MHz side mode suppression of -32 dB would be guaranteed for the three cavities configuration in the case of both sets of mirrors (set II is borderline). For a general discussion of the expected side mode suppression of the final system, I computed that the the 1.6 GHz spaced modes transmitted by the first cavity are filtered to more than -50 dB by the second (FSR = 8 GHz) and the third (FSR = 16 GHz) cavities in series. For what concerns, instead, the 8 GHz spaced modes transmitted by the second cavity, they will be suppressed to a factor higher than -32 dB by the third 16 GHz cavity.

The obtained results allow also to do some general considerations regarding the final expected

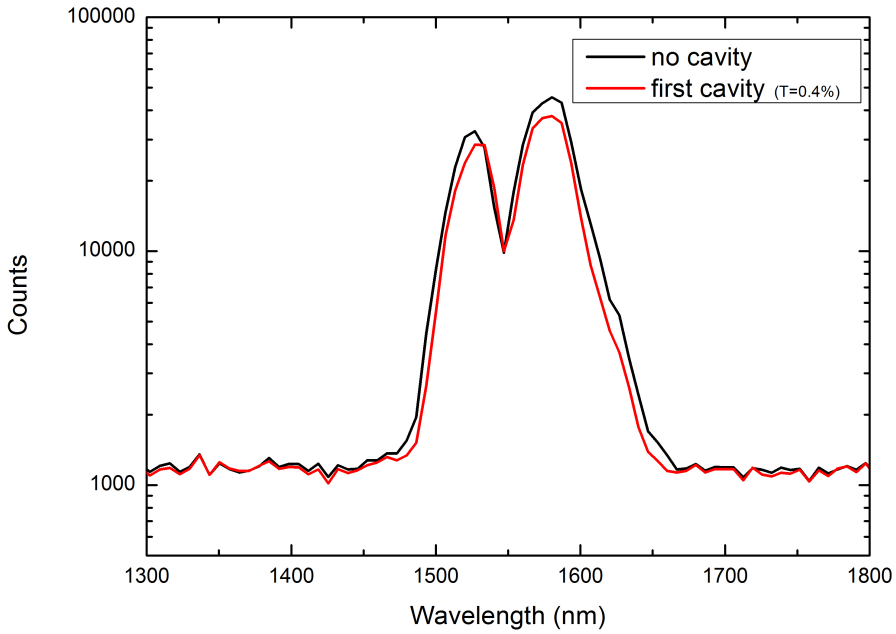

Figure 6.6: Comparison of the spectral bandwidth after the first cavity with that of the EDFA spectrum using set II mirrors.

mean power. Supposing that the cavity losses are the same for each cavity, in the case of three cavities in series the overall losses (considering also the factor 160 due to the filtering) would be $L_1 = 1.4 \times 10^{-9}$ in the case of set I and $L_2 = 5 \times 10^{-7}$ in the case of set II. Assuming that all comb modes have the same intensity, I computed in Section 4.2.1 that the total mean power in the range 1.5−1.65 μm after the filtering should be at least 2−20 pW. For the case of set I, the resulting final power, starting with 450 mW of mean power, would be $P_o = 600$ pW, while for set II it would be $P_o = 200$ nW. In both cases the final power is enough to be detected by the spectrograph. Moreover, a minimum input power of 15 mW for set I mirrors and 42 μW for set II mirrors would be enough to get the required filtered output power of 20 pW in the narrow spectral range 1500−1650 nm. Instead, for the 1−2 μm range, the power requirements for the Giano calibration spectrum are 2−20 nW of mean power, which can be reached with an input power of 1.5−15 W and 4−42 mW for three cavities in series with set I and set II mirrors,

respectively. Due to the fact that comb powers higher than hundreds of mW are difficult to achieve in this octave spanning range, the solution with set II mirrors seems the most suitable one for the astro-comb application.

For what concerns spectral coverage, the above results in the limited 1500−1650 nm range support that dispersion problems are avoided with this metallic mirrors approach.

Chapter 7

Discussion and conclusions

In this Thesis, I proposed two different approaches to filter a comb source for astronomical calibration purposes. In particular, a near-IR frequency comb with 100 MHz repetition rate was filtered up to a factor 160 to produce a 16 GHz comb calibration spectrum for the Giano spectrograph. In fact, investigation of possible terrestrial planets aroud M-type stars with such astronomical spectrograph requires a precision of about 1 m/s in radial velocity measurements. To allow such a precision in Doppler-shifts measurements over a wide spectral range (1−2.5 μm), it is mandatory to calibrate the spectrograph with a spectrum of uniformly spaced lines such those from a filtered laser comb. Filtering the comb over a wide spectral range is a not resolved issue at the moment. Interferometric systems such as Fabry-Perot cavities has given, up to now, the most promising results. This is the approach I followed in my Thesis work. In fact, the early period of my Thesis was devoted to find and analyze which could be the best solution for the purpose of filtering the comb spectrum. In this context, I spent one month at Max Plank Institute of Quantum Optics (MPQ) in Munich, where one of the two leader research groups in the world has developed such a system for a visible astronomical spectrograph. After this period, I identified two possible approaches to the problem, which have been developed during this Thesis. In Chapter 5, I described the experimental results obtained by filtering a limited portion of the comb spectrum with two F-P cavities in series made of dielectric coated mirrors; in Chapter 6, instead, I proposed a different and original solution to the problem, i.e. filtering the

comb with three F-P cavities in series made of metallic coated mirrors. In both cases, particular attention was put in developing a reliable, stable and compact system for a real application as the Giano calibration source.

In this Chapter, I will discuss the experimental results presented in this Thesis, outlining the advantages and disadvantages of the two followed approaches with the aim of concluding which is the best arrangement to be used at a real telescope. Since the first approach (dielectric mirrors cavities in series) is the only one that has been followed in literature up to now, I will also briefly compare the results presented in this Thesis with those obtained by other research groups in the field of astronomical application of frequency combs (already summarized in Section 3.6).

7.1 Advantages and disadvantages of dielectric cavities

In Section 3.3.1, I showed that the filtering cavity finesse (i.e. mirror reflectivity) is the parameter which defines the side mode suppression level. Calibration of spectrographs like Giano requires a side mode suppression up to -32 dB for a 100 MHz comb filtered by a factor 160. I also pointed out the impossibility of reaching such suppression level with just one cavity, while a relaxed constraint in finesse can be provided by using multiple cavities in series. The approach that guarantees enough side mode suppression with the minor number of cavities in series (i.e. with a simpler and more compact system) is the one that uses dielectric coated mirrors. This is, hence, the first advantage of using dielectric cavities. Nevertheless, mirrors with such a high reflectivity cannot be used for a broad filtering spectral range due to dispersion of dielectric coatings. This is the main drawback of this approach. The cavity-comb mismatches due to dispersion effects prevent to cover the whole spectral range of the comb source, so that the filtering must be limited to a reduced portion of the spectrum (1.5−1.65 μm in our case). To overcome such limitation, spectral broadening of the filtered comb can be obtained by using HNLFs and photonic fibers. In this case, however, the power needed by non-linear broadening effects requires to use intermediate laser amplification stages. Both amplification and non-linear broadening degrade the side mode suppression as well as increase the final cost of the system.

The other main advantage of using dielectric mirrors is that they provide low absorption

losses. Recalling the condition $R + T + A = 1$ (see Section 6.1), I found that $R \simeq 99.5\%$ and $T \simeq 0.45\%$, so that it results: $A \simeq 0.05\%$. In terms of cavity losses (due to coupling, absorption and scattering), I found that the mean power after the first cavity was reduced by a factor 4 and after the second one by a factor 3, neglecting the filtering losses. Comparing these losses with the power losses due to the filtering process itself (a factor 160), the total cavity losses (4×3) result more than one order of magnitude smaller.

The results obtained by using dielectric cavities can be analyzed in the context of the results obtained by other research groups, as described in Section 3.6. In fact, the common idea, although developed differently by each research group, is the same: filtering a reduced portion of the comb spectrum to a mode spacing suitable for an astronomical spectrograph and then broadening this filtered spectrum in a HNLF or photonic fiber. I compare my results with those obtained by NIST group, since it is the only one which developed a system starting with an Er-doped fiber comb, i.e. in the same spectral region as the work discussed in this Thesis.

First of all, they started with a 250 MHz repetition rate comb instead of 100 MHz. This is really favourable in terms of side mode suppression: using dielectric coated mirrors with $R = 99.5\%$, as in the case of my Thesis, the theoretical suppression of the first adjacent mode filtering with two identical 16 GHz cavities would be -36 dB if starting with a 100 MHz comb and -52 dB if starting with a 250 MHz comb. This means that lower requirements for mirrors reflectivity would be necessary in the case of a 250 MHz comb to reach the same side mode suppression as with a 100 MHz comb.

In their work they filtered a reduced spectral interval of just 30 nm around 1.5 μm and broadened it with a HNLF up to almost 400 nm. Moreover, a fiber laser amplification up to 400 mW after the filtering process has been implemented to allow such a broadening. With the aim of developing a similar broadening system in our case (but with the difference of reaching an octave spanning filtered spectrum), more than one amplification stage will be necessary, strongly increasing the total cost of the system. In addition, I would expect to find similar, or even worse, difficulties due to the degrading of the suppression as a consequence of such amplification and broadening processes. In fact, the problem, found also by the other reasearch groups working at

visible wavelengths, is that after the broadening stage most of the unwanted modes come up again, worsening the overall side mode suppression. In the case of the NIST group, at some wavelengths the adjacent modes were increased by a factor up to 40 dB, so that at those wavelengths the side mode suppression became of the order of just -20 dB. This effect can be ascribed to the highly non-linear effects in the broadening fiber. In fact, the power amplifier before the fiber not only increases the power of the wanted modes, but also that of the less suppressed modes, which play a significant role in the non-linear processes inside the fiber (see Section 3.6). Moreover, they observed high asymmetry in the side modes intensity after the broadening process.

From the above analysis, an octave spanning filtered spectrum with the required suppression for our case can be reached by filtering up to -70 dB or more before laser amplification and HNLF broadening. Such a high suppression requires higher finesse cavities, making likely the use of three dielectric cavities in series instead of two.

Finally, I would like to mention that I found the same intracavity power losses as in the case of NIST cavities (a factor 4).

7.2 Advantages and disadvantages of metallic cavities

The listed above problems, connected with the use of dielectric cavities, led me to explore new solutions. In this Thesis, I showed for the first time the feasibility of using metallic mirrors cavities instead of dielectric ones. As already pointed out, the main advantage of metallic mirrors is that they are virtually free from dispersion due to coating. In fact, results about the spectral coverage measured for the 1.6 GHz metallic mirrors cavity show no reduction of the input comb bandwidth. In this sense, filtering cavities with this kind of mirrors allow to simplify the experimental set-up by filtering directly the $1-2$ μm comb light, removing the broadening stage.

On the other hand, there are two main disadvantages in following the metallic mirrors approach. First of all, the coating reflectivity is lower than the dielectric case, making necessary to introduce a third cavity, to be controlled independently. This fact makes the system more complex and less compact. Secondly, metallic cavities cause considerable intracavity power losses. In fact, studying the behaviour of the 1.6 GHz cavity alone, I recorded cavity power losses of a

factor 6×10^{-3} for one set of mirrors (set I) and 4×10^{-2} for the other (set II), hence a factor 40 and 5 higher than the first dielectric cavity. While in the second case the cavity losses remains smaller than the filtering losses, in case of set I mirrors they become comparable. As shown in Section 6.3, for the case of $1-2$ μm comb source, an initial maximum mean power of 15 W and 40 mW would be necessary using set I and set II mirrors, respectively. A mean power of some watts is really difficult to obtain for an octave spanning near-IR comb, and hence set I mirrors cannot be used for the purpose of three filtering cavities in series. Instead, in the case of set II mirrors, the required initial power can be easily achieved, making possible the use of this type of mirrors for the Giano's calibration system.

7.3 Conclusions

To summarize, I developed two filtering systems to get a 16 GHz spaced comb spectrum. The first one is composed by two cavities in series made of dielectric coated mirrors with 1.6 GHz and 16 GHz FSRs, respectively. Such a system filters the input 100 MHz comb spectrum to more than -43.4 dB of side mode suppression for the 100 MHz adjacent modes and more than -32 dB for the 1.6 GHz spaced ones, in the $1510-1590$ nm spectral range.

The second system is arranged with three cavities in series made of metallic coated mirrors with 1.6 GHz, 8 GHz and 16 GHz FSRs, respectively. The characterization measurements of the 1.6 GHz cavity in the reduced $1500-1650$ nm spectral range with two different sets of metallic mirrors allow me to conclude that a finesse up to 90 for each cavity is enough to guarantee a suppression higher than -32 dB for the 100 MHz apart filtered side modes in all this spectral range. Instead, mirrors with a transmission of at least 0.3% are necessary to reach enough transmitted power for the unfiltered modes to be detected by Giano.

Taking into account these results and considering the advantages and disadvantages of both dielectric and metallic mirrors cavities, I conclude stating that the original approach I proposed, i.e. that of cavities with set II metallic mirrors, is the best choice to be mounted at a real spectrograph, as Giano. In fact, despite the complexity of arranging a system with three cavities in series instead of two, the most crucial stage seems to be the spectral broadening in a HNLF.

With metallic cavities, this stage is removed, since it is possible to filter directly an octave spanning spectrum. In this sense, the disadvantage of having three cavities is completely cancelled out by the advantage of discarding the broadening process. Moreover, taking into account the availability of near-IR combs with higher repetition rates (up to 250 MHz), a comb spectrum suitable for the Giano calibration can be developed by using two metallic cavities in series with a finesse of 90 and 4 GHz and 16 GHz FSRs, respectively.

Finally, I would like to note that in the case of the calibration of just the echelle orders between 1500 and 1650 nm, the system with dielectric cavities could be useful.

7.3.1 Perspectives

The first future step will be to implement the set-up with metallic cavities, first of all introducing the second (FSR = 8 GHz) and third (FSR = 16 GHz) cavities, secondly substituting the 1.5−1.65 μm light with the 1−2 μm spectrum. In this way, I plane to obtain for the first time an octave spanning 16 GHz comb spectrum for astronomical calibration.

Next, it will be necessary to test the system on the Giano detector, to measure the overall resolution provided by the filtered spectrum. Moreover, new solutions could be investigated. In particular, also the 2−2.5 μm spectral region, not covered by an Er-doped fiber comb, needs to be calibrated, so that, for example, different comb sources can be considered to calibrate the Giano detector at these wavelengths.

Appendix A

Theory of mode locking

A mode locked (ML) laser is a type of laser which can store a single pulse and maintain it on a repetitive path. After each round trip a copy of the pulse is emitted through the output mirror of the laser cavity resulting in an indefinite train of laser pulses. In the following the basic principles of operation of a ML laser are described.

A.1 Mathematical background

First of all, I assume that there is no dispersion in the laser cavity, so that the propagation speed of the wave packet (group velocity) is the same as the phase velocity. Moreover, I suppose (unrealistically) that the spectrum of an inhomogeneously broadened laser consists of a series of lines of constant amplitude spaced by the cavity free spectral range f_c [96]. If there are N lines, the total width Δf_{inhom}, is:

$$\Delta f_{inhom} = (N-1) f_c \,. \tag{A.1}$$

The total electric field is:

$$E_{tot} = E_0 \sum_{-(N-1)/2}^{+(N-1)/2} \exp\left[i(\omega_0 + n\omega_c)t + i\phi_n(t)\right], \tag{A.2}$$

where ω_0 is the center frequency, E_0 the electric field for each line and $\phi_n(t)$ a random function of time uniformly distributed between 0 and 2π. If I_0 is the intensity of each line, the time-averaged

intensity results as $\langle I \rangle = NI_0$, where the cross-terms, responsible of a random interference among the laser modes, average to zero.

Now suppose that there is a mechanism for locking the phases of all the lines together, so that $\phi_n(t)$ can be taken out of the sum in Equation (A.2). The total field in this case is:

$$E_{tot} = E_0 e^{i\omega_0 t + i\phi(t)} \sum_{-(N-1)/2}^{(N+1)/2} e^{in\omega_c t} = E_0 e^{i\omega_0 t + i\phi(t)} \frac{\sin N\omega_c t/2}{\sin \omega_c t/2} \tag{A.3}$$

and the intensity is:

$$I = I_0 \left[\frac{\sin N\omega_c t/2}{\sin \omega_c t/2} \right] . \tag{A.4}$$

The peak intensity of this function results:

$$I_{peak} = N^2 I_0 \tag{A.5}$$

and the temporal width of each pulse is roughly $\Delta t_p \simeq 1/Nf_c \simeq 1/\Delta f_{inhom}$, with $f_c = \omega_c/2\pi$. As can be seen from Equation (A.5), the locking process increases the peak power for each pulse over the cw laser average power by a factor N and generates pulses with a duty cycle $f_c \Delta t_p = 1/N$. The average power is the same as for a cw laser, but the peak power can reach very high values when Δt_p is of the order of some femtoseconds.

The basic conceptual diagram to illustrate how the phases can be locked together is shown in Figure A.1: the basic technique consists in the introduction of an intracavity shutter which is arranged to cyclically open and close with a period exactly equal to the round trip time of the intracavity wave. In these conditions, the only surviving field distribution is a regular series of pulses with the same repetition rate as the shutter cycling frequency, i.e. the cavity free spectral range. From Fourier theory, it can be inferred that the only frequency dependence which can generate this field distribution is a series of uniformly spaced modes separated by the cavity free spectral range.

A more realistic starting distribution is an inhomogeneously broadened laser with a Gaussian

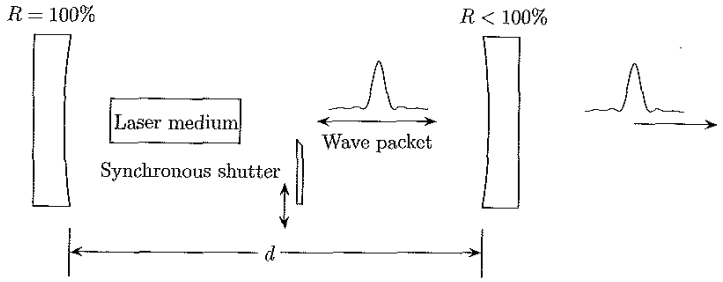

Figure A.1: Conceptual diagram of a ML laser [96].

envelope of modes instead of uniformly intense modes. The electric field of the nth mode is:

$$E_n = E_0 \exp\left[-2\ln 2\left(\frac{n\omega_c}{\Delta\omega}\right)^2\right] , \tag{A.6}$$

where E_0 is the electric field at the peak of the Gaussian and $\Delta\omega$ the inhomogeneous width. The electric field in the time domain can be expressed as:

$$E(t) = \sum_{-(N-1)/2}^{+(N-1)/2} E_n e^{i\omega_0 t + in\omega_c t} = E_0 e^{i\omega_0 t} \sum_{-(N-1)/2}^{+(N-1)/2} \left\{\exp\left[-2\ln 2\left(\frac{n\omega_c}{\Delta\omega}\right)^2\right]\right\} e^{i\omega_c t} . \tag{A.7}$$

To infer the single pulse shape, I suppose that N is so large that the sum in Equation (A.7) can be converted to an integral, with the substitutions $x = n\omega_c$ and $dx = (n+1/2)\omega_c - (n-1/2)\omega_c = \omega_c$. The electric field becomes:

$$E(t) = \frac{E_0 e^{i\omega_0 t}}{\omega_c} \int_{-\infty}^{+\infty} \left\{exp\left[-\frac{2(\ln 2)x^2}{(\Delta\omega)^2}\right]\right\} e^{ixt} dx . \tag{A.8}$$

The intensity can be obtained by solving the integral and taking the square modulus:

$$I(t) = I_0 \exp\left[-2\left(\frac{\Delta\omega t}{2\sqrt{\ln 2}}\right)^2\right] . \tag{A.9}$$

Thus the pulse is Gaussian-shaped with a width:

$$\Delta t_p = \frac{2\ln 2}{\pi}\frac{2\pi}{\Delta\omega} = \frac{0.44}{\Delta f} . \tag{A.10}$$

A.2 Mode locking techniques

The mode locking condition can be obtained in two general ways: the **active mode locking**, which is realized when an external shutter which opens and closes at the mode spacing frequency is used (as in the explained conceptual model) and the **passive mode locking**, which uses some non-linear optical effect in the intracavity medium as an "internal shutter". In an actively ML laser, the shutter is an amplitude or a phase modulator placed inside the cavity. The amplitude modulation is usually achieved with an acousto-optic modulator. In the case of phase modulation, an electro-optic modulator or a Pockel cell is placed near one of the cavity mirrors and acts modulating the optical path length in the cavity, achieving the same condition as if the cavity mirror would move back and forth at the modulation frequency.

The most common way to realize the mode locking condition is to use some non-linear behaviour of the intracavity medium, i.e. the passive mode locking. The most exploited techniques are the saturable absorption and the Kerr-lens mode locking. A saturable absorber is characterized by an absorption which, due to saturation, decreases with increasing intensity. Let assume that each pulse has E photons per unit area and, hence, an average flux per pulse of E/t_p. Moreover, the pulse time dependence is assumed to be rectangular, of width t_p. Modelling the saturating medium as a two-level system with level population densities N_1 and N_2, respectively, the population densities satisfy a rate equation at each point in space:

$$\frac{dN_1}{dt} = R(N_2 - N_1) + N_2/\tau \,, \tag{A.11}$$

where R is the stimulated rate and τ the lifetime of level 2. If the wave propagates along the z-axis, the loss in photon flux per unit length is equal to the number of absorptions per unit time per unit volume:

$$\frac{d}{dz}\left(\frac{E}{t_p}\right) = -R(N_1 - N_2) \,. \tag{A.12}$$

The last two Equations can be solved imposing the initial condition that all the population is in the ground state at $t = 0$ and knowing the initial population $N_{1,in}$; thus, the fractional absorption

per unit length results:

$$\alpha = \frac{N_{1,in}\sigma s t_p}{2\sigma E + s t_p} + \frac{2N_{1,in}\sigma^2 E}{(2\sigma E + s t_p)^2}\left[1 - e^{-(2\sigma E + s t_p)}\right] , \tag{A.13}$$

where $s = 1/\tau$ and $\sigma = Rt_p/E$. From this Equation it can be seen, first of all, that α is a monotonically decreasing function of $1/t_p$: the loss decreases as the pulses get shorter, so that the passive mode locking favors very short (of the order of fs) pulses, and this is the reason why it is the most suitable scheme for fs-lasers. Moreover, when $st_p < 1$ (i.e. the pulse width is smaller than the population lifetime), the loss becomes nearly independent of t_p and hence the the pulse width will tend to approach the population lifetime, which is typically of the order of some tens of femtoseconds.

The Kerr-lens mode locking is based on the **optical Kerr effect**. Due to this effect, the refractive index of a medium is proportional to the squared electric field (the intensity I) via the relation $n = n_0 + n_2 I$. The radial intensity distribution of a Gaussian beam is:

$$I = I_0 e^{-2r^2/\omega_0^2} \tag{A.14}$$

and the total phase shift for a medium of length L results:

$$\phi = \frac{2\pi n L}{\lambda} . \tag{A.15}$$

Thus, the change in the phase shift due to the intensity distribution is:

$$d\phi = \frac{2\pi L}{\lambda} dn = \frac{2\pi L n_2 I_0}{\lambda} e^{-2r^2/\omega_0^2} \simeq \frac{2\pi L n_2 I_0}{\lambda}(1 - 2r^2/\omega_0^2) , \tag{A.16}$$

where the last relation is valid in the proximity of the beam center ($r \ll \omega_0$). The quadratic dependence of the change in phase shift with radial distance is characteristic of a positive lens: the beam is more focused with increasing intensity.

A.3 Dispersion

In a non-dispersive system, the wave number k has a linear dependence on the angular frequency ω ($k = n\omega/c$) and the refraction index n is constant with ω; a dispersive system is, instead, characterized by a non-trivial dependence of n on ω: $n(\omega)$. When considering a pulsed laser, each pulse has a finite width and each frequency which composes the pulse travels with a slightly different phase velocity due to dispersion; as a consequence, the pulse shape changes and the pulse is broadened.

First of all, we introduce the **group velocity** as the velocity of the pulse and the **phase velocity** as the velocity of the constant phase surfaces of the pulse (the wavefronts). The pulse is described as a continuous sum of components whose frequencies differ only slightly from each other and which are arranged to cancel outside of a finite time interval Δt_p:

$$E(z,t) = \int_{-\infty}^{+\infty} A_\omega(\omega - \omega_0) e^{ik(\omega)z - i\omega t} d\omega \; . \tag{A.17}$$

We expand the wave number around ω:

$$k(\omega) = k_0 + \left(\frac{\partial k}{\partial \omega}\right)_{\omega_0} (\omega - \omega_0) + ... \tag{A.18}$$

and substitute in Equation (A.17):

$$E(z,t) = e^{i(k_o z - \omega_0 t)} \int_{-\infty}^{+\infty} A_\omega(\Delta\omega) \exp\left\{-i\Delta\omega \left[t - \left(\frac{\partial k}{\partial \omega}\right)_{\omega_0} z\right]\right\} d\Delta\omega \; , \tag{A.19}$$

where $\Delta\omega = \omega - \omega_0$. Calling $A[\,]$ the integral, we can write:

$$E(z,t) = A\left[t - \left(\frac{\partial k}{\partial \omega}\right)_{\omega_0} z\right] e^{i(k_0 z - \omega_0 t)} \; . \tag{A.20}$$

The field is, hence, the product of a plane wave propagating along the z-axis with speed ω_0/k_0 and an envelope function, $A[t-(\partial k/\partial\omega)z]$, propagating in the same direction with speed $v_g = \partial\omega/\partial k$ (group velocity). The two speeds are the same just in the case of a linear dispersion function.

For simplicity we assume the case of normal dispersion, i.e. the index of refraction, $n(k)$, monotonically increases with frequency. The surfaces of constant phase travel at the phase velocity:

$$v_\phi = \frac{\omega(k)}{k} = \frac{c}{n(k)} \,. \tag{A.21}$$

Differentiating Equation (A.21), we obtain:

$$v_g = \frac{c}{n(k) + \omega \frac{dn(\omega)}{d\omega}} \,. \tag{A.22}$$

In a dispersive medium, a pulse with temporal width t_p at $z = 0$ will spread to $t_p + \Delta t_p$ at $z = l$:

$$\Delta t_p \simeq \frac{1}{(v_g)_{min}} - \frac{1}{(v_g)_{max}} \simeq l \frac{\Delta(1/v_g)}{\Delta\omega} \Delta\omega = l \frac{\Delta(\partial k/\partial\omega)}{\Delta\omega} \Delta\omega = l \left(\frac{\partial^2 k}{\partial\omega^2}\right)_{\omega_0} \Delta\omega \,, \tag{A.23}$$

where $\Delta\omega$ is the spread of frequencies in the pulse. If we assume a quadratic dependence of k on ω:

$$k(\omega) = k_0 + \left(\frac{\partial k}{\partial\omega}\right)_{\omega_0} (\omega - \omega_0) + \frac{1}{2} \left(\frac{\partial^2 k}{\partial\omega^2}\right)_{\omega_0} (\omega - \omega_0)^2 \,, \tag{A.24}$$

from Equation (A.23) it results that the pulse spreads as it propagates and the spread is proportional to the traveled distance. The second derivative of k with respect to ω is called **group velocity dispersion** (GVD):

$$\text{GVD} = \left(\frac{\partial^2 k}{\partial\omega^2}\right)_{\omega_0} = \left(\frac{\partial(1/v_g)}{\partial\omega}\right)_{\omega_0} \,. \tag{A.25}$$

The **group delay dispersion** (GDD) is, then, obtained by multipling GVD by the traveled distance. Since the phase ϕ accumulated by a wave in a distance l is kl, GDD can be seen as the second derivative of ϕ with respect to ω.

Appendix B

Waist and radius of curvature of a Gaussian beam

The behaviour of a thin collimated beam which propagates along the z-axis can be described using the *paraxial wave equation*. The wave equation can be expressed as [97]:

$$\nabla^2 u + k^2 u = 0\,, \tag{B.1}$$

where u is any component of the electromagnetic field and k is the wave vector. Since the wave propagates along the z-axis, u can be expressed as $u = \psi(x, y, z)e^{+ikz}$, where ψ is the field amplitude, whose dependence on x, y, z is much slower than $\exp(ikz)$. Substituting this expression in Equation B.1, we obtain:

$$\nabla_\perp^2 \psi + \frac{\partial^2}{\partial z^2}\psi + 2ik\frac{\partial}{\partial z}\psi = 0\,, \tag{B.2}$$

where $\nabla_\perp^2 = \partial^2/\partial x^2 + \partial^2/\partial y^2$. If we assume that ψ varies so slowly in z that $\mid \partial\psi/\partial z \mid \ll k\psi$, we can neglect $\partial^2\psi/\partial z^2$ with respect to $k\partial\psi/\partial z$ and we obtain the paraxial wave equation [97]:

$$\nabla_\perp^2 \psi + 2ik\frac{\partial}{\partial z}\psi = 0\,, \tag{B.3}$$

for the field amplitude in a linear, homogeneous and isotropic medium.

One solution of Equation B.3 is given by [97]:

$$\psi = \exp\left[i\left(P + \frac{k}{2q}a^2\right)\right] , \tag{B.4}$$

with $a^2 = x^2 + y^2$. The $P(z)$ parameter represents a complex phase difference associated with the beam propagation, while $q(z)$ is a complex parameter which describes the beam shape. Including Equation B.4 in Equation B.3 and comparing terms with the same power in r, we obtain the relations:

$$\frac{dq}{dz} = 1 , \qquad \frac{dP}{dz} = \frac{i}{q} . \tag{B.5}$$

We introduce, for convenience, two real parameters, r and w, so that:

$$\frac{1}{q} = \frac{1}{r} + i\frac{\lambda}{\pi w^2} , \tag{B.6}$$

where λ is the wavelength in the propagation medium ($k = 2\pi/\lambda = 2\pi n/\lambda_0$, with λ_0 wavelength in vacuum). Inserting Equation B.6 in B.4, we obtain:

$$\psi = \exp\left(iP + i\frac{\pi}{\lambda r}a^2 - \frac{a^2}{w^2}\right) . \tag{B.7}$$

For a given z value, $r(z)$ represents the radius of curvature of the wave front as measured on the beam axis, while $w(z)$ is the spot size, i.e. the radius of the beam for which the field amplitude is $1/e$ times the amplitude on the beam axis. A circle of radius w contains about 86.5% of the total power of the beam at each axis position. The real part of the q parameter cancels out at a given position along the z axis, called *waist* of the beam, where we have:

$$q_0 = -i\frac{\pi w_0^2}{\lambda} = -i\frac{\pi n w_0^2}{\lambda_0} , \tag{B.8}$$

and from Equation B.6 it results that the wave front is plane. Integrating the first of the

Equations B.5 and choosing the waist point as the origin, we find:

$$q(z) = q_0 + z = -i\frac{\pi w_0^2}{\lambda} = -iz_R + z\,, \tag{B.9}$$

where

$$z_R = iq_0 = \frac{k}{2}w_0^2 = \frac{\pi w_0^2}{\lambda} = \frac{\pi n w_0^2}{\lambda_0} \tag{B.10}$$

is the *Rayleigh distance*. The q parameter, hence, behaves as the wave front radius of curvature in geometrical optics varying the distance from the center of curvature, and the $-iz_R$ term represents an immaginary correction to account for the wave nature of radiation.

Combining Equations B.6 and B.9 and separating the real and immaginary parts, we obtain the variation of w and r with z:

$$w^2(z) = w_0^2\left[1 + \left(\frac{z}{z_R}\right)^2\right], \qquad r(z) = z\left[1 + \left(\frac{z_R}{z}\right)^2\right]. \tag{B.11}$$

B.1 Transformations of Gaussian beams by a thin lens

An ideal *thin lens* of focal length f changes a spherical wave with radius of curvature r_1 immediately before the lens into a spherical wave with radius of curvature r_2 immediately after the lens, following the *Thin-Lens Equation* (often referred as the *Lensmaker's formula*) [98]:

$$\frac{1}{r_2} = \frac{1}{r_1} - \frac{1}{f}\,, \tag{B.12}$$

where the radii of curvature are positive if the wave front is seen convex from $z \to +\infty$. Since for a thin lens the beam diameters immediately before and after the lens are the same, from Equation B.6 the relation between the q parameters for the entering and exiting beam thus results:

$$\frac{1}{q_2} = \frac{1}{q_1} - \frac{1}{f}\,, \tag{B.13}$$

where q_1 and q_2 are measured on the lens. This expression can be rewritten as [97]:

$$q_2 = \frac{Aq_1 + B}{Cq_1 + D}\,, \tag{B.14}$$

which is a general expression, where the coefficients A, B, C, D (which in this case are: $A = 1$, $B = 0$, $C = -1/f$, $D = 1$), are those of the matrix $ABCD$ of a lens between its two primary planes [97]. If we integrate the first of the Equations B.5 between z_1 and z_2, $q(z_2) = q(z_1)+z_2-z_1$, and we consider the general case where q_1 and q_2 are measured at distances s_1 and s_2 respectively from the lens we find that:

$$q_2 = \frac{(1 - s_2/f)\, q_1 + (s_1 + s_2 - s_1 s_2/f)}{-(1/f)\, q_1 + (1 - s_1/f)}\,. \tag{B.15}$$

Last Equation can be rewritten substituting the variables s_1 and s_2 with Z_1 and Z_2, defined as $Z_1 = s_1 - f$ and $Z_2 = s_2 - f$, so that:

$$(q_2 - Z_2)\,(q_1 + Z_1) = -f^2\,. \tag{B.16}$$

In the special case when $Z_1 = Z_0$ and $Z_2 = Z_i$ are the waist positions for the entering and exiting beam, the parameters q_1 and q_2 are immaginary:

$$q_1 = -i\frac{\pi}{\lambda}w_1^2 = -iz_{R1}\,, \qquad q_2 = -i\frac{\pi}{\lambda}w_2^2 = -iz_{R2}\,. \tag{B.17}$$

Putting Equation B.17 into B.16 and expanding the products, we obtain the relation:

$$f^2 - z_{R1}z_{R2} - Z_0 Z_i - i(z_{R2}Z_0 - z_{R1}Z_i) = 0\,. \tag{B.18}$$

The problem has a solution when both the real and immaginary parts cancel out:

$$\frac{z_{R2}}{z_{R1}} = \frac{Z_i}{Z_0}\,, \tag{B.19}$$

$$Z_0 Z_i = f^2 - z_{R1}z_{R2}\,. \tag{B.20}$$

Defining α as:

$$\alpha^2 = \frac{f^2}{Z_0^2 + z_{R1}^2}\,, \tag{B.21}$$

we can write z_{R2} and Z_i as functions of z_{R1} and Z_0:

$$z_{R2} = \alpha^2 z_{R1}\,, \tag{B.22}$$

$$Z_i = \alpha^2 Z_0\,. \tag{B.23}$$

Due to the relation between Rayleigh distance and waists expressed in Equation B.10, we can infer that $w_2 = \alpha w_1$, i.e. the α parameter represents the amplification of the beam transverse dimension between the two conjugated waist planes of the lens.

Bibliography

[1] S. Eales, "Planets and Planetary Systems", ed. John Wiley and Sons, Ltd. (2009).

[2] F. H. Shu, "The physical universe. An introduction to astronomy", University Science Books, Oxford University Press (1982).

[3] M. J. McCaughrean and C. R. O'dell, "Direct imaging of circumstellar disks in the Orion Nebula", *Astron. Journal* **111**, 1977-1987 (1996).

[4] K. E. Haisch, E. A. Lada, and C. J. Lada, "Disk frequencies and lifetimes in young clusters", *The Astroph. Journal* **533**, L153-L156 (2001).

[5] N. C. Santos, M. Mayor, D. Queloz, and S. Udry, "Extrasolar planets", *The Messenger* **110**, 32-38 (2002).

[6] A. Wolszczan and D. A. Frail, "A planetary system around the millisecond pulsar PSR1257+12", *Nature* **355**, 145-147 (1992).

[7] M. Mayor and D. Queloz, "A Jupiter-mass companion to a solar-type star", *Nature* **378**, 355-357 (1995).

[8] S. Udry and N. C. Santos, "Statistical properties of exoplanets", *Ann. Rev. of Astron. and Astrophys.* **45**, 397-439 (2007).

[9] J. Pollack, O. Hubickyj, P. Bodenheimer, J. Lissauer, M. Podolak, and Y. Greenzweig, "Formation of the giant planets by concurrent accretion of solids and gas", *Icarus* **124**, 62-85 (1996).

[10] G. F. Benedict, B. E. McArthur, T. Forveille, X. Delfosse, E. Nelan, R. P. Butler, W. Spiesman, G. Marcy, B. Goldman, C. Perrier, W. H. Jefferys, and M. Mayor, "A mass for the extrasolar planet Gliese 876b determined from Hubble Space Telescope fine guidance sensor 3 astrometry and high-precision radial velocities", *The Astroph. Journal* **581**, L115-L118 (2002).

[11] D. Pourbaix and A. Jorissen, "Re-processing the Hipparcos transit data and intermediate astrometric data of spectroscopic binaries. I. Ba, CH and Tc-poor S stars", *Astron. & Astrophys.* **145**, 161-183 (2000).

[12] N. C. Santos, "Extra-solar planets: detection methods and results", *New Astron. Rev.* **52**, 154-166 (2008).

[13] A. Baranne, D. Queloz, M. Mayor, G. Adrianzyk, G. Knispel, D. Kohler, D. Lacroix, J.-P. Meunier, G. Rimbaud, and A. Vin, "ELODIE: a spectrograph for accurate radial velocity measurements", *Astron & Astrophys. S.* **119**, 373-390 (1996).

[14] N. C. Santos, F. Bouchy, M. Mayor, F. Pepe, D. Queloz, S. Udry, C. Lovis, M. Bazot, W. Benz, J.-L. Bertaux, G. Lo Curto, X. Delfosse, C. Mordasini, D. Naef, J.-P. Sivan, and S. Vauclair, "The HARPS survey for souther extra-solar planets. II. A 14 Earth-masses exoplanet around μ Arae", *Astron. & Astrophys.* **426**, L19-L23 (2004).

[15] M. Mayor, F. Pepe, D. Queloz, F. Bouchy, G. Rupprecht, G. Lo Curto, G. Avila, W. Benz, J.-L. Bertaux, X. Bonfils, and 22 coauthors, "Setting new standards with HARPS", *The Messenger* **114**, 20-24 (2003).

[16] R. P. Butler, G. W. Marcy, E. Williams, C. McCarthy, P. Dosanjh, and S. S. Vogt, "Attaining Doppler precision of 3 m s^{-1}", *Publ. of Astron. Soc. of Pac.* **108**, 500-509 (1996).

[17] F. Pepe, M. Mayor, G. Rupprecht, G. Avila, P. Ballester, J.-L. Beckers, W. Benz, J.-L. Bertaux, F. Bouchy, B. Buzzoni, and 43 coauthors, "HARPS: ESO's coming planet searcher. Chasing exoplanets with the La Silla 3.6-m telescope", *The Messenger* **110**, 9-14 (2002).

[18] R. W. Hilditch, "An Introduction to close binary stars", Ed. R. W. Hilditch, Cambridge, Uk, Cambridge University Press, ISBN 0521241065, p.392 (2001).

[19] B. W. Carroll and D. A. Ostlie, "An introduction to modern astrophysics", Addison-Wesley Publishing Company, Inc., ISBN 0201547309 (1996).

[20] D. Queloz, G. W. Henry, J. P. Sivan, S. L. Baliunas, J. L. Beuzit, R. A. Donahue, M. Mayor, D. Naef, C. Perrier, and S. Udry, S., "No planet for HD 166435" *Astron. & Astrophys.* **379**, 279-287 (2001).

[21] F. Bouchy, M. Bazot, N. C. Santos, S. Vauclair, and D. Sosnowska, "Asteroseismology of the planet-hosting star μ Arae. I. The acoustic spectrum" *Astron. & Astrophys.* **440**, 609-614 (2005).

[22] K. Mandel and E. Agol, "Analytic light curves for planetary transit search", *The Astroph. Journal* **580**, L171-L175 (2002).

[23] F. Pont, C. H. F. Melo, F. Bouchy, S. Udry, D. Queloz, M. Mayor, and N. C. Santos, N.C., "A planet-sized transiting star around OGLE-TR-122. Accurate mass and radius near the hydrogen-burning limit", *Astron. & Astrophys.* **433**, L21-L24 (2005).

[24] A. Udalski, B. Paczynski, K. Zebrun, M. Szymaski, M. Kubiak, I. Soszynski, O. Szewczyk, L. Wyrzykowski, and G. Pietrzynski, "The optical gravitational lensing experiment. Search for planetary and low-luminosity object transits in the galactic disk. Results of 2001 campaign", *Acta Astronomica* **52**, 1-37 (2002).

[25] A. Udalski, O. Szewczyk, K. Zebrun, G. Pietrzynski, M. Szymanski, M. Kubiak, I. Soszynski, and L. Wyrzykowski, "The optical gravitational lensing experiment. Planetary and low-luminosity object transits in the Carina fields of the Galactic disk", *Acta Astronomica* **52**, 317-359 (2002).

[26] F. Bouchy, F. Pont, C. Melo, N. C. Santos, M. Mayor, D. Queloz, and S. Udry, "Doppler follow-up of OGLE transiting companions in the Galactic bulge" *Astron. & Astrophys.* **431**, 1105-1121 (2005).

[27] F. Pont, F. Bouchy, C. Melo, N. C. Santos, M. Mayor, D. Queloz, and S. Udry, S., "Doppler follow-up of OGLE planetary transit candidates in Carina", *Astron. & Astrophys.* **438**, 1123-1140 (2005).

[28] A. Jorissen, M. Mayor, and S. Udry, "The distribution of exoplanet masses", *Astron. & Astrophys.* **379**, 992-998 (2001).

[29] J. L. Halbwachs, F. Arenou, M. Mayor, S. Udry, and D. Queloz, "Exploring the brown dwarf desert with Hipparcos", *Astron. & Astrophys.* **355**, 581-594 (2000).

[30] N. C. Santos, G. Israelian, and M. Mayor, "Spectroscopic [Fe/H] for 98 extra-solar planet-host stars. Exploring the probability of planet formation", *Astron. & Astrophys.* **415**, 1153-1166 (2004).

[31] C. Lovis, M. Mayor, F. Bouchy, Y. Alibert, W. Benz, F. Bouchy, A. C. M. Correia, J. Laskar, C. Mordasini, D. Queloz, N. C. Santos, S. Udry, J.-L. Bertaux, and J. P. Silvan, "An extrasolar planetary system with three Neptune-mass planets", *Nature* **441**, 305-309 (2006).

[32] S. Udry, X. Bonfils, X. Delfosse, T. Forveille, M. Mayor, C. Perrier, F. Bouchy, C. Lovis, F. Pepe, D. Queloz, and J.-L. Bertaux, "The HARPS search for southern extrasolar planets. XI. Super-Earths (5 and $8M_{\oplus}$) in a 3-planet system", *Astron. & Astrophys.* **469**, L43-L47 (2007).

[33] M. Mayor, X. Bonfils, T. Forveille, X. Delfosse, S. Udry, J.-L. Bertaux, H. Beust, F. Bouchy, C. Lovis, F. Pepe, C. Perrier, D. Queloz, and N. C. Santos, "The HARPS search for southern extra-solar planets. XVIII. An Earth-mass planet in the GJ 581 planetary system", *Astron. & Astrophys.* **507**, 487-494 (2009).

[34] J. F. Kasting, D. P. Whitmire, and R. T. Reynolds, "Habitable zones around main sequence stars", *Icarus* **101**, 108-128 (1993).

[35] G. Schettino, E. Oliva, M. Inguscio, C. Baffa, E. Giani, A. Tozzi, and P. Cancio Pastor, "Optical Frequency Comb as a general-purpose and wide-band calibration source for astronomical high resolution infrared spectrographs", *Exp. Astron.* **31**, 69-81 (2011).

[36] E. Oliva, E. Origlia, C. Baffa, C. Biliotti, P. Bruno, F. D'Amato, C. Del Vecchio, G. Falcini, S. Gennari, F. Ghinassi, E. Giani, M. Gonzalez, F. Leone, M. Lolli, M. Lodi, R. Maiolino, F. Mannucci, G. Marcucci, I. Mochi, P. Montegriffo, E. Rossetti, S. Scuderi, and M. Sozzi, "The GIANO-TNG Spectrometer", *Proc. of SPIE* **6269**, 626919-626928 (2006).

[37] S. Gennari, I. Mochi, S. L. Donati, E. Oliva, L. Origlia, and P. Sandri, "The spectrometer optics of GIANO-TNG", *Proc. of SPIE* **6269**, 62693Z (2006).

[38] G. Lo Curto, C. Lovis, T. Wilken, G. Avila, B. Chazelas, M. Esposito, T. W. Hänsch, J. Gonzalez-Hernandez, R. Holzwarth, G. Ihlea, A. Manescau, L. Pasquini, F. Pepe, R. Rebolo, A. Segovia, P. Sinclaire, T. Steinmetz, T. Udem, and F. Wildi, "Along the path towards extremely precise radial velocity measurements", *Proc. of SPIE* **7735**, 77350Z1-77350Z8 (2010).

[39] G. Avila, P. Singh, and B. Chazelas, "Results on fibre scrambling for high accuracy radial velocity measurements", *Proc. of SPIE* **7735**, 7735881-7735889 (2010).

[40] P. G. van Dokkum and C. Conroy, "A substantial population of low-mass stars in luminous elliptical galaxies", *Nature* **468**, 940-942 (2010).

[41] M. Heath, L. Doyle, M. M. Joshi, and R. M. Haberle, "Habitability of planets around red dwarf stars", *OLEB* **29**, 405-424 (1999).

[42] M. Salaris and S. Cassisi, "Evolution of stars and stellar population", ed. John Wiley and Sons, ISBN 0470092203 (2005).

[43] A. Bauch, "Caesium atomic clocks: function, performance and applications", *Meas. Sci. Technol.* **14**, 1159-1173 (2003).

[44] J. E. Bernard, A. A. Madej, L. Marmet, B. G. Whitford, K. J. Siemsen, and S. Cundy, "Cs-based frequency measurement of a single, trapped ion transition in the visible region of the spectrum", *Phys. Rev. Lett.*, **82**, 3228-3231 (1999).

[45] T. Udem, A. Huber, B. Gross, J. Reichert, M. Prevedelli, M. Weitz, and T. W. Hänsch, "Phase-Coherent Measurement of the Hydrogen $1S$-$2S$ Transition Frequency with an Optical Frequency Interval Divider Chain", *Phys. Rev. Lett.* **79**, 2646-2649 (1997).

[46] M. Kourogi, K. Nakagawa, and M. Ohtsu, "Wide-span optical frequency comb generator for accurate optical frequency difference measurement", *IEEE J. Quantum Electron.* **29**, 2693-2701 (1993).

[47] J. Reichert, R. Holzwarth, T. Udem, and T. W. Hänsch, "Measuring the frequency of light with mode-locked lasers", *Opt. Comm.* **172**, 59-68 (1999).

[48] D. J. Jones, S. A. Diddams, J. K. Ranka, A. Stentz, R. S. Windeler, J. H. Hall, and S. T. Cundiff, "Carrier-envelope phase control of femtosecond mode-locked lasers and direct optical frequency synthesis", *Science* **288**, 635-639 (2000).

[49] T. Steinmetz, T. Wilken, C. Araujo-Hauck, R. Holzwarth, T. W. Hänsch, L. Pasquini, A. Manescau, S. D'Odorico, M. T. Murphy, T. Kentischer, W. Schmidt, and T. Udem, "Laser frequency combs for astronomical observations", *Science* **321**, 1335-1337 (2008).

[50] T. Udem, R. Holzwarth, and T. W. Hänsch, "Optical Frequency Metrology", *Nature* **416**, 233-137 (2002).

[51] M.C. Stumpf, S. Pekarek, A. E. H. Oehler, T. Sudmeyer, J. M. Dudley, and U. Keller, "Self-referenciable frequency comb from a 170-fs, 1.5-μm solid-state laser oscillator", *Appl. Phys. B* **99**, 401-408 (2010).

[52] J. Jiang, C. Mohr, J. Bethge, M. Fermann, and I. Hartl, "Fully Stabilized, Self-Referenced Thulium Fiber Frequency Comb", *CLEO/Europe and EQEC 2011 Conference Digest*, OSA Technical Digest (CD), paper PDB-1 (2011).

[53] M. J. Thorpe and J. Ye, "Cavity-enhanced direct frequency comb spectroscopy", *Appl. Phys. B* **91**, 397-414 (2008).

[54] S. M. Foreman, D. J. Jones, and J. Ye, "Flexible and rapidly configurable femtosecond pulse generation in the mid-IR", *Opt. Lett.* **28**, 370-372 (2003).

[55] D. Mazzotti, P. Cancio Pastor, G. Giusfredi, P. De Natale, and M. Prevedelli, "Frequency comb-based absolute frequency measurements in the mid-infrared with a difference-frequency spectrometer", *Opt. Lett.* **30**, 997-999 (2005).

[56] E. Penman, C.McGowan, P. Loza-Alvarez, D.T. Reid, M. Ebrahimzadeh, and W. Sibbett, "Femtosecond optical parametric oscillators based on periodically poled lithium niobate", *J. Mod. Opt.* **45**, 1285-1294 (1998).

[57] R. J. Jones, K. D. Moll, M. J. Thorpe, and J. Ye, "Phase-Coherent Frequency Combs in the Vacuum Ultraviolet via High-Harmonic Generation inside a Femtosecond Enhancement Cavity", *Phys. Rev. Lett.* **94**, 193201 1-4 (2005).

[58] C. Gohle, T. Udem, M. Herrmann, J. Rauschenberger, R. Holzwarth, A. Schuessler, F. Krausz, and T. W. Hänsch, "A frequency comb in the extreme ultraviolet", *Nature* **436**, 234-237 (2005).

[59] D. Spence, P. Kean, and W. Sibbett, "60-fsec pulse generation from a self-modelocked Ti-sapphire laser", *Opt. Lett.* **16**, 42-44 (1991).

[60] D. Meschede, "Optics, Light and Lasers. The Practical Approach to Modern Aspects of Photonics and Laser Physics", New York: Wiley-VCH, 2nd edition (2007).

[61] R. Szipocs, K. Ferencz, C. Spielmann, and F. Krausz, "Chirped multilayer coatings for broadband dispersion control in femtosecond lasers", *Opt. Lett.* **19**, 201-203 (1994).

[62] J. Ranka, R. Windeler, and A. Stentz, "Visible continuum generation in air-silica microstructure fibers with anomalous dispersion at 800 nm", *Opt. lett.* **25**, 25-27 (2000).

[63] E. P. Ippen, H. A. Haus, and L. Y. Liu, "Additive pulse mode locking", *J. Opt. Soc. Am. B* **6**, 1736-1745 (1989).

[64] K. Tamura, E. P. Ippen, H. A. Haus, and L. E. Nelson, "77-fs pulse generation from a stretched-pulse mode-locked all-fiber ring laser", *Opt. Lett* **18**, 1080-1082 (1993).

[65] J.-L. Peng, H. Ahn, R.-H. Shu, H.-C. Chui, and J. W. Nicholson, "Highly stable, frequency-controlled mode-locked erbium fiber laser comb", *Appl. Phys. B* **86**, 49-53 (2007).

[66] P. Pal, W. H. Knox, I. Hartl, and M. E. Fermann, "Self-referenced Yb-fiber-laser frequency comb using a dispersion micromanaged tapered holey fiber", *Opt. Expr.* **15**, 12161-12166 (2007).

[67] M. T. Murphy, T. Udem, R. Holzwarth, A. Sizmann, L. Pasquini, C. Araujo-Hauck, H. Dekker, S. D'Odorico, M. Fischer, T. W. Hänsch, and A. Manescau, "High-precision wavelength calibration of astronomical spectrographs with laser frequency combs", *Mon. Not. R. Astron. Soc.* **380**, 839-847 (2007).

[68] S. Osterman, S. Diddams, M. Beasley, C. Froning, L. Hollberg, P. MacQueen, V. Mbele, and A. Weiner, "A proposed laser frequency comb based wavelength reference for high resolution spectroscopy", *Proc. of SPIE* **6693**, 66931G1-66931G9 (2007).

[69] F. Kerber, G. Nave, C. J. Sansonetti, P. Bristow, and M. R. Rosa, "The spectrum of Th-Ar hollow catode lamps in the 900-4500 nm region: establishing wavelength standards for the calibration of VLT spectrographs", *ASP Conference Series* **364**, 461-478 (2007).

[70] J. W. Brault, "High Precision Fourier Transform Spectrometry: The Critical Role of Phase Corrections", *Mikrochimica Acta* **3**, 215 (1987).

[71] F. Bouchy, F. Pepe, and D. Queloz, "Fundamental photon noise limit to radial velocity measurements", *Astron. & Astrophys.* **374**, 733-739 (2001).

[72] S. A. Diddams, A. Bartels, T. M. Ramond, C. W. Oates, S. Bize, E. A. Curtis, J. C. Bergquist, and L. Hollberg, "Design and control of femtosecond lasers for optical clocks and the synthesis of low-noise optical and microwave signals", *IEEE J. Selected Topics Quantum Electron.* **9**, 1072-1080 (2003).

[73] T. Sizer, "Increase in Laser Repetition Rate by Spectral Selection", *IEEE J. Quantum Electron.* **25**, 97-103 (1989).

[74] T. Udem, J. Reichert, R. Holzwarth, and T. W. Hänsch, "Absolute Optical Frequency Measurement of the Caesium D1 Line with a Mode-Locked Laser", *Phys. Rev. Lett* **82**, 3568-3571 (1999).

[75] T. Steinmetz, T. Wilken, C. Araujo-Hauck, R. Holzwarth, T. W. Hänsch, and T. Udem, "Fabry-Perot filter cavities for wide-spaced frequency combs with large spectral bandwidth", *Appl. Phys. B* **96**, 251-256 (2009).

[76] D. A. Braje, M. S. Kirchner, S. Osterman, T. Fortier, and S. A. Diddams, "Astronomical spectrographs calibration with broad-spectrum frequency combs", *Eur. Phys. J. D* **48**, 57-66 (2008).

[77] E. A. Siegman, "Lasers", Mill Valley, California: University Science Books (1986).

[78] R. G. DeVoe, C. Fabre, K. Jungmann, J. Hoffnagle, and R. G. Brewer, "Precision optical-frequency-difference measurements", *Phys. Rev. A* **37**, 1802-1806 (1988).

[79] M. J. Thorpe, R. J. Jones, K. D. Moll, J. Ye, and R. Lalezari, "Precise measurements of optical cavity dispersion and mirror coating properties via femtosecond combs", *Opt. Expr.* **13**, 882-888 (2005).

[80] B. Edlen, "The refractive index of air", *Metrologia* **2**, 71-80 (1966).

[81] E. R. Peck and K. Reeder, "Dispersion of air", *J. of Opt. Soc. of A.* **62**, 958-962 (1972).

[82] H. Matsumoto, "The refractive index of moist air in the 3-μm region", *Metrologia* **18**, 49-52 (1982).

[83] P. E. Ciddor, "Refractive index of air: new equations for the visible and near-IR", *Appl. Opt.* **35**, 1566-1573 (1996).

[84] K. K. Lehmann, P. S. Johnston, and P. Rabinowitz, "Brewster angle prism retroreflectors for cavity enhanced spectroscopy", *Appl. Opt.* **48**, 2966-2979 (2009).

[85] F. Quinlan, G. Ycas, S. Osterman, and S. A. Diddams, "A 12.5 GHz-spaced optical frequency comb spanning >400 nm for near-infrared astronomical spectrograph calibration", *Rev. of Scient. Instrum.* **81**, 063105-063105-9 (2010).

[86] T. Wilken, C. Lovis, A. Manescau, T. Steinmetz, L. Pasquini, G. Lo Curto, T. W. Hänsch, R. Holzwarth, and T. Udem, "High-precision calibration of spectrographs", *Mon. Not. R. Astron. Soc.* **405**, L16-L20 (2010).

[87] C. Gohle, B. Stein, A. Schliesser, T. Udem, and T. W. Hänsch, "Frequency comb Vernier spectroscopy for broadband, high-resolution, high-sensitivity absorption and dispersion spectra", *Phys. Rev. Lett.* **99**, 2639021-2639024 (2007).

[88] T. Wilken, C. Lovis, A. Manescau, T. Steinmetz, L. Pasquini, G. Lo Curto, T. W. Hänsch, R. Holzwarth, and T. Udem, "High-precision calibration of spectrographs using laser frequency combs", *Proc. of SPIE* **7735**, 77350T1-77350T8 (2010).

[89] S. Osterman, S. Diddams, F. Quinlan, J. Bally, J. Ge, and G. Ycas, "A near infrared laser frequency comb for high precision Doppler planet surveys", *EPJ Web of Conference* **16**, 020021-020029 (2011).

[90] M. Hirano, T. Nakanishi, T. Okuno, and M. Onishi, "Silica-based highly nonlinear fibers and their application", *IEEE J. Sel. Topics Quantum Electron.* **15**, 103-114 (2009).

[91] C.-H. Li, A. J. Benedick, P. Fendel, A. G. Glenday, F. X. Kartner, D. F. Phillips, D. Sasselov, A. Szentgyorgyi, and R. L. Walsworth, "A laser frequency comb that enables radial velocity measurements with a precision of 1 cm/s", *Nature Letters* **452**, 610-613 (2008).

[92] C. E. Cramer, C.-H. Li, A. J. Benedick, A. G. Glenday, F. X. Kartner, D. F. Phillips, D. Sasselov, A. Szentgyorgyi, and R. L. Walsworth, "Astro-comb: revolutionizing precision spectroscopy in astrophysics", *Proc. IAU Symposium* **253**, 499-501 (2009).

[93] C.-H. Li, A. G. Glenday, A. J. Benedick, G. Chang, L.-J. Chen, C. Cramer, P. Fendel, G. Furesz, F. X. Kartner, S. Korzennik, D. F. Phillips, D. Sasselov, A. Szentgyorgyi, and R. L.

Walsworth, "In-situ determination of astro-comb calibrator lines to better than 10 cm/s", *Opt. Expr.* **18**, 13239-13249 (2010).

[94] K. L. Corwin, Z.-T. Lu, C. F. Hand, R. J. Epstein, and C. E. Wieman, "Frequency stabilized diode laser with the Zeeman shift in an atomic vapor", *Appl. Opt.* **37**, 3295-3298 (1998).

[95] G. Chang, C.-H. Li, D. F. Phillips, R. L. Walsworth, and F. X. Kartner, "Toward a broadband astro-comb: effect of nonlinear spectral broadening in optical fibers", *Opt. Expr.* **18**, 12736-12747 (2010).

[96] W. Nagourney, "Quantum electronics for atomic physics", ISBN 978-0-19-953262-9, Oxford University Press, Oxford graduate text (2010).

[97] H. Kogelnik and T. Li, "Laser beams and resonators", *Appl. Opt.* **5**, 1550-1567 (1966).

[98] E. Hecht, "Optics", 4th Edition, ISBN 0-321-18878-0, Addison Wesley (2002).